Synchronisation Behaviour of Viscoelastically Coupled Self-Sustained Oscillators as Models for Oscillations of Premature Cardiomyocytes

Dissertation

Zur Erlangung des mathematisch-naturwissenschaftlichen Doktorgrades
"Doctor rerum naturalium"
der Georg-August-Universität Göttingen
im Promotionsprogramm ProPhys
der Georg-August University School of Science (GAUSS)

vorgelegt von
Sebastian Stein
aus Bad Arolsen

Göttingen, 2017

Betreuungsausschuss

Prof. Dr. Reiner Kree (Referent)
Institute for Theoretical Physics
Georg-August-University Göttingen

apl. Prof. Dr. Ulrich Parlitz (Korreferent)
Biomedical Physics Group
Max Planck Institute for Dynamics and Self-Organization

Prof. Dr. Stefan Luther
Biomedical Physics Group
Max Planck Institute for Dynamics and Self-Organization

Mitglieder der Prüfungskommission

Prof. Dr. Reiner Kree (Referent)
Institute for Theoretical Physics
Georg-August-University Göttingen

apl. Prof. Dr. Ulrich Parlitz (Korreferent)
Biomedical Physics Group
Max Planck Institute for Dynamics and Self-Organization

Weitere Mitglieder der Prüfungskommission

Dr. Ragnar Fleischmann
Nonlinear Dynamics & Network Dynamics Group
Max Planck Institute for Dynamics and Self-Organization

Prof. Dr. Stefan Klumpp
Institut for Nonlinear Dynamics
Georg-August-University Göttingen

Prof. Dr. Stefan Luther
Biomedical Physics Group
Max Planck Institute for Dynamics and Self-Organization

Dr. Florian Rehfeldt
Third Institute of Physics - Biophysics
Georg-August-University Göttingen

Tag der mündlichen Prüfung: 16.10.2017

Affidavit

Hereby, I declare that the presented thesis has been written independently and with no other sources and aids than quoted.

List of related publications

Sebastian Stein, Stefan Luther, and Ulrich Parlitz. Impact of viscoelastic coupling on the synchronization of symmetric and asymmetric self-sustained oscillators. *New Journal of Physics*, 19(6):063040, 2017. doi: 10.1088/1367-2630/aa6d4a.

Disclosure

The research leading to this thesis was supported with funding from the German Research Foundation (DFG) via the Collaborative Research Center SFB 937 "Collective behavior of soft and biological matter" through project A18.

Dedicated to my first physics teacher Bernd Rauschenbach.

Contents

1. Introduction **1**
- 1.1. Research question of this thesis . . . 3
- 1.2. Structure of this document . . . 3

2. Background **5**
- 2.1. Excitation contraction coupling of cardiomyocytes . . . 5
- 2.2. Premature engineered heart muscle . . . 7
- 2.3. Concepts of linear rheology . . . 8
  - 2.3.1. From elasticity and viscosity to viscoelasticity . . . 8
  - 2.3.2. Models of viscoelastic materials . . . 10
  - 2.3.3. The complex modulus . . . 11
- 2.4. Concepts of nonlinear dynamics . . . 14
  - 2.4.1. Dynamics of nonlinear systems . . . 14
  - 2.4.2. Linear stability analysis . . . 15
  - 2.4.3. Bifurcation theory . . . 20
- 2.5. Concept of synchronicity . . . 25
  - 2.5.1. Self-sustained oscillators . . . 25
  - 2.5.2. Notion of the phase . . . 26
  - 2.5.3. Mutual synchronisation . . . 28

3. Oscillations of Cardiomyocytes **33**
- 3.1. Experimental setup and video data . . . 33
- 3.2. Video analysis . . . 34
  - 3.2.1. Signals of cellular beating . . . 36
  - 3.2.2. Signal filtering . . . 44
- 3.3. Results . . . 51
- 3.4. Summary . . . 56

4. Rheology of the Extracellular Matrix **59**
- 4.1. Experimental setup . . . 59
- 4.2. Data analysis . . . 61
- 4.3. Maxwell fluid approximation . . . 65

5. Two Oscillator Model **69**
- 5.1. Mathematical model . . . 70
- 5.2. Results . . . 80
  - 5.2.1. Synchronisation with symmetric linear restoring force . . . 83
  - 5.2.2. Synchronisation with asymmetric restoring force . . . 90

5.2.3. Synchronisation with symmetric nonlinear restoring force . . . 94
5.3. Summary . . . 97

6. Conclusion **101**

A. Additional Figures **103**
A.1. Pictures of the analysed premature cardiomyocytes . . . 103
A.2. Good vs. poor cell beating signals . . . 104
A.3. All cell beating signals . . . 105
A.4. Spectra of cell beating signals . . . 108
A.5. Frequency map of the in-phase synchronisation states . . . 111
A.6. Oscillation form of in- and anti-phase state . . . 112
A.7. Lissajous figures from raw experimental data . . . 113

B. Additional Calculations **115**
B.1. Equivalence of Relaxance and Retardance . . . 115
B.2. Solving Eq. (5.4c) with Green's function approach . . . 116

List of Figures **119**

Acknowledgements **121**

Curriculum Vitae **125**

1. Introduction

The heart is one of the most important organs which render human life possible. It is a muscular structure which pumps the blood through the entire body and is thus the central active unit driving the cardiovascular system. The muscle cells the heart comprises are called cardiomyocytes. For effectively operating as a pump, the heart has to contract and relax in a temporal coherent manner and thus have the cardiomyocytes. The frequency of this coherent beating behaviour is compelled by pacemaker cells [1]. These cells emit electric signals, which allow the cardiomyocytes to contract via the so called excitation contraction coupling [2]. In the mature heart, cardiomyocytes which are in direct contact are connected via gap junctions. Gap junctions allow ion currents to flow from one cell to another. By exploiting this communication channel, cardiomyocytes are able to operate in a coordinated manner [3].

To understand the formation process of heart tissue and possible pathological behaviour, effort has been made to study the physiological properties of cardiomyocytes and their development. Interestingly, they are able to contract without pacemaker cells, in a self-sustained manner, even in early development stages [4, 5, 6]. Radmacher et al. were one of the first who used atomic force microscopy to observe the mechanical beating behaviour of single cardiomyocytes [7]. Today, many studies deal with the quantitative characterisation of the electromechanical properties of the beating of single cardiomyocytes in terms of contraction force, beating frequency, intracellular calcium concentration, and membrane potential [8, 9, 10]. Eschenhagen and Zimmermann developed a biological system termed engineered heart muscle [11, 12]. The engineered heart muscle is coherent contracting heart tissue produced in a petri dish. Its premature state can be used as a model for studying the development process of heart tissue and the collective behaviour of premature cardiomyocytes in particular. Surprisingly, it can be observed that premature cardiomyocytes synchronise their beating behaviour although they are separated from each other. Tzlil et al. showed that the mechanical connection established by the medium surrounding the cells, is sufficient for the synchronisation process to happen [13]. This raises the question of how the mechanical properties of the medium influence the synchronisation behaviour of self-sustained beating premature cardiomyocytes.

The two most prominent components of the gel-like medium surrounding the cardiomyocytes are collagen, which builds the polymer structure of the extracellular matrix, and fibroblasts, which are cells that exert traction forces, remodel the extracellular matrix and stiffen the medium over time [14, 15, 16]. In general, the medium has to be considered viscoelastic. A material is called viscoelastic if it cannot be described as a pure elastic solid or a pure viscous liquid, but features both viscose and elastic properties to a certain extent. This means that the inner forces of a viscoelastic material opposing a

deformation depend on the deformation itself as well as on the rate of deformation; or that energy is only conserved to a certain extent during a deformation process [17]. Effort has been made to characterise the rheological properties of polymer gels or collagen in particular [18, 19, 20]. Baroccas et al. studied the rheological properties of collagen gels comprising fibroblasts and developed a mathematical model for describing the remodelling process [21, 22, 23]. Although linear viscoelastic behaviour can be modelled by simple serial-parallel-connection of Hookean springs and liner dampers [17], nonlinear viscoelastic behaviour, found in polymer gels, requires more sophisticated mathematical tools like fractional derivatives or Fourier rheology [24, 25, 26].

To theoretically study the synchronisation behaviour of premature cardiomyocytes in dependence on the viscoelastic properties of the medium surrounding them, mathematical models are needed for the medium as well as for the cardiomyocytes. Mathematical systems of different complexity and abstraction level have been used to model the latter. The more complex systems try to model cardiomyocytes as calcium oscillators on the detail level of their organelles [27, 28]. Systems with a moderate complexity focus on the electromechanical features of heart tissue on a more abstract level [29, 30]. Since cardiomyocytes exhibit self-sustained beating, they are represented by self-sustained oscillators in cases in which only their oscillatory properties on the highest abstraction level are considered [31, 32].

Especially the latter approach connects the synchronisation behaviour of viscoelastically coupled premature cardiomyocytes, modelled as self-sustained oscillators, to another very broad research field. Namely, the branch of nonlinear dynamics in which the synchronisation of networks of oscillatory units is studied in general. It exists a lot of theoretical and experimental work in this context [33, 34, 35, 36]. For example it was studied how networks of oscillators synchronise in the presence of time delay coupling [37, 38], chimera states have been found [39, 40], networks of coupled oscillators are used to model neuronal activity [41], and until today it is an open question how to experimentally tweak the coupling of two self-sustained oscillators to make them synchronise in an in- or anti-phase manner [42, 43].

1.1. Research question of this thesis

This thesis analyses how the synchronisation behaviour of self-sustained oscillators is influenced by the viscoelastic properties of their coupling. This question is motivated by the early development stage of artificial heart tissue in which the synchronisation of beating premature cardiomyocytes is aided by the viscoelastic polymer gel surrounding them. To tackle this task, a mathematical model is developed which comprises self-sustained oscillators and a viscoelastic component providing their coupling. Techniques and concepts from nonlinear dynamics are used to study the stability of the synchronous states featured by that model.

Furthermore, first experimental insights are provided and analysed which characterise the model system – the premature state of the engineered heart muscle. Videos of beat-

ing premature cardiomyocytes – recorded by Susanne Schlick[1] – are studied to extract the following features of their beating behaviour: frequency, oscillation form, and scale of contraction. Rheological experiments have been conducted – with the help of Susanne Schlick, Florian Spreckelsen[2], and Florian Rehfeldt[3] – to access the viscoelastic properties of the medium surrounding the premature cardiomyocytes. The acquired experimental data is analysed with image processing tools, time series analysis techniques, and concepts from linear and nonlinear phenomenological rheology.

1.2. Structure of this document

The main body of this document is subdivided into six chapters and two appendices. This introduction is followed by an explanation of the general concepts which build the scientific and technical background of this thesis and which might be of great avail for readers which are new to certain fields. The background chapter is followed by an analysis of the beating behaviour of premature cardiomyocytes. Videos of beating premature cardiomyocytes are analysed with image processing tools to access the temporal form of their beating. This data is further processed with time series analysis to access their beating frequency, oscillation form and scale of contraction. The next chapter is dedicated to the rheological properties of the medium surrounding the premature cardiomyocytes. Experimental results from shear rheometry experiments, which provide insights into the rheology of the extracellular matrix, are shown, interpreted, and facilitated to guide the following model process. A mathematical model of two viscoelastically coupled self-sustained oscillators is presented and analysed in the succeeding chapter. The stability properties of the synchronised states featured by that model are analysed with the help of bifurcation analysis tools and the obtained results are discussed in the contexts of nonlinear dynamics and the synchronisation process of premature cardiomyocytes. The main body of this document ends with a short summary and a general interpretation of the obtained results. Furthermore, and besides a list of figures, two appendices are provided which contain additional material in form of calculations and figures.

[1] Institute of Pharmacology and Toxicology, University Medical Center Göttingen
[2] Biomedical Physics Group, Max Planck Institute for Dynamics and Self-Organization, Göttingen
[3] Third Institute of Physics - Biophysics, Georg-August-University Göttingen

2. Background

This thesis touches three distinct fields. These are biomedical physics, rheology, and nonlinear dynamics. The functional behaviour of cardiomyocytes and the composition of the medium under study – the premature state of the engineered heart muscle – fall into the field of biomedical physics. Rheological concepts and tools are used to study the material properties of the medium which couples the premature cardiomyocytes. The final analysis of the synchronisation behaviour of viscoelastically coupled, self-sustained oscillators is ascribed to the field of nonlinear dynamics.

In order to understand this thesis, some background information about the mentioned topics might be of great avail. This background information is provided in the different sections of this chapter. First, the physiology of cardiomyocytes and the composition of the medium under study is presented. Those first sections are followed by a short introduction to the field of linear phenomenological rheology. After that, some notions and techniques from nonlinear dynamics are elaborated. These are used later to introduce the concept of synchronisation in the last section of this chapter. Note that although all information is provided which should be sufficient to better understand this thesis, the given introductions are far from being comprehensive. Thus, additional literature is mentioned to provide a good starting point for acquiring further and more detailed insights into the different topics.

2.1. Excitation contraction coupling of cardiomyocytes

In the context of this thesis, the two most important properties of cardiomyocytes are their ability to beat, or rather to contract in a self-sustained manner, and their ability to synchronise with each other. The former one can be understood in the context of *excitation contraction coupling*. This contraction mechanism of cardiomyocytes is described in two review papers published by Bers [2, 3].

A cardiomyocyte has to get excited or rather to depolarise in order to contract. Depolarisation means that the *transmembrane potential* of the cell changes from negative voltage to about zero. The transmembrane potential is the electrical potential measured between the inner and outer part of the cell. Usually, this depolarisation is caused by an ion flux from neighbouring cells via *gap junctions* and opens ion channels which allow calcium (Ca^{+2}) influx. The raised calcium concentration [Ca^{+2}] triggers the *sarcoplasmic reticulum* of the cell to release Ca^{+2}, and thus the intracellular calcium concentration raises even further. Ca^{+2} diffuses though the cell and binds to the *myofilaments* which contract the cell along the direction of their alignment. After some time, the intracellular calcium concentration recovers to its base level. This process is governed by the sarcoplasmic reticulum up-taking Ca^{+2} and by ion pumps pumping Ca^{+2} outside the

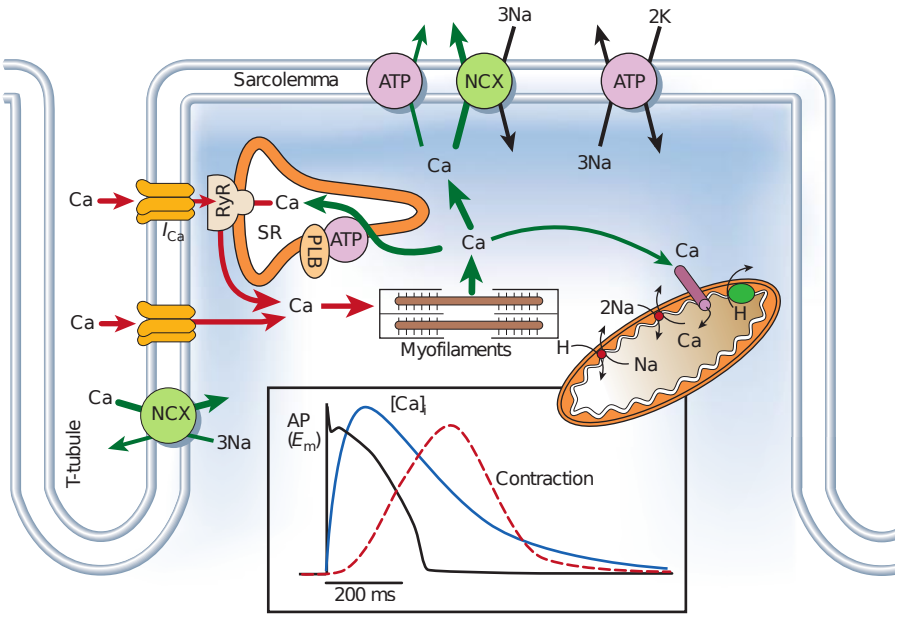

Figure 2.1.: Sketch showing the calcium transport during the excitation contraction coupling of a cardiomyocyte. Shown are different organelles which transport ions through the cell membrane (sarcolemma), the sarcoplasmic reticulum (orange boundary) which releases a large portion of calcium into the cell if excited, and the myofilaments which make the cell contract if in contact with calcium, beside others. The picture was taken from Bers [2].

cell. As soon as the calcium concentration has recovered to a certain extent, the cardiomyocyte can be excited again. Figure 2.1 shows a sketch of the ion transport during the excitation contract coupling.

Note that the described behaviour is valid for adult cardiomyocytes inside heart tissue and that the contraction of single premature cardiomyocytes differs at least in two ways. Depending on the age, the myofilaments of premature cardiomyocytes might not be aligned well. Thus the cell might not contract along a distinct direction but rather buckles. Furthermore it is known that premature cardiomyocytes beat in a self-sustained manner, thus without the stimulus from neighbouring cells. This self-sustained beating is driven by oscillations of the inner calcium concentration [4, 6].

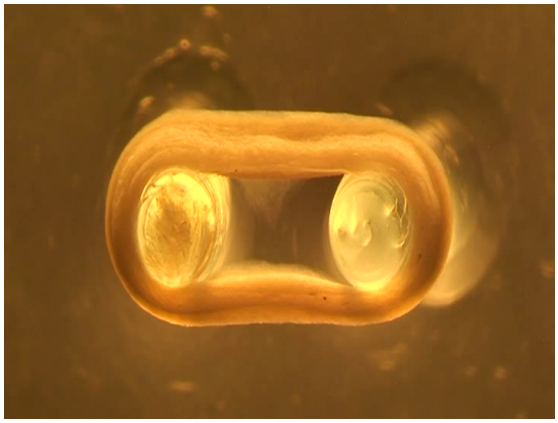

(a) Picture of a mature ring-shaped engineered heart muscle. The image was provided by Zimmermann[a] et al. and post processed.

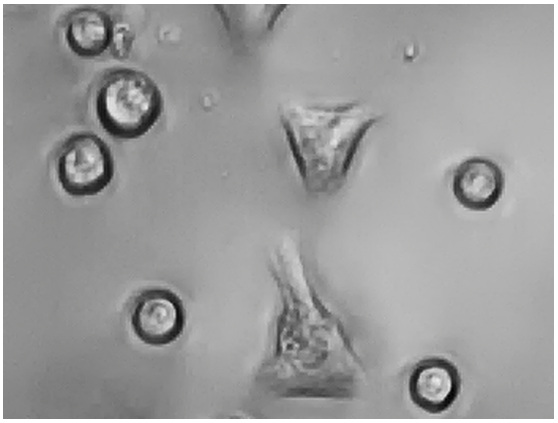

(b) Microscope recording of (roundish) premature cardiomyocytes among some elongate cardiomyocytes. The image was recorded by Susanne Schlick[a] and post processed.

Figure 2.2.: Macroscopic and microscopic pictures of engineered heart muscles as mature tissue and as premature gel.

[a]Institute of Pharmacology and Toxicology, University Medical Center Göttingen

2.2. Premature engineered heart muscle

The biological system under study is a premature state of the *engineered heart muscle* (EHM) system developed by Eschenhagen and Zimmermann [11, 12]. The engineered heart muscle is self-sustained and coherent contracting heart tissue produced in a petri dish. Global contractions begin around a month after cultivation. Its final shape and size depends on the mechanical boundary conditions of the petri dish during its development. Ring-shaped EHMs are macroscopic objects with spatial extents on the length scale of 1 mm – 10 mm. The development of mature EHMs takes around three months.

The premature state of the EHM can be considered as a polymer hydrogel populated by cardiomyocytes and fibroblasts. Collagen builds the polymer structure of the extracellular matrix. During the development of the EHM, the fibroblasts exert traction forces which remodel and compress the gel until it can be considered as a tissue [14, 15, 16]. The (premature) cardiomyocytes are quiescent and roundish after cultivation but start to contract and to elongate while they mature. The onset of their synchronisation is around 8 h – 15 h after cultivation, depending on the cell density. Recent studies have shown that cardiomyocytes can be synchronised by mechanical stimuli mediated by the extracellular matrix [13]. The diameter of roundish premature cardiomyocytes is on the length scale of 10 μm. The biological system under study is the premature state of the EHM in which the premature cardiomyocytes start to synchronise their contraction behaviour. A mature ring-shaped EHM is shown in Figure 2.2a while Figure 2.2b shows a microscope recording of premature cardiomyocytes.

2.3. Concepts of linear rheology

At this, point a short introduction to the concepts of linear rheology will be given. This introduction is based on Tschoegl [17].

2.3.1. From elasticity and viscosity to viscoelasticity

The rheological properties of a material determine how this material is deformed if a force is acting on it. The study of these properties is called rheology. In the field of linear rheology, all the constitutive equations obey linearity. One can distinguish between two types of deformations:

Elastic Deformation The energy needed for a elastic deformations is preserved (thus it is reversible without energy loss) and the deformation is instantaneous (thus it does not depend on rates). During a linear elastic deformation the force F acting on an elastic material is proportional (with factor k) to its elongation Δl:

$$F = k\,\Delta l. \tag{2.1}$$

Viscous Deformation The energy needed for a viscous deformation is not preserved and the deformation happens over a finite time. During a linear viscous deformation the force F acting on a viscous material is proportional (with factor n) to its rate of elongation $\mathrm{d}\Delta l/\mathrm{d}t$:

$$F = n\,\frac{\mathrm{d}\Delta l}{\mathrm{d}t}. \tag{2.2}$$

Because rheology is the study of *material* and not *object* properties, one seeks a formulation of the constitutive equations Eq. (2.1) and Eq. (2.2) which does not depend on the geometry of the object under study. Following this approach one uses *stress* $\sigma = F/A_0$, which is the force acting on an object per unit area A_0, instead of force F, and *strain* $\varepsilon = \Delta l/l_0$, which is the relative elongation with respect to a reference length l_0, instead of elongation Δl.

$$\sigma = E\,\varepsilon \tag{2.3}$$

$$\sigma = \eta\,\frac{\mathrm{d}\varepsilon}{\mathrm{d}t} \tag{2.4}$$

Doing so, the constitutive equations (Eq. (2.3) and Eq. (2.4)) depend only on material properties which are independent of geometry. These are the *elastic modulus* or *Young's modulus* $E = k\,l_0/A_0$ and the *viscosity* $\eta = n\,l_0/A_0$. For an illustration see Figure 2.3.

The two deformation scenarios described above are idealised limit cases. Real materials exhibit always both kinds of deformations to a certain extent. How viscous or elastic a material deforms often depends on the time scale of deformation. To predict how a material behaves in certain scenarios, its **viscoelastic** properties need to be known. Since the strain-stress response of viscoelastic materials depends on the whole material

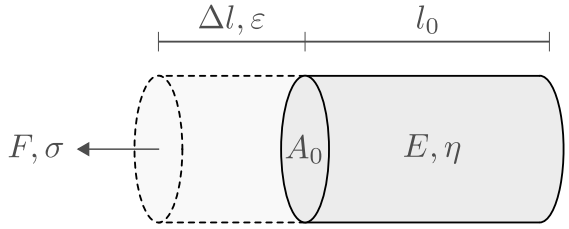

Figure 2.3.: Sketch of an object with reference length l_0, cross section area A_0, elastic modulus E, and viscosity η. It is deformed about the length Δl corresponding to the strain ε by an external force F corresponding to the stress σ.

history, the constitutive equations describing them are not functions but functionals; and the viscoelastic properties are no scalars but functions of time.

$$\sigma(t) = \mathcal{F}[\varepsilon(u)]_0^t = \int_0^t Q(t-u)\,\varepsilon(u)\,\mathrm{d}u \tag{2.5}$$

$$\varepsilon(t) = \mathcal{F}[\sigma(u)]_0^t = \int_0^t U(t-u)\,\sigma(u)\,\mathrm{d}u \tag{2.6}$$

Equations Eq. (2.5) and Eq. (2.6) showing the stress response $\sigma(t)$ to a history of strain $\varepsilon(u)$ and the strain response $\varepsilon(t)$ to a history of stress $\sigma(u)$, respectively. The response functions are called *relaxance* $Q(t)$ and *retardance* $U(t)$. It is important to note that the relaxance and the retardance are equivalent in the sense that each of them fully describes the viscoelastic behaviour of the material under study on its own, since[1]

$$\int_0^t Q(t-u)\,U(u)\,\mathrm{d}u = \delta(t). \tag{2.7}$$

holds. The choice of which response function to use often depends on the experimental accessibility. For example the relaxance of a material is given as the stress response to an instantaneous strain impulse stimulus:

$$Q(t) = \frac{\sigma(t)}{\varepsilon_0}, \quad \text{with} \quad \varepsilon(t) = \varepsilon_0\,\delta(t). \tag{2.8}$$

Besides the relaxance and the retardance there are many other equivalent response functions, each of them accessible via other kinds of stimuli.

2.3.2. Models of viscoelastic materials

The task of viscoelastic modelling is to derive constitutive equations[2] for materials with different viscoelastic properties to understand and predict their behaviour under load.

[1] See Sec. B.1 for a more detailed explanation.
[2] These are the equations which directly relate stress and strain (or their derivatives) to each other.

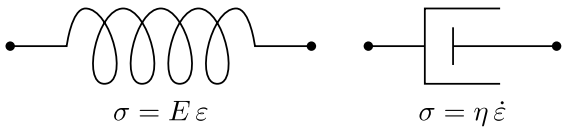

Figure 2.4.: Sketch of the two basic building blocks of serial-parallel models. Left is a Hookean spring with the modulus E and right a Newtonian dashpot with the viscoelasticity η.

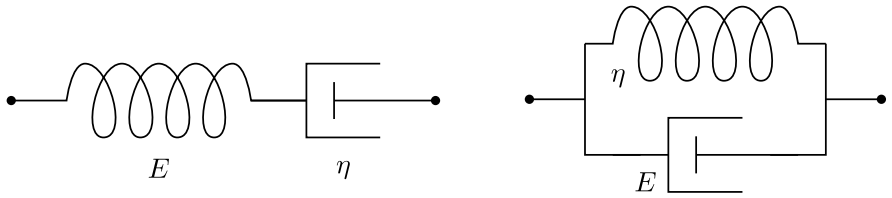

(a) The Maxwell fluid consists of a Hookean spring in serial with a Newtonian dashpot.

(b) The Kelvin-Voigt material consists of a Hookean spring in parallel with a Newtonian dashpot.

Figure 2.5.: Sketch of the two simplest possible serial-parallel models: A Maxwell fluid and a Kelvin-Voigt material. E denotes the moduli of the springs and η denotes the viscosity of the dashpots.

The simplest models describe the behaviour of purely elastic or viscous materials. The model of an idealised elastic material is a Hookean spring obeying Eq. (2.3). And the model of an idealised viscous material is a Newtonian dashpot obeying Eq. (2.4).

One prominent class of linear viscoelastic models has the former mentioned as building blocks. This class is called *serial-parallel* models. The idea is to combine the idealised elastic and viscous behaviour of springs and dashpots to produce viscoelastic behaviour. The two simplest of those serial-parallel combinations are called *Maxwell fluid* and *Kelvin-Voigt material*. They obey the following constitutive equations and are shown in Figure 2.5.

$$\text{Maxwell fluid:} \quad \dot{\sigma} = E\,\dot{\varepsilon} - \frac{E}{\eta}\,\sigma \tag{2.9}$$

$$\text{Kelvin-Voigt material:} \quad \sigma = \eta\,\dot{\varepsilon} + E\,\varepsilon \tag{2.10}$$

Their names are motivated by their rheodictic[3] and arrheodictic[4] behaviour, respectively. Although it is easy to create further kinds of serial-parallel models with more building blocks to model more complicated viscoelastic behaviour, this approach has some disadvantages. In very complex models the single parameters cannot be interpreted anymore as material parameters in a meaningful sense due to their large number. Thus the ability

[3]Materials which do not have a well defined reference configuration, such as many fluids like water, are called rheodictic.

[4]Materials which do have a well defined reference or rest configuration, such as some solids like rubber, are called arrheodictic.

to understand the material behaviour via the applied model is lost. Furthermore, they are not suited to reproduce any arbitrary kind of viscoelastic response. For example power law like responses found in polymers cannot be modelled by serial-parallel models which comprise a finite number of elements [25, 26]. But if kept simple and applied in an adequate way, serial-parallel models are a powerful tool to characterise the behaviour of a large variety of materials [44], and are able to convey a valuable understanding of viscoelasticity itself.

2.3.3. The complex modulus

One prominent viscoelastic response function is the *dynamic modulus* or *complex modulus* $G^*(\omega)$. The complex modulus is defined as the stress response to a harmonic strain stimulus after infinite time.

$$G^*(\omega) = \lim_{t\to\infty} \frac{\sigma(t,\omega)}{\varepsilon(t,\omega)} \quad \text{with} \quad \varepsilon(t,\omega) = \varepsilon_0 \exp(i\,\omega\,t) \tag{2.11}$$

The direct physical meaning of the complex modulus is revealed by considering its real and imaginary part.

$$G^*(\omega) = G'(\omega) + i\,G''(\omega) = \widetilde{G}(\omega)\,\exp[i\,\theta(\omega)] \tag{2.12}$$

The *storage modulus* $G'(\omega)$ is proportional to the average energy **conserved** during one cycle per unit volume, the *loss modulus* $G''(\omega)$ is proportional to the average energy **dissipated** during one cycle per unit volume, and the tangent of the *loss angle* $\tan[\theta(\omega)] = G''(\omega)/G'(\omega)$ is the ratio between the dissipated and the conserved energy during one cycle per unit volume of the material. Reconsidering the definitions of elasticity and viscosity given along with Eq. (2.1) and Eq. (2.2), which state that the energy needed for a purely elastic or purely viscous deformation is preserved or lost respectively, the loss angle can be interpreted as a measure of how elastic or viscous the material under study is[5].

To get further insight into the meaning of the complex modulus and its components, it is derived analytically for the Maxwell fluid and the Kelvin-Voigt material (see Figure 2.5). To do so, Eq. (2.9) and Eq. (2.10) are used along with the definition of the complex modulus Eq. (2.11). The resulting complex moduli are given as follows and are shown in Figure 2.6.

$$\text{Maxwell fluid:} \quad G^*(\omega) = E\left(1 - \frac{E^2/\eta^2}{E^2/\eta^2 + \omega^2}\right) + i\,E\,\frac{E/\eta}{E^2/\eta^2 + \omega^2}\,\omega \tag{2.13}$$

$$\text{Voigt material:} \quad G^*(\omega) = E + i\,\eta\,\omega \tag{2.14}$$

To understand the shown complex moduli by intuition one could think about how the corresponding model will behave (in terms of elastic or viscous response) if it is stimulated by different frequencies.

[5] On the time scale given by $2\pi/\omega$.

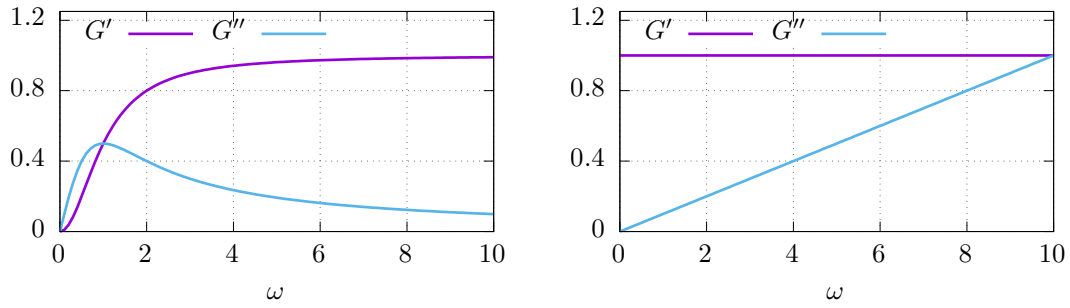

(a) Complex modulus of the Maxwell fluid (Eq. (2.13)) with $E = \eta = 1$.

(b) Complex modulus of the Kelvin-Voigt material (Eq. (2.14)) with $E = \eta = 1$.

Figure 2.6.: Complex moduli (Eq. (2.11)) of the Maxwell fluid and the Kelvin-Voigt material (Fig. 2.5) split up into storage and loss modulus.

First, the Maxwell fluid (Figure 2.5a) is considered. If the Maxwell fluid is stimulated with a periodic strain or elongation $\varepsilon(\omega = 0)$ with a frequency equal to zero, meaning infinitely slow, no energy is conserved or dissipated during the deformation process. This is because an infinitely slow elongation will result in a strain rate equal to zero $\dot{\varepsilon} = 0$. Thus no strains which correspond to the friction in the Newtonian dashpot (Eq. (2.2)) occur. Nevertheless the steady and strain free elongation of the dashpot allows the spring to stay at its rest length although the whole model is elongated. So no strains corresponding to the elastic spring can be measured either. This means that no energy is needed for an infinitely slow elongation of the Maxwell fluid. Thus the storage $G'(\omega)$ and the loss modulus $G''(\omega)$ are equal to zero at $\omega = 0$. If, however, the Maxwell fluid is stimulated by an infinitely fast elongation ($\omega \to \infty$) the dashpot acts like an solid rod since $\dot{\varepsilon} \to \infty$. Thus, the deformation happens only via the elongation of the spring. Since the spring perfectly conserves all the energy needed for the deformation, the storage modulus $G'(\omega)$ approaches a limit given by its elastic modulus while the loss modulus $G''(\omega)$ goes to zero.

Now the Kelvin-Voigt material (Figure 2.5b) is considered. All elongations applied affect both the spring and the dashpot equally since they are setup in parallel. The strain generated by the spring does not depend on the rate of the elongation. Thus, the energy stored does not depend on the frequency of elongation either. That is why the storage modulus is constant with respect to ω and only depends on the elastic modulus of the spring. The strain generated by the dashpot depends linearly on the rate of elongation. Thus, the energy dissipated depends linearly on the elongation frequency. This means that the loss modulus does as well and is zero for infinitely slow elongations and approaching infinity for infinitely fast elongations.

2.4. Concepts of nonlinear dynamics

Dynamical systems obeying nonlinear constitutive equations are studied in the research field of nonlinear dynamics. The fact that those equations are nonlinear adds an additional layer of complexity, since the dynamical behaviour of those systems cannot be described by simple superpositions of exponential functions in general, as it is possible with linear systems. That means, analytic solutions which fully describe the systems dynamics cannot be found in general, thus making their analysis more challenging. On the other hand, those systems are able to exhibit very rich dynamical behaviour as their solutions are not restricted to a set of basis functions. In this section, a short introduction into the concepts and tools of the field of nonlinear dynamics is given to an extent which is of avail for the understanding of this thesis. For a more detailed overview Argyris et al. [45] is recommended.

2.4.1. Dynamics of nonlinear systems

Nonlinear systems can be described by nonlinear ordinary differential equations if time is assumed to flow continuously[6] and if the system is assumed to be not spatially extended. That means that the only independent variable[7] is time t.

$$\frac{\mathrm{d}\boldsymbol{x}}{\mathrm{d}t} = \boldsymbol{f}(\boldsymbol{x}, t) \tag{2.15}$$

The temporal derivatives of the dependent variables $\boldsymbol{x}$ are given by a nonlinear vector field $\boldsymbol{f}$ which in turn depends on the dependent variables and time in general. Note that lowercase bold italic letters are used for denoting vectors. Since only autonomous nonlinear systems are considered in this thesis, the explicit time dependence will be neglected henceforth. The current state of the system is given as the union of all dependent variables at a certain point in time $\boldsymbol{x}_t$. It is common to define the *phase flow* $\boldsymbol{\phi}$ which transports a system state in time.

$$\boldsymbol{\phi} : t + \Delta t, \boldsymbol{x}_t \to \boldsymbol{x}_{t+\Delta t} \tag{2.16a}$$

$$\boldsymbol{\phi}(t + \Delta t, \boldsymbol{x}_t) = \boldsymbol{x}_{t+\Delta t} \tag{2.16b}$$

Although the phase flow is implicitly given by Eq. (2.15), which defines the past and the future[8] of all states, it cannot be given analytically in general. Nevertheless, its notion is utile in order to "speak" about the dynamics compelled by the *equations of motion* Eq. (2.15). One can think about the phase flow as the nonlinear equivalent[9] to

[6] If time is assumed to flow in discrete portions the systems under study are described in terms of nonlinear maps.

[7] If the system is assumed to be extended, it is described by partial differential equations and the additional independent variables are the spacial dimensions of the system.

[8] All systems in this thesis are deterministic.

[9] To be precise, the phase flow *is* the general solution of the system Eq. (2.15). The distinction between linear and nonlinear systems is only made for didactical reasons.

the general solution of a linear system, which transports an initial condition forward in time. Given a fixed initial condition $\boldsymbol{x}_0$, the phase flow generates a *trajectory*[10] $\boldsymbol{x}$.

$$\boldsymbol{x} : t \to \boldsymbol{x}_t \tag{2.17a}$$

$$\boldsymbol{\phi}(\boldsymbol{x} = \boldsymbol{x}_0, t) \equiv \boldsymbol{x}(t) = \boldsymbol{x}_t \tag{2.17b}$$

A trajectory is a continuous curve of system states, parametrised by time and it is equivalent to a fundamental solution of Eq. (2.15). The trajectory resides in *phase space* which is the space spanned by all dependent variables $\{x_i\}$, which are called *dynamic variables* henceforth. Again, the analytical form of both, the phase flow and its generated trajectories, are not known in general. To analyse the dynamics of the system under study, one exploits the fact that the temporal derivatives of the dynamic variables in Eq. (2.15) are tangent to the trajectories. Thus, by following those tangents one is able to generate trajectories graphically and numerically. For illustrating this, the following dynamical system, the Van der Pol oscillator, shall be considered.

$$\dot{x}_1 = f_1(x_1, x_2) = x_2 \tag{2.18a}$$

$$\dot{x}_2 = f_2(x_1, x_2) = \mu \left(1 - x_1^2\right) x_2 - \omega^2 x_1 \tag{2.18b}$$

By plotting the vector field given by $(f_1, f_2)^{\mathrm{T}}$ in phase space, the dynamical behaviour of system Eq. (2.18) can be accessed. Figure 2.7 shows the phase portrait of the Van der Pol oscillator. It can be seen how two different initial conditions lead to two different trajectories (orange and blue line). The direction of time is illustrated by the direction of the arrows, representing the vector field $(f_1, f_2)^{\mathrm{T}}$. In addition to the trajectories two other structures are shown in Figure 2.7: two *invariant sets*; a (stable) periodic orbit and an (unstable) fixed point.

Invariant sets are special sets of points in phase space. If a point of an invariant set is chosen as an initial condition, the corresponding trajectory will never leave this set. Furthermore, an additional property can be assigned to invariant sets, which is their *stability*. Stable invariant sets attract trajectories and unstable ones repel them. Taking these two properties together, invariant sets define the topology of the phase flow and thus the dynamical behaviour which can be observed. Thus, analysing a nonlinear system's dynamics boils down to finding and characterising its invariant sets. In general, this can only be done numerically or semi-analytically. The notions utilised for that purpose are discussed in the following.

2.4.2. Linear stability analysis

An invariant set's dimension is limited by the dimension of the dynamical system featuring it. Zero dimensional invariant sets, which are called *fixed points*, play a singular role since they can be found and classified analytically in many cases. To access their stability, linear stability analysis is used. The concepts introduced in this context can be generalised to invariant sets of higher dimensions later.

[10] Not that it is common in physics that functions and the elements of their image sets are addressed with the same symbol.

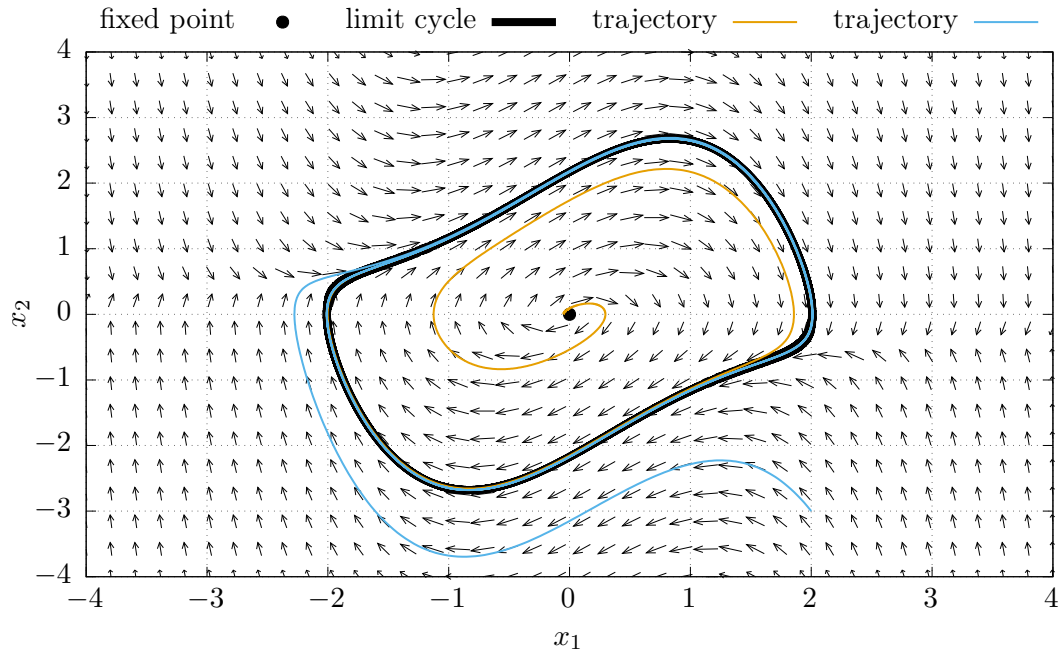

Figure 2.7.: Phase space portrait of the Van der Pol oscillator Eq. (2.18) with $\mu = \omega = 1$. For two different initial conditions, the phase flow generates two different trajectories which are colour coded by orange and blue. The vectors of the vector field $(f_1, f_2)^{\mathrm{T}}$ are tangent to these trajectories. Furthermore, the only (unstable) fixed point and the only (stable) periodic orbit of the system are shown in black.

Since the trajectory generated by the phase flow for an initial condition identical to the fixed point $\boldsymbol{x}^*$ only comprises the fixed point itself, the temporal derivatives of all dynamic variables have to vanish at the fixed point.

$$0 = \left.\frac{\mathrm{d}\boldsymbol{x}}{\mathrm{d}t}\right|_{\boldsymbol{x}=\boldsymbol{x}^*} = \boldsymbol{f}(\boldsymbol{x}^*) \tag{2.19}$$

The solutions of the nonlinear system of equations (Eq. (2.19)) might be found analytically. A fixed point is asymptotically stable if trajectories are attracted towards it and asymptotically unstable if they are repelled. Since there can be multiple "competing" stable invariant sets in phase space, the given definition has only to hold in the infinitesimally close proximity of the fixed point under study. The *Hartman-Grobman* theorem states that the nonlinear phase flow is topologically conjugated to the phase flow of the linearised system in the vicinity of a hyperbolic fixed point. The dynamics of the linearised system are defined by the linearised (around the fixed point x^*) differential equations[11]:

$$\frac{\mathrm{d}\boldsymbol{x}}{\mathrm{d}t} \approx \boldsymbol{f}_l(\boldsymbol{x}) = \overbrace{\boldsymbol{f}(\boldsymbol{x}^*)}^{=0} + \left.\frac{\partial f_i}{\partial x_j}\right|_{\boldsymbol{x}^*} (\boldsymbol{x} - \boldsymbol{x}^*) = J|_{\boldsymbol{x}^*}\ (\boldsymbol{x} - \boldsymbol{x}^*). \tag{2.20}$$

Here $J|_{\boldsymbol{x}^*}$ is the Jacobian of $\boldsymbol{f}$ at the fixed point $\boldsymbol{x}^*$. If the real parts of the eigenvalues of the Jacobian $J|_{\boldsymbol{x}^*}$ do not vanish, the fixed point $\boldsymbol{x}^*$ is called a hyperbolic fixed point. The dynamics of a trajectory in the proximity of the fixed point $\boldsymbol{x}(t) = \boldsymbol{x}^* + \Delta\boldsymbol{x}$ is studied to check if the fixed point is attracting or repelling. This means that small deviations Δx from the fixed point decrease or increase in time, respectively. The linearised equations Eq. (2.20) are used for this purpose. Insertion of the trajectory yields:

$$\frac{\mathrm{d}\boldsymbol{x}}{\mathrm{d}t} = \overbrace{\frac{\mathrm{d}\boldsymbol{x}^*}{\mathrm{d}t}}^{=0} + \frac{\mathrm{d}\Delta\boldsymbol{x}}{\mathrm{d}t} \approx \boldsymbol{f}_l(\boldsymbol{x}^* + \Delta\boldsymbol{x}) = J|_{\boldsymbol{x}^*}\ \Delta\boldsymbol{x}. \tag{2.21}$$

The general solution of the linear differential equation is known to be a linear combination of N exponential functions; where the number of dimensions of the system under study is denoted by N. Those exponential functions have the eigenvalues ν_i of $J|_{\boldsymbol{x}^*}$ as exponents and its eigenvectors $\boldsymbol{v}_i$ as prefactors.

$$\Delta\boldsymbol{x}(t) = \sum_i^N a_i\, \boldsymbol{v}_i\, \mathrm{e}^{\nu_i\, t} \tag{2.22}$$

This solution states that a multidimensional deviation $\Delta\boldsymbol{x}$ from a fixed point will exponentially grow or decay in direction of the eigenvector $\boldsymbol{v}_i$, on the time scale given by the real part of the corresponding eigenvalue ν_i. If all the real parts of the eigenvalues are negative $\mathrm{Re}\{\nu_i\} < 0\ \forall\ i$, the fixed point is called asymptotically stable.

[11] In this thesis, the terms in long equations which are used later are emphasised.

Invariant sets which are asymptotically stable are called *attractors*. Since they attract trajectories in phase space, they can be easily found by numerically integrating the equations of motion forward in time. If multiple attractors coexist, the initial conditions determine in which attractor the resulting trajectory will end up. The union of all initial conditions which lead to a certain attractor is called *basin of attraction* of this attractor. Invariant sets which are asymptotically unstable along **all** phase space directions are called *repellers*. They can be found by numerically integrating the equations of motion backward in time. Invariant sets which attract trajectories along some directions in phase space and repel them along others are called saddles[12].

The spectrum of *Lyapunov exponents* $\{\lambda_i\}$ quantifies the stability of invariant sets with an arbitrary number of dimensions. It is a statistical measure of stability and can be calculated numerically [46]. Note that the Lyapunov spectrum of a fixed point is equal to the union of its eigenvalues' real parts $\lambda_i = \mathrm{Re}\{\nu_i\}$. The meaning of Lyapunov exponents can be understood by considering the notion of phase volume and its growth rates σ_i along certain directions in phase space. A phase volume is defined as a bounded continuous set of states in phase space. Each state can be considered as an initial condition of a trajectory. The phase flow deforms that volume over time. The mean[13] rates with which the principal components of the phase volume change are the Lyapunov exponents. Consider Figure 2.8 as an example. There, a phase volume near a stable periodic orbit is considered. A periodic orbit is a closed one dimensional invariant set. Dynamic variables of the trajectories which live on top of this structure oscillate periodically in time. Since the orbit is stable, the phase volume shrinks towards it in one direction of phase space. Along the other direction, the phase volume does not change size. This is caused by the motion a trajectory exhibits on top of the orbit. Along the direction of motion, a perturbation does neither grow nor decay. Since Lyapunov exponents are usually ordered with respect to their magnitude, the first Lyapunov exponent of this periodic orbit is zero and the second one is negative $\{\lambda_1 = 0, \lambda_2 < 0\}$.

Invariant stets can be characterised by their Lyapunov spectrum. If all Lyapunov exponents of an invariant set are negative, it is called asymptotically stable. One vanishing Lyapunov exponent among negative ones characterises a stable periodic orbit. If the phase flow enforces two distinct periodic motions with incommensurable frequencies along two directions in phase space, *quasi-periodic* oscillations are observed. Such a set corresponds to a two dimensional torus. Two vanishing Lyapunov exponents among negative ones characterise these tori. A not periodic and bounded solution whose dynamics is sensitive to the initial conditions is called chaotic. Such solutions are governed by *chaotic attractors*. These are invariant sets in phase space which are locally unstable but globally stable. Thus, they are characterised by at least one positive and one vanishing Lyapunov exponent among negative ones. Note that they cannot be distinguished (by only considering the Lyapunov spectrum) from periodic saddles, which have positive and negative Lyapunov exponents among one that is zero (theses invariant sets

[12] Nevertheless, saddles repel trajectories as well in all practical situation, since a little perturbation along an unstable direction is enough for a trajectory to diverge.

[13] In this context, the temporal mean is defined as follows: $\langle g \rangle_t = \lim_{t\to\infty} \frac{1}{t} \int_0^t g(t')\,\mathrm{d}t'$

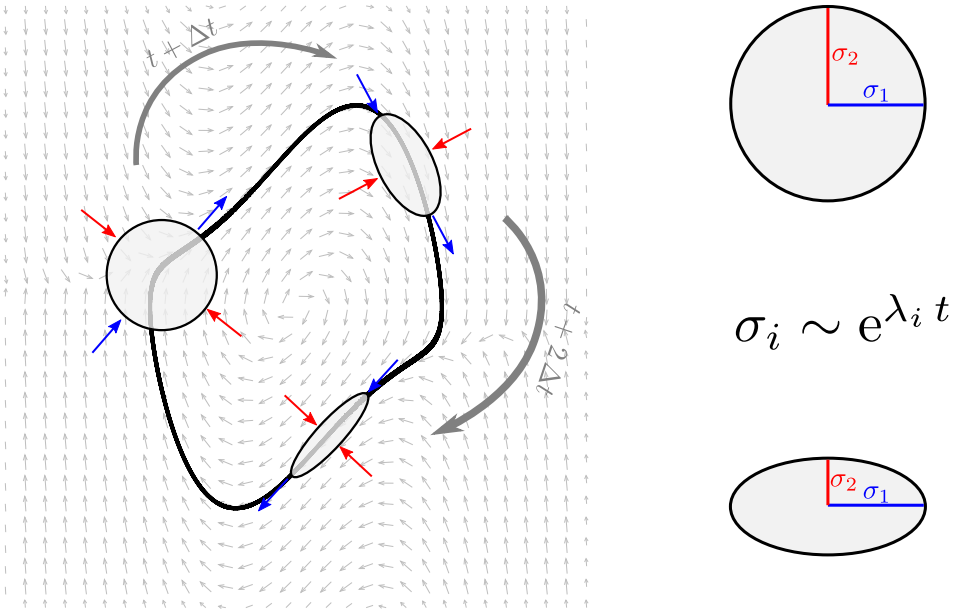

Figure 2.8.: Sketch of a phase volume which shrinks in one direction (red arrow) while it travels around a periodic orbit along an other direction (blue arrow). Its principal components σ_i change accordingly. Their mean temporal rate of change is given by the corresponding Lyapunov exponent λ_i.

are locally and globally unstable). This is due to the fact that the notion of Lyapunov exponents utilises the linearised system of equations of a nonlinear dynamical system. Thus, Lyapunov exponents only measure local stability. Only nonlinear systems which have a (at least) three dimensional phase space can feature chaotic attractors[14].

At least three different kinds of invariant sets occur later in this thesis. Among them are chaotic and quasi-periodic attractors. However, the most notable ones are periodic orbits, since they feature the most important class of solutions of the mathematical models developed. Especially their stability, in dependence of the system parameters, will be analysed. For investigating how properties of invariant sets change with system parameters, bifurcation theory is utilised.

2.4.3. Bifurcation theory

A sudden change of the topology of the phase flow is called *bifurcation*. These are linked to invariant sets which change their stability or state of existence, while one or more parameters of the system under study are varied. Bifurcations are named depending on the type of topological change, or the class, number and dimension of the invariant sets involved. There is a vast number of bifurcations one can distinguish, especially if systems of higher dimensionality are considered. One can group bifurcations by the number of system parameters which have to change for the bifurcations to occur. This number is called *codimension*. A *saddle-node* bifurcation is a pair production of a stable node or stable limit cycle and a saddle or semi-stable limit cycle. After a supercritical *Poincaré–Andronov–Hopf* bifurcation, a stable limit cycle is born or ceases to exist, while it grows out or collides with an unstable node; the node becomes stable after collision. Both are bifurcations of codimension one. The supercritical *Neimark-Sacker* bifurcation is of codimension two. It is similar to the Hopf bifurcation, but an invariant torus grows out or collides with a limit cycle in a shrink hose like manner. To detect a bifurcation in general, one tries to observe how the number of invariant sets and their eigenvalues or Lyapunov spectrum change.

Lets consider the following system as an example.

$$\dot{x}_1 = f_1(x_1, x_2) = -a + x_1^2 \tag{2.23a}$$

$$\dot{x}_2 = f_2(x_1, x_2) = -x_2 \tag{2.23b}$$

The system in Eq. (2.23) has a two dimensional phase space consisting of x_1 and x_2 and features a saddle-node bifurcation of fixed points when its only parameter a is varied. Its phase space portrait is shown in Figure 2.9 for different values of a. It can be seen that no fixed point exists at $a = -0.2$ and how a stable node and a saddle are born while a changes sign. Note how the vectors of the phase flow change continuously although its topology does not. For a better understanding the position of the fixed points and their eigenvalue spectrum can be considered. The position of the saddle is given by $\boldsymbol{x}_s = (\sqrt{a}, 0)^{\mathrm{T}}$ and the one of the node by $\boldsymbol{x}_n = (-\sqrt{a}, 0)^{\mathrm{T}}$. Their eigenvalue spectrum

[14] Reminder: Only continuous systems are considered here. Systems in which time flows in discrete portions do not have to be (at least) three dimensional to feature chaotic solutions.

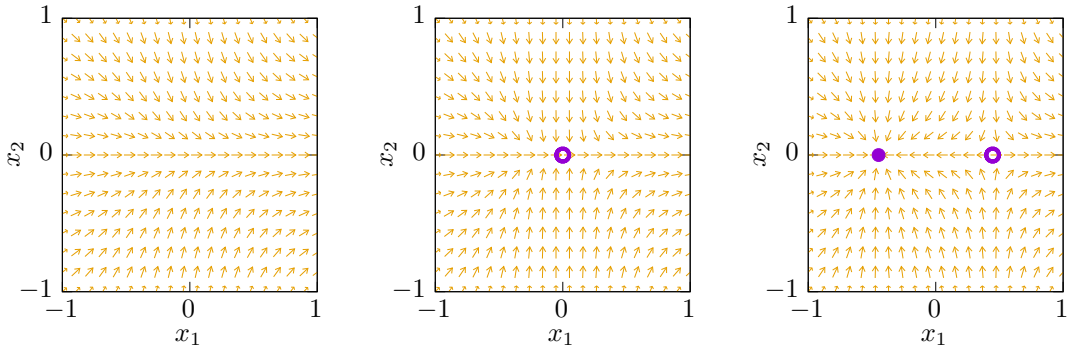

(a) $a = -0.2$. (b) $a = 0$. (c) $a = 0.2$.

Figure 2.9.: Phase space portraits of system Eq. (2.23) undergoing a saddle-node bifurcation while the parameter a is varied. The arrows denote the direction of the phase flow. The solid circle represents the asymptotically stable node while the other marks the saddle. The bifurcation happens at $a = 0$.

is given by $\{2\sqrt{a}, -1\}$ and $\{-2\sqrt{a}, -1\}$ respectively. It can be shown that both lose their stability properties along x_1 at $a = 0$ and that their positions, considering a real phase space, are not well defined anymore if $a < 0$. Exactly at $a = 0$ they are identical.

For better visualising the event, one can draw a *bifurcation diagram* as shown in Figure 2.10. Usually, invariant sets are represented by a scalar in a bifurcation diagram. This could be the maximal positive amplitude of an oscillation caused by a stable periodic orbit for example. Here, the x_1 phase space positions of the fixed points are chosen. The change of this scalar is observed in dependence of the parameter varied. By additionally visualising the stability properties of the invariant sets, they can be distinguished from each other. Note that this kind of visualisation is a mere projection of the bifurcation behaviour rather than a comprehensive picture. Although a saddle-node bifurcation of two limit cycles would look very similar, its implication on the phase space dynamics is very different (or at least of higher dimensionality). To better visualise and analyse the change of phase space dynamics caused by bifurcations, a clever way of reducing the dimensionality of the problems is useful. One of those ways is the application of a *Poincaré surface*.

To explain the concept of a Poincaré surface, the following three dimensional system, called *Rössler* system, shall aid as an example. It comprises three parameters and in dependence on those, it is able to exhibit periodic as well as chaotic dynamics.

$$\dot{x} = -y - z \tag{2.24a}$$
$$\dot{y} = x + a\,y \tag{2.24b}$$
$$\dot{z} = b + z\,(x - c) \tag{2.24c}$$

The values[15] of two of the three parameters will stay fixed at $a = 0.2$ and $c = 5.7$.

[15]The values have been taken from [47].

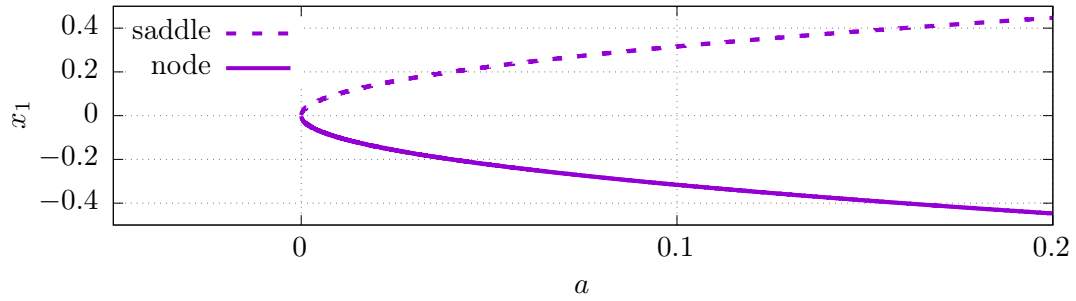

Figure 2.10.: Bifurcation diagram of system Eq. (2.23) showing a saddle-node bifurcation when the parameter a is varied. The solid line denotes the x_1 position of the asymptotically stable node, while the dashed line marks the saddle. The bifurcation happens at $a = 0$.

b is considered as the bifurcation parameter. In dependence of b, the properties of the Rössler attractor will be discussed. The Figures 2.11a, 2.11b, and 2.11c show three phase space portraits of the Rössler attractor which differ with respect to b. At $b = 1.6$ the Rössler attractor is a period one orbit (see Figure 2.11a). As the bifurcation parameter decreases, two period doubling bifurcations happen; leaving the Rössler attractor as a period four orbit at $b = 0.8$ (see Figure 2.11b). At $b = 0.4$ the Rössler attractor exhibits attracting chaotic dynamics (bounded, quasi-periodic dynamic which is sensitive to the choice of initial conditions; or rather globally stable but locally unstable dynamics). To visualise this behaviour in form of a bifurcation diagram, a Poincaré surface is applied. It is a hyperplane in phase space defined by fixing the value and the sign of the derivative of one dynamic variable. A part of the Poincaré surface for $y = 0$ and $\dot{y} < 0$ is shown in each phase portrait as blue square (see Figure 2.11a for example). The surface is chosen in such a way that the orbit under study intersects it. In the Poincaré surface, orbits are represented by their intersection points. Single points correspond to periodic orbits, while a dense point cloud is created by the intersection of a quasi-periodic or chaotic orbit. This kind of mapping reduces the dimension of the bifurcation problem under study by one.

One of the points' coordinates, with respect to the chosen Poincaré surface, might be choose as a scalar, representing the invariant set under study in a bifurcation diagram. Such a bifurcation diagram, showing the bifurcation behaviour of the Rössler attractor, is shown in Figure 2.11d. This time, different branches do not represent other invariant sets, as it was the case with the bifurcation diagram shown in Figure 2.10. The number of branches corresponds to the number of windings of the Rössler attractor as long as it is periodic. By observing how the image of the Rössler attractor on the Poincaré surface changes while varying the bifurcation parameter b, its bifurcation behaviour can be seen. After some period doubling bifurcations (branching), chaotic windows alternate with periodic ones while decreasing b. Note that both, quasi-periodic dynamics and chaotic dynamics produce a dense point set on the Poincaré surface. That means that

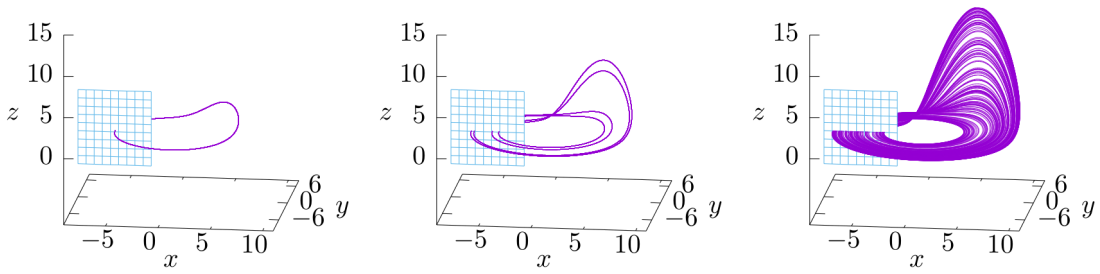

(a) Period one orbit at b=1.6. (b) Period four orbit at b=0.8. (c) Chaotic attractor at b=0.4.

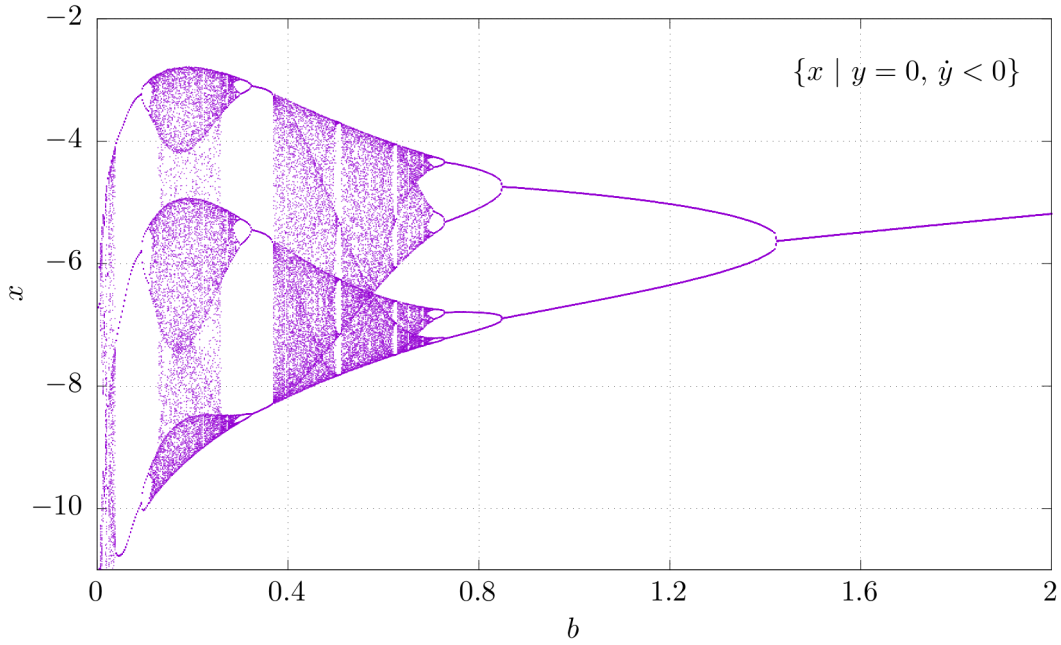

(d) Bifurcation diagram created with the Poincaré map defined in top right corner. Several period doublings (branch points) can be observed before the system becomes chaotic (point cloud).

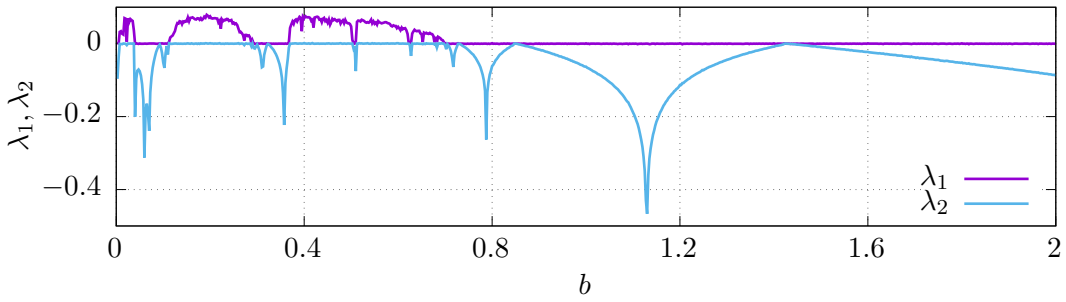

(e) Two largest Lyapunov exponents of the system in dependence on the bifurcation parameter. If the largest exponent is positive, the system exhibits chaotic dynamics.

Figure 2.11.: Bifurcation behaviour of the Rössler system Eq. (2.24). (a), (b), (c) The attractor of the Rössler system is reduced to a set of points on a Poincaré surface. (d) The x position of this points represents the attractor in a bifurcation diagram. (e) Additionally, the two largest Lyapunov exponents are shown. Everywhere where $\lambda_1 > 0$ and $\lambda_2 = 0$ the systems exhibits chaotic dynamics.

one cannot distinguish between them by only considering the bifurcation diagram.

To overcome this problem, the Lyapunov spectrum of the Rössler attractor has to be considered. Figure 2.11e shows the two largest Lyapunov exponents of the system in dependence of the bifurcation parameter b. Note how one Lyapunov exponent is always equal to zero while the others are negative in the case of a periodic motion, as discussed before in context of a growing or shrinking phase space volume (see Figure 2.8). Every time a dense point set can be seen in the bifurcation diagram, the largest Lyapunov exponent is larger than zero, indicating local instability thus chaotic dynamics in this case.

2.5. Concept of synchronicity

In 1665, the Dutch scientist Christian Huygens reported about a phenomenon nowadays referred to as synchronisation. Huygens observed that after some time, two pendulums clocks, mounted on a common support, started to tick at the same moments. He concluded that little amounts of energy, which passed though their common support, must have lead to that behaviour. Thus the "*sympathy of two clocks*" is caused by their *coupling* via their support. In this section the notion of synchronisation is discussed to an extent which is utile in order to provide a better understanding of the work conduced in the context of this thesis. As a reference the textbook written by Pikovsky et al. [48] was used.

Freely translated, "synchronous" means "at the same point in time". In more mathematical words, one would consider two systems as acting synchronous if there is a perfect temporal correlation between them. *Synchronisation* describes the process after which two systems are synchronised. Thus, the term synchronisation has a causal extent. Two uncoupled systems could exhibit synchronous dynamics by chance but only two coupled systems can synchronise. In the context of this thesis, only the latter case, synchronicity induced by a causality, is meant when speaking about synchronous systems. Furthermore, the notion of synchronicity in terms of a perfect temporal correlation shall be relaxed. Two systems will be called synchronous if the current state of the first system can be inferred by only knowing the current state of the second one and vice versa. These definitions translate to systems comprising multiple coupled units as well.

Usually synchronisation can occur in two ways. In the first case, a unit synchronises with another one, which in turn influences or drives the first, in terms of a master-slave relation (unidirectional coupling). In the second case, multiple similar units synchronise with each other because of a mutual influence (bidirectional coupling). The latter case is called *mutual synchronisation*. Only mutual synchronisation of self-sustained oscillators is analysed in this thesis.

2.5.1. Self-sustained oscillators

Systems which exhibit self-sustained oscillations, thus featuring a asymptotically stable limit cycle[16] in phase space as solution, are called self-sustained oscillators. In terms of physics, self-sustained oscillators have an internal energy source which is used to maintain their oscillatory motion even in the presence of damping or perturbations. A pendulum clock is an example for a self-sustained oscillator. Its pendulum performs a periodic oscillatory motion which is maintained by the potential energy of its weights. Although small perturbations of the pendulum add an offset to its motion with respect to time, its oscillatory behaviour is unaffected.

To illustrate the dynamics of a self-sustained oscillator and to compare these with the dynamics of a not self-sustained oscillator, the following two systems are considered: the

[16] Of course there are (self-sustained) chaotic oscillators as well, but they are neglected here for didactic reasons.

Van der Pol oscillator

$$\dot{x}_1 = x_2 \tag{2.25a}$$
$$\dot{x}_2 = \mu \left(1 - x_1^2\right) x_2 - \omega^2 x_1 \tag{2.25b}$$

and the harmonic oscillator

$$\dot{y}_1 = y_2 \tag{2.26a}$$
$$\dot{y}_2 = \omega^2 y_1. \tag{2.26b}$$

Figure 2.12 shows the dynamics of the self-sustained Van der Pol oscillator and compares its phase space portrait with the one of the harmonic oscillator. The phase flow of the Van der Pol oscillator features, besides an unstable fixed point at the origin, a global attracting limit cycle (see Figure 2.12a). Almost all initial conditions converge towards this limit cycle and perform a periodic motion after their transient time (see Figure 2.12c). Thus, perturbations will decay and the system goes back to the periodic motion compelled by the limit cycle. The "internal energy source" of the Van der Pol oscillator is given by the nonlinear damping present in Eq. (2.25b). It pumps energy into the system if trajectories are inside the limit cycle and drains energy from it if trajectories are outside the limit cycle.

The phase flow of the harmonic oscillator features a dense family of periodic orbits around its fixed point at the origin. Three of those are shown in Figure 2.12b. This means that the whole phase space is filled with invariant sets. Thus, every initial condition will produce a trajectory which stays on the invariant set from which the initial condition was chosen. Perturbations will neither grow nor decay but lead to periodic oscillations with a different amplitude than the unperturbed trajectory. This is due to the fact that the harmonic oscillator does not comprise an inner energy source or sink but is energy conserving.

2.5.2. Notion of the phase

Often, the phases of periodically oscillating systems are used to detect and classify synchronisation between them. The *phase* φ is defined as follows: "The phase of a periodic oscillator grows uniformly in time and gains $2\,\pi$ at each period." [48]. Lets consider T as the temporal length of one oscillation cycle, usually called *period*. The phase of a periodic oscillator keeps count of the number of oscillation cycles passed $(t - t_0)/T$, after a time t_0, as multiple[17] of $2\,\pi$.

$$\varphi = 2\,\pi \cdot \frac{t - t_0}{T} + \varphi_0 \tag{2.27}$$

The offset φ_0 can be used to define a starting point of the oscillation cycle and to account for perturbations, which transport the state of the oscillating system along its limit cycle, thus suddenly increasing or decreasing its phase. Note the very importance

[17] This factor is used for mathematical convenience.

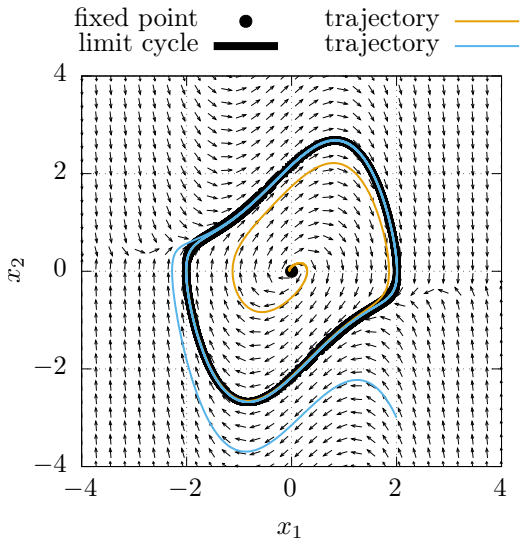

(a) Phase space portrait of the Van der Pol oscillator comprising its fixed point and two trajectories converging towards its limit cycle.

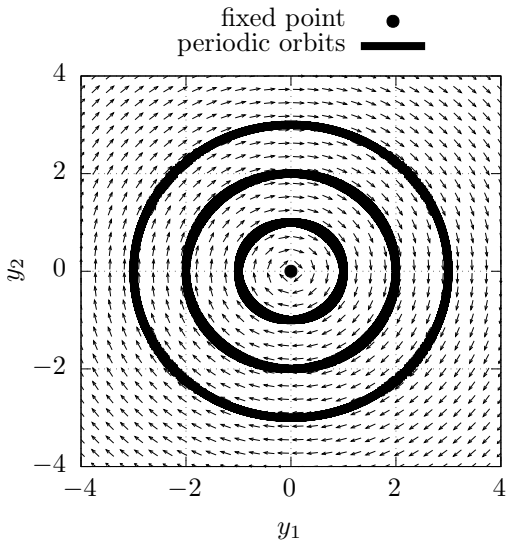

(b) Phase space portrait of the harmonic oscillator comprising its fixed point and three of its dense packed periodic orbits.

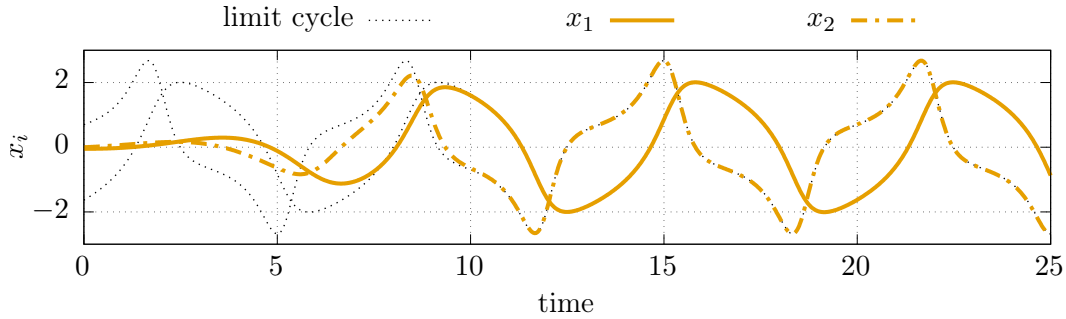

(c) Oscillations of the Van der Pol oscillator in the time domain. It can be seen how its dynamic variables (orange) converge towards the periodic oscillation behaviour (black) compelled by its limit cycle.

Figure 2.12.: Dynamics of a self-sustained oscillator, the Van der Pol oscillator, in phase space and in the time domain. Furthermore, the phase space portrait of the Van der Pol oscillator is compared with the portrait of the harmonic oscillator. The parameter values $\mu = \omega = 1$ have been used.

of the latter statement; since this is the only difference between a dimensionless number, which counts time in terms of oscillation cycle length T, and a phase, which counts passed oscillation cycles. Note further that the mere term "phase" is used ambiguously in different contexts, like in "phase space". There, for example, the term "phase" denotes a state of the system under study in general. Fortunately, it can be inferred from the context what is meant in most cases.

If a trajectory, which lives on a stable limit cycle, is perturbed, this perturbation will decay in time, but only with respect to the amplitude or rather the form of oscillation. Since the direction along the limit cycle is only neutrally stable (see Figure 2.8) perturbation or projections of perturbation on this direction will neither grow nor decay. This is illustrated by Figure 2.13. Figure 2.13a shows the phase space portrait of a self-sustained oscillator featuring one stable limit cycle. If a trajectory on top of this limit cycle is perturbed, it will relax towards the limit cycle but might be transported along it, which leads to a phase shift. This becomes more evident in the time domain. Figure 2.13b shows an oscillation generated by the same limit cycle. After some time, this oscillation is perturbed. The resulting oscillation is quantitatively identical with the unperturbed one but features a phase shift $\Delta\varphi$ with respect to it.

To summarize, the phase of an oscillation counts the numbers of passed oscillation cycles as multiples of $2\,\pi$ and is neutrally stable. Thus, a general perturbation, although decaying in time with respect to the amplitude of oscillation, leads to a phase shift. By reviewing the Lyapunov spectrum of limit cycles: "the phase can be considered as a variable that corresponds to the zero Lyapunov exponent." [48]. Especially the latter property of the phase is crucial for oscillators to synchronise.

2.5.3. Mutual synchronisation

In the beginning of this section, synchronisation was defined as the process which leads to temporal correlated oscillation of multiple coupled units. For two oscillators to synchronise it is necessary for them to be coupled, since correlated oscillations by chance are not considered as being the result of a synchronisation process. However, if it is known that two oscillators are coupled, they have synchronised if and only if their oscillations are correlated. In this context, the term correlation is used as the possibility to infer the state of one oscillator by only knowing the state of the other[18]. Or in other words, coupled oscillators are synchronised with each other if and only if they are *phase locked*[19]. In the most simple way of phase locking, the phase difference $\Delta\varphi$ of two oscillators is constant in time.

$$\varphi_2 - \varphi_1 = \Delta\varphi = \text{const.} \tag{2.28}$$

This definition of phase locking is sufficient for all cases considered in this thesis. There is a more relaxed definition though, which states that the ratio of the phases of two

[18] This means that to coupled oscillators which exhibit a sinusoidal oscillation, with a mutual phase shift of $\pi/2$, are still considered to be correlated.

[19] There are more relaxed definitions which cover the synchronisation of chaotic oscillators.

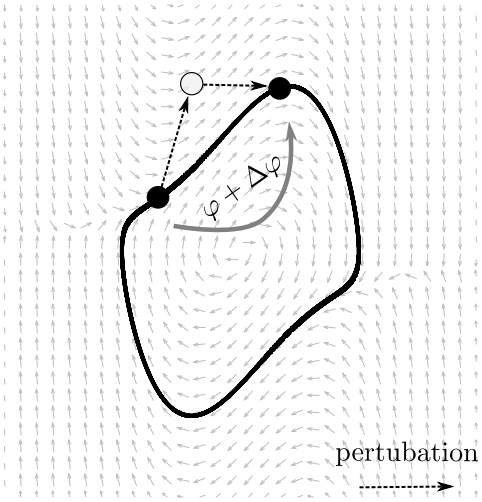

(a) Phase space portrait of a limit cycle. If trajectories on a stable limit cycle are perturbed, they will converge towards it again. Nevertheless, they experience a phase shift $\Delta\varphi$ caused by perturbations along the limit cycle and by their transient time.

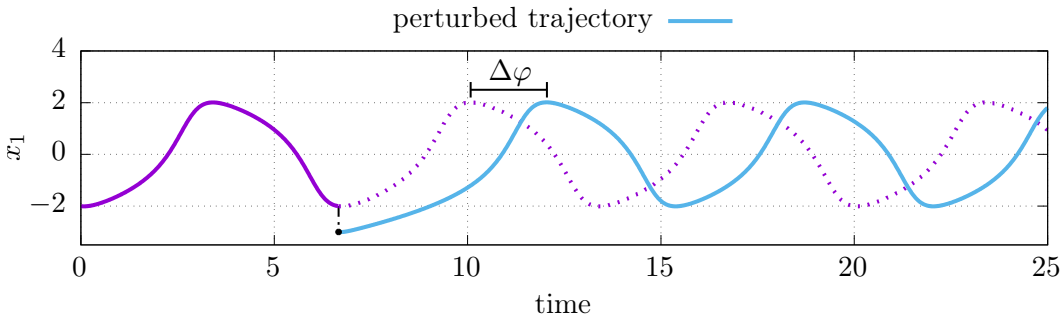

(b) Oscillations caused by a stable limit cycle in the time domain. The oscillations are stable with respect to their amplitude or rather the quantitative form of oscillation. Nevertheless, a perturbation will lead to a phase shift $\Delta\varphi$.

Figure 2.13.: Phase space portrait of a self-sustained oscillator and oscillations generated by it illustrating how perturbations of trajectories lead to phase shifts.

oscillators has to be rational and constant for them to be phase locked.

$$\frac{\varphi_2}{\varphi_1} = \frac{m}{n} = \text{const.} \quad \text{with} \quad n, m \in \mathbb{Z} \tag{2.29}$$

The ratio of $m/n = 1/2 \Leftrightarrow \varphi_2 = 2\,\varphi_1$ would mean that after oscillator 2 has finished two cycles, oscillator 1 has finished one.

To illustrate the concept of synchronisation further, the following system of two coupled Van der Pol oscillators is considered.

$$\dot{x}_1 = x_2 \tag{2.30a}$$
$$\dot{x}_2 = \mu_x \left(1 - x_1^2\right)\, x_2 - \omega_x^2\, x_1 + k\,(y_1 - x_1) \tag{2.30b}$$
$$\dot{y}_1 = y_2 \tag{2.30c}$$
$$\dot{y}_2 = \mu_y \left(1 - y_1^2\right)\, y_2 - \omega_y^2\, y_1 - k\,(y_1 - x_1) \tag{2.30d}$$

The Van der Pol system is already known from Eq. (2.18) and Eq. (2.25). Here, $\boldsymbol{x}$ and $\boldsymbol{y}$ denote the dynamic variables of the first and second oscillator respectively. Their coupling is given by the term $k\,(y_1 - x_1)$, where k is the coupling strength. The damping coefficients are considered to be equal henceforth $\mu_x = \mu_y = \mu = 1$. If the natural frequencies of the oscillators ω_x and ω_y are equal as well, the oscillators are called identical; and nonidentical otherwise. Synchronisation of identical oscillators is considered first. Figure 2.14a shows how two identical Van der Pol oscillators oscillate uncoupled ($k = 0$ at $t < 40$) and how they synchronise after the coupling is switched on ($k = 1$ at $t \geq 40$). Before the coupling is switched on, the two oscillators were phase locked by chance since they have identical frequencies. Again, oscillators are not considered synchronised if their phase locking is not due to causality or rather coupling. After the coupling is switched on and after some transients have ceased, the two oscillators are perfectly synchronised with a constant and phase difference of $\Delta\varphi = 0$.

Figure 2.14b shows the synchronisation of two nonidentical ($\omega_y - \omega_x = 0.1$) Van der Pol oscillators. Again, the oscillators are uncoupled at $t < 40$ and coupled afterwards ($t \geq 40$). Before the coupling is switched on, it can be seen how the nonidentical natural frequencies leading to a varying phase difference between them. After the coupling is switched on and after some transient oscillations have ceased, the two oscillators are synchronised. Here, the synchronised state has two characteristics. First, the phase difference is not exactly zero; second, the amplitude of the second oscillator is smaller than the amplitude of the first one. Both are caused by the different natural frequencies which break the symmetry of the coupled system. Only an infinite large coupling strength would compensate for that.

It was already mentioned that the phase of an oscillator is neutrally stable. Thus, perturbations of the phase do neither grow nor decay. This neutral stability of the phase is the reason why oscillators are able to synchronise if they are coupled. Coupling means that one oscillator is able to "feel" the other's dynamic. Thus, the latter is influencing the former and vive versa. These influences can be interpreted as perturbations which change permanently the phase of the oscillators under consideration. These phase changes drive the coupled system into a state which features a symmetry compelled by the coupling.

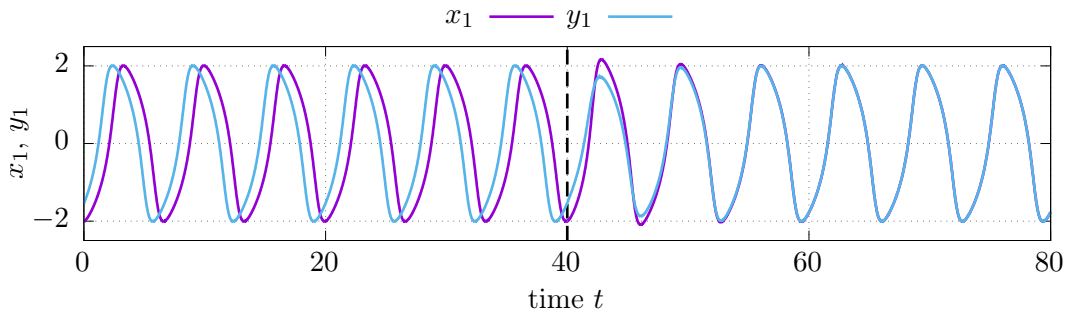

(a) Synchronisation of identical oscillators ($\omega_x = \omega_y = 1$).

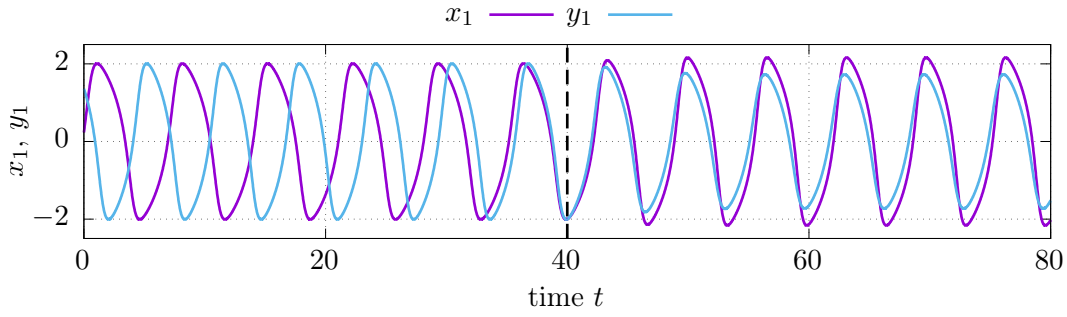

(b) Synchronisation of nonidentical oscillators ($\omega_x = 0.95$ and $\omega_y = 1.05$).

Figure 2.14.: Synchronisation of two coupled Van der Pol oscillators (see Eq. (2.30)). The black dashed line denotes the point in time ($t = 40$) at which the coupling is switched on ($k = 1$). The oscillators are uncoupled ($k = 0$) before. Furthermore, they do not differ with respect to their damping coefficient ($\mu_x = \mu_y = \mu = 1$).

Thus, identical oscillators which are coupled symmetrically have to synchronise with a phase shift of $\Delta\varphi = 0$ or $\Delta\varphi = \pi$ after a while; even if the coupling strength is infinitesimally small. A decreasing coupling strength only increases the transient time towards the synchronised state. If the oscillators are nonidentical, their own dynamical behaviour competes with the effect of the coupling. They only reach a synchronised state if the coupling strength is high enough to dominate the dynamics of the whole system. Nevertheless, the synchronised state cannot be perfectly symmetric since it has to account for the symmetry breaking introduced be the nonidenticality of the oscillators.

If a system exhibits periodical behaviour in time, this periodic state is represented as an one dimensional closed invariant set in phase space, namely a periodic orbit. The stable limit cycle of a self-sustained oscillator is an example. If two coupled oscillators are synchronised, the whole system, which comprises both of them and their coupling, exhibits periodic dynamics as well. Thus, the synchronised state, comprising the dynamic variables of the oscillators and their coupling, is represented as a periodic orbit as well. This means that the whole system could be considered a single high dimensional oscillator. In general, it cannot be distinguished from "outside" whether a high dimensional periodic system is comprised of synchronised subsystems or not, since all dynamic variables are "synchronised" with each other. Even by knowing the equations describing these systems, different choices of what the synchronised subsystems are might be possible[20]. Thus, although some choices might be more or less reasonable in different contexts, these choices are arbitrary and are only a classification introduced by the physicist analysing these systems.

[20] At least, a subsystem has to be able to exhibit oscillations to be considered synchronisable.

3. Oscillations of Cardiomyocytes

Premature cardiomyocytes exhibit self-sustained oscillations or rather beating. This beating behaviour was extensively studied. Early experiments accessed membrane currents and the transmembrane potential of myocardial fibre bundles in voltage clamp conditions [49]. This yielded information about the correlation between the depolarisation of the membrane potential and the contraction of the muscle fibres. Furthermore, they suggested the existence of a calcium storing and releasing unit inside the cells and its importance for their contraction behaviour. Nowadays, this unit is known as *sarcoplasmic reticulum*. RADMACHER et al. were the first who used *atomic force microscopy* (AFM) to observe the mechanical beating behaviour of single cardiomyocytes [7], and many followed. Today, many studies deal with the quantitative characterisation of the electromechanical properties of the beating of single cardiomyocytes, in terms of contraction force, beating frequency, intracellular calcium concentration, and membrane potential [8, 9, 10]. This chapter is dedicated to the analysis of the qualitative form of the beating signal of single premature cardiomyocytes.

Experiments were conducted by my colleague and collaborator Susanne Schlick[1], which yielded video data of beating premature cardiomyocytes embedded in a collagen hydro gel. This data were analysed with mathematical and image processing tools to extract time series which show the periodic beating of single premature cardiomyocytes.

The first section of this chapter explains the experimental setup used. After that, mathematical and image processing tools are introduced. The obtained results are discussed at the end of this chapter, followed by a short summary.

3.1. Experimental setup and video data

The medium of interest are in collagen I gel embedded cardiomyocytes. Together with fibroblasts, which remodel the collagen structure and thus influence the rheological properties of the gel [14], they are the active part of the medium.

The experiments yielded video data of the samples showing beating cardiomyocytes. These data were acquired using a camera attached to an optical microscope. All the videos have one channel with a bit depth of 8 bit, a resolution of 2048x1087 pixels, are stored in an uncompressed raw format (DIB[2] [50]) in an AVI container [51], and were recorded with a frame rate of 50 Hz.

Some snapshots of the videos acquired are shown in Figure 3.1. Figure 3.1a shows an unordered assembly of cardiomyocytes in different stages during their development. In

[1] Institute of Pharmacology and Toxicology, University Medical Center Göttingen
[2] A more common name for *Device-Independent Bitmap* (DIB) is *Bitmap* (BMP).

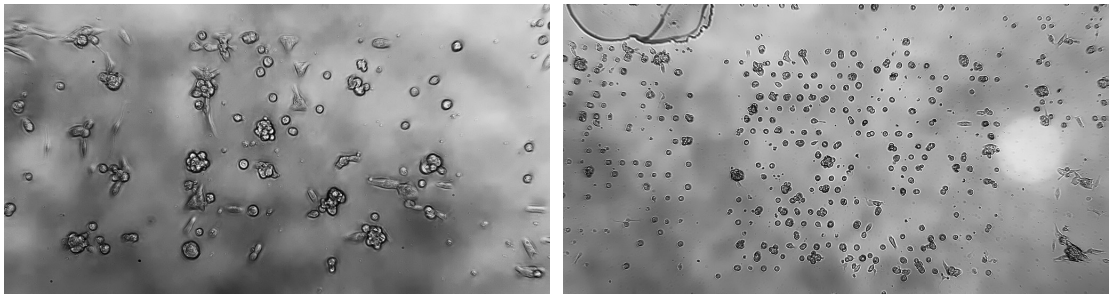

(a) Unordered structure of clustered and non clustered cardiomyocytes in different stages during their development.

(b) Rectangular assembly of mostly single premature cardiomyocytes.

Figure 3.1.: Two typical snapshots of the videos acquired during the experiments conducted by Susanne Schlick.

Figure 3.1b cardiomyocytes are shown, which are assembled in a rectangular structure. This structure is predefined by an underlying grid, allowing the cardiomyocyte only to attach to certain positions. It was developed by my colleague and collaborator Til Driehorst[3].

To understand what can be seen in the acquired video data, Figure 3.2 provides sketches of the most prominent components. These most prominent components are: beating and not beating premature cardiomyocytes (Figure 3.2a), beating and not beating elongated cardiomyocytes (Figure 3.2b), and clusters composed of the former mentioned (Figure 3.2c and Figure 3.2d). In a young medium, a lot of the unelongated premature cardiomyocytes can by found. As the medium grows older, the single cells form clusters and the cells inside a cluster beat in coherence. As the cardiomyocytes grow older they change their shape. They become longer and sink to the ground of the medium. The most interesting type with respect to the following analysis are the single beating premature cardiomyocytes.

3.2. Video analysis

To study the beating of single premature cardiomyocytes and to handle the large amount of video data[4], the original videos were cropped to regions of interest, which contain only one beating cell. In the same processing step each video was converted into a lossless compressed image sequence (TIFF [52]). FFmpeg [53] was used for this. The resulting images have a resolution of about 100x100 pixels. In the next processing step the image sequences were denoised, the global contrast was enhanced and an edge detection algorithm was applied. The image analysis tool Fiji [54], which is a version of ImageJ [55], was used for this purpose. Figure 3.3 summarises the mentioned preprocessing steps. In total, six cells were analysed. Pictures of the cells are shown in Figure A.1.

[3]Third Institute of Physics - Biophysics, Georg-August-University Göttingen; Institute of Pharmacology and Toxicology, University Medical Center Göttingen

[4]In terms of memory, one video is about five to six GB large.

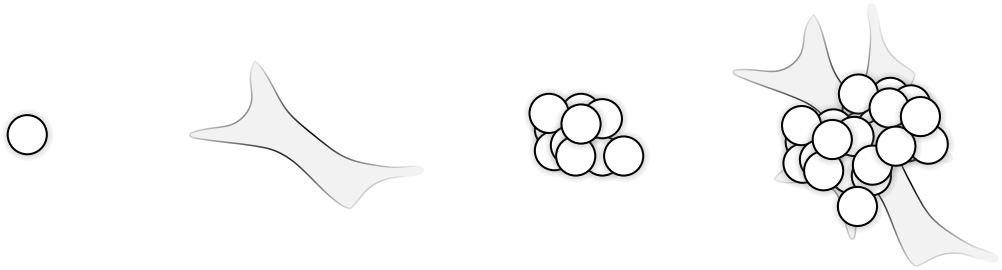

(a) Single premature cardiomyocyte. (b) Single elongated cardiomyocyte. (c) Cluster of premature cardiomyocytes. (d) Cluster of premature and elongated cardiomyocytes.

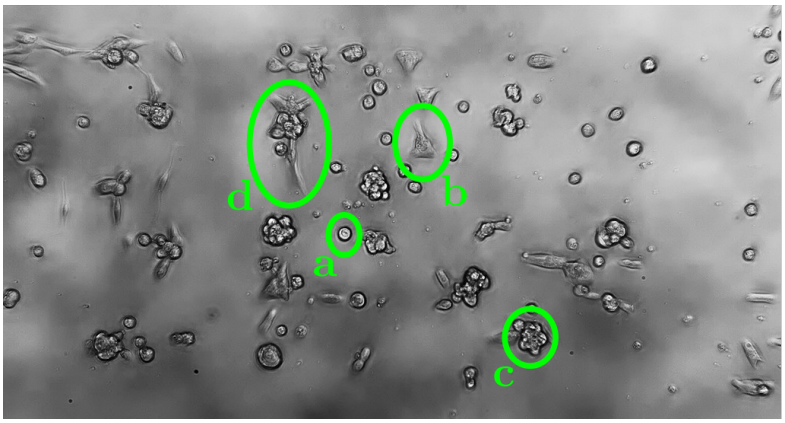

(e) Video snapshot with labelled cell structures.

Figure 3.2.: Sketches of the most prominent cellular components seen in the videos.

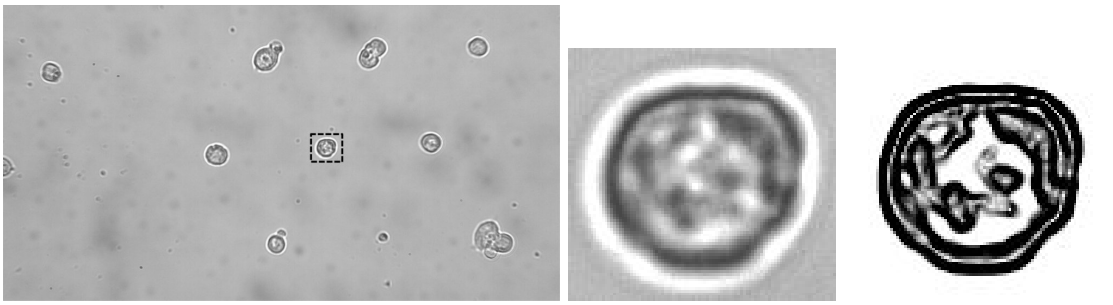

(a) Snapshot of a video containing several premature cardiomyocytes. (b) Snapshot of the cropped video containing only one cardiomyocyte. (c) Snapshot of the cropped and processed video emphasising the cell contour.

Figure 3.3.: Snapshots of one captured video showing the results of the preprocessing the videos undergo before the beating of the cardiomyocytes is analysed.

3.2.1. Signals of cellular beating

The goal of this analysis is to specify the *beating behaviour* of the cardiomyocytes. By *beating behaviour* any kind of rather periodic change of the cell's configuration in time is meant. This excludes all rigid body movements, like drift and rotation but includes for example periodic contraction and bending. Because the premature cardiomyocytes behave very differently with respect to each other, this broad definition of beating behaviour was chosen. To measure this property four different approaches have been followed.

Human eye approach The first approach was to watch the videos. In this way, a first general impression was obtained how the cells behave. Independent of the concrete representation of the beating, it could be seen that the temporal behaviour was the same for all cells. The cells change very fast from their reference configuration to their excited configuration[5]. If the maximum extent of their excited state is reached, they return to their reference configuration immediately. Although the change from the excited to the rest state is very fast as well, it happens in a rather asymptotic-like manner, in contrast to the change from the rest to the excited state. After the rest state is reached, the cells stay there for a certain amount of time until they go to the excited state again. Furthermore, the frequencies f of the cells can be determined by counting the beat events N_b and dividing that number by the total observation time t_o. The total observation time is given by the ratio between the number of observed frames N_f and the frames per second fps.

$$f = \frac{\text{fps}}{N_f} N_b \quad \text{with} \quad \sigma_f = \left| \frac{\text{fps}}{N_f} \sigma_{N_b} \right| \tag{3.1}$$

Table 3.1 shows the frequencies of the cells determined by eye. A counting error of $\sigma_{N_b} = 1$ was assumed.

Mean intensity approach The second approach to analyse the beating behaviour of the cells is to calculate a time series from the videos consisting of the mean intensities per frame. Obviously, this approach makes only temporal changes visible which alter the mean intensity of the frames. That means that movement or beating behaviour, which conserve the recorded cross section area of the cell cannot be observed with this method. Thus this method is robust against rigid body cell movements. On the other hand, high fluctuations of the background intensity (observed in some of the videos) lead to a very poor signal to noise ratio. In the following, this approach will be called *mean intensity approach*. Figure 3.4 shows an exemplary time series generated with the mean intensity approach. The shown signal was generated from the video of cell 1. The signal to noise ratio is relatively high compared to the other two approaches which will be discussed soon. Thus the form of the oscillation cannot be determined very well with this method. Nevertheless, the signal is good enough to estimate the frequency of the beating behaviour. It should be noted that the time series comprises

[5]The configuration which the cells occupy longest is called *reference configuration* or *rest state*. The state occupied shortest is called *excited configuration* or *excited state*. Note that this definition is rather arbitrary since it does not take the inner biological mechanisms into account.

Cell	Frequency	Figure
1	0.72 (±0.02) Hz	Figure A.1a
2	0.51 (±0.02) Hz	Figure A.1b
3	0.39 (±0.02) Hz	Figure A.1c
4	1.40 (±0.02) Hz	Figure A.1d
5	0.64 (±0.03) Hz	Figure A.1e
6	0.70 (±0.02) Hz	Figure A.1f

Table 3.1.: Frequencies of the cells determined from the videos by eye. The number of beating events was counted and divided by total temporal length of the video. The average frequency is 0.73 (±0.03) Hz.

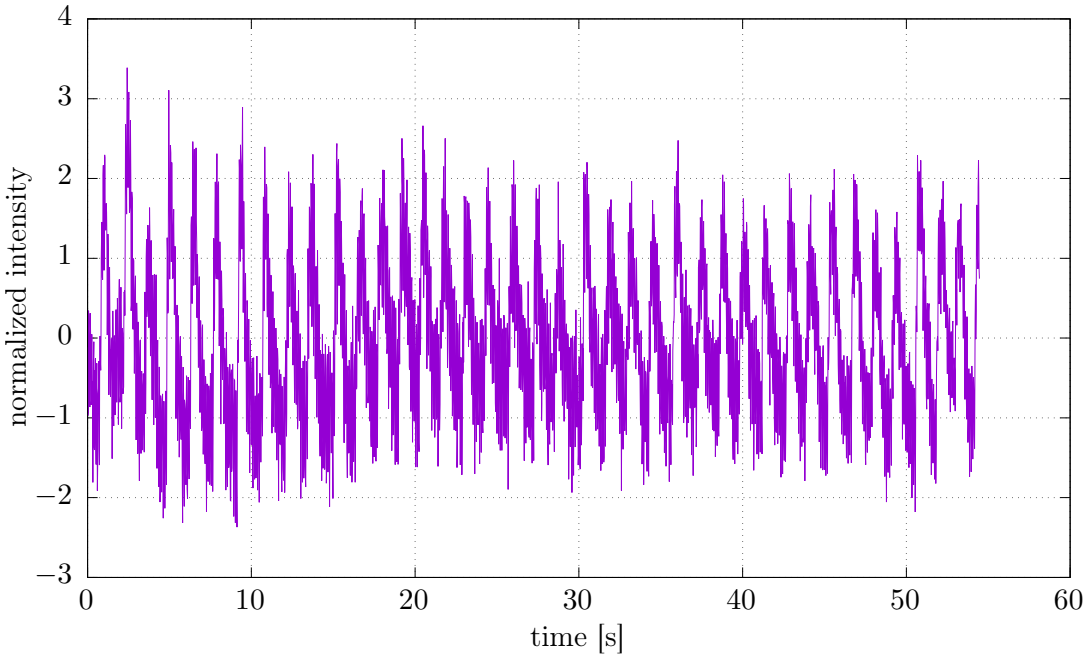

Figure 3.4.: Beating signal of cell 1 resulting from the mean intensity approach. Shown is the mean intensity of each video frame.

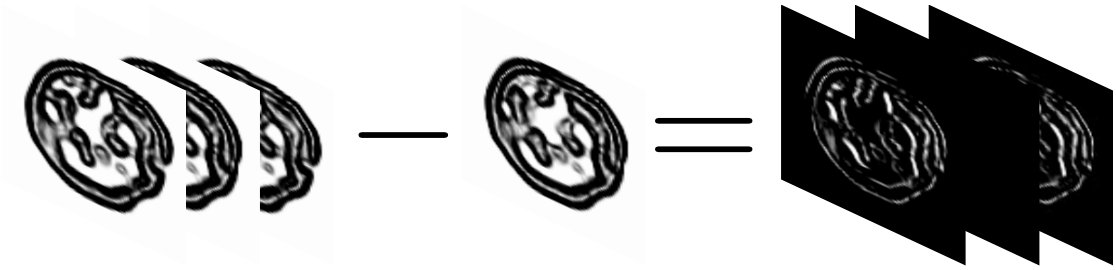

Figure 3.5.: Sketch showing how the beating of a cardiomyocytes can be visualised. A reference image is subtracted from the video resulting in a video showing only the deviations from the chosen reference frame.

negative values. This is because all the time series generated with this or the following approaches are normalised. This means that the temporal mean of the time series is removed by subtraction and that all values are divided by the standard deviation of the time series.

$$s(t) = \frac{s_{\text{measured}}(t) - \langle s_{\text{measured}} \rangle_t}{\text{STD}_t(s_{\text{measured}})} \tag{3.2}$$

Here $s_{\text{measured}}(t)$ denotes the time series directly generated by applying the approach under discussion and $s(t)$ it the normalised time series with vanishing temporal mean.

Reference frame approach The third approach is called *reference frame approach.* A reference frame is chosen and subtracted from the video. A time series is calculated from the resulting difference, which again comprises the mean intensities per frame. A sketch of the described method can be seen in Figure 3.5. Since this method makes visible any deviations from the reference frame, it suffers from rigid body cell movement. This means that the signal is best close (with respect to time) to the reference frame and it becomes poorer if it is farer away. To generate a meaningful signal over the whole time domain, a frame from the middle of each video is chosen as reference frame. On the other hand this approach is more robust against background noise, since it yields a stronger beating signal than the mean intensity approach. Figure 3.6 shows an exemplary time series generated with the reference frame approach. As one can see, the peaks indicating the beating of the cell are far more pronounced than in Figure 3.4, corresponding to the mean intensity approach. Furthermore, the cell drift can be seen clearly as the temporal distance to the reference frame increases. Again the signal was normalised as described above. Note that the signal shows a clear outlier at the point in time defining the reference frame. At this point, the unnormalised signal would be exactly zero. At every other point in time the background noise defines the ground level (larger than zero) of the signal. Another notable effect can be seen. The signal in Figure 3.6 is bifid. During, approximately, the first third of the signal the peaks point downward. Later they point upward. This is caused by the cell drifting past the position it occupies in the reference frame. In this case, the cell beats by stretching out one of its ends. The direction of this elongation coincides with the direction of the cell drift. While the cell is in front of its

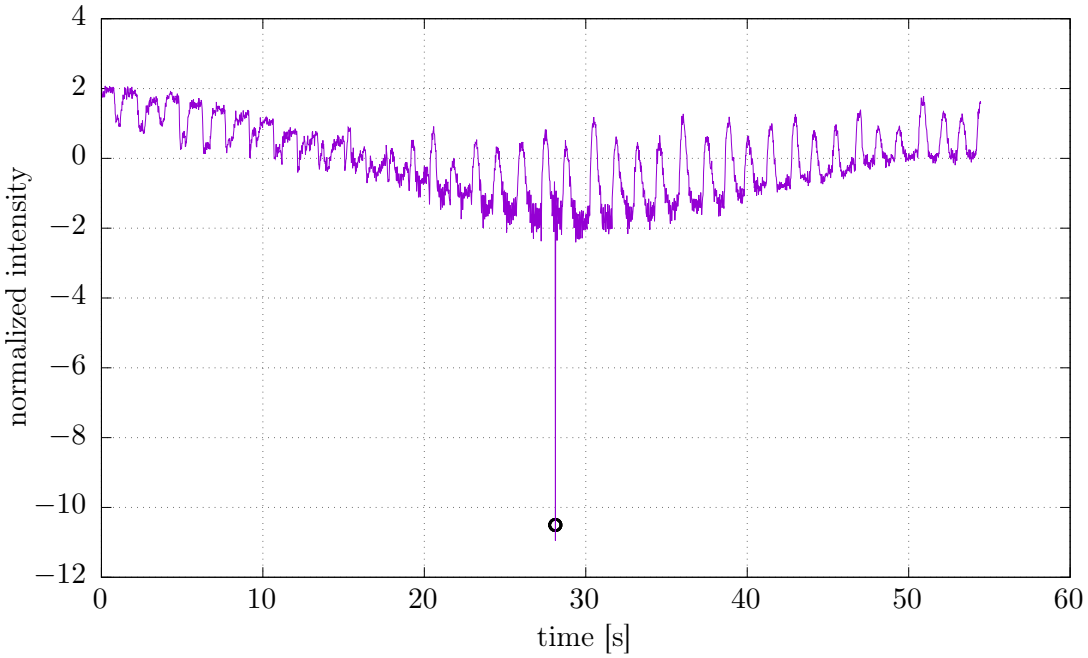

Figure 3.6.: Beating signal of cell 1 resulting from the reference image approach (Figure 3.5). An outlier is marked with a black circle.

reference frame position, it stretches into that position. Thus, the deviation from the reference position is smallest if the cell is in the excited state. As soon as the cell has reached its reference position, it stretches away from it. Thus, the deviation from the reference position is largest if the cell is in the excited state.

Active contour approach The fourth and last approach is called *active contour approach*. For each video frame, the outer contour of the cell is fitted by an active contour[6]. A principal component analysis is applied to each contour, to generate a scalar time signal, which consists of the first (largest) principal value. It is assumed that the beating of the cells happens along a distinct direction. This approach assumes further that even in the resting state, the cell is slightly more elongated along the direction of beating. If this assumption is not fulfilled, the first principal component of the cell contour does not uniquely measure the beating behaviour along the distinct direction of the cell, leading to a poor signal. On the other hand, this approach is very robust against background noise and does not suffer from rigid body cell movement.

For fitting the active contour to the outer contour of the cells, the MATLAB toolbox *Gradient Vector Flow (GVF) Active Contour* written by XU and PRINCE [56, 57] was used and adopted for convenience. It follows an explanation of how the mentioned software works. In general, the core algorithm places a parametrised (in our case closed) curve (active contour or snake) $\boldsymbol{x}(u) = [x(u), y(u)]$ in a force field. The force field is

[6] Active contours are sometimes called *snakes*.

defined by a provided image. Usually, the force vectors pointing toward regions of a large intensity gradient, thus make these regions attracting the snake. The antagonists, opposing the external forces, are the inner forces of the snake, given by its length and curvature. By minimizing the energy functional $E = \int_{\Gamma_u} E_{\text{int}}[\boldsymbol{x}(u)] + E_{\text{ext}}[\boldsymbol{x}(u)]\,\mathrm{d}u$, comprising external energy E_{ext}, defined as the potential energy of the force field, and internal energy E_{int}, given by the length and curvature of the snake, the snake is fitted to edges in the provided image.

In Figure 3.7 the computational steps regarding the active contour software are shown. The first step in using the software for fitting a snake to edges in an image is to provide an image whose intensity is defined in the right way. The attracting features of the image have to be regions of high intensity[7]. In the terminology of Xu and Prince, images following this definition are called *edge maps* (3.7b). The next task is to generate the external force field from the edge map. If one would just use the gradient of the edge map, one would face the following problem: Homogeneous regions do not provide any information, or even false information if noise is present. Thus, if the snake is initialised far away from the regions of interest, it will not be able to "see" the feature to be fitted. Xu and Prince overcame this problem by introducing their *gradient vector flow* (gvf) method. This method "diffuses" the vectors, generated by taking the gradient of the image, in a direction preserving manner. This yields the gradient vector flow field (3.7c), which is equivalent to the external force field deforming the snake. The generation of the gfv field depends on two parameters: the number of computational steps or rather the maximal time of diffusion and the regularization parameter μ. In general, μ defines the length scale of features which are present in the final gfv field. In the last step, the user has to define an initial snake and provide two parameters, α and β, which define how strong the snake's length and curvature is weighted against the influence of the gfv field. The parameters define the elasticity and stiffness of the snake. If everything works out, the initial snake is fitted to the image features of interest; the outer cell contour in the case of this thesis (3.7e). To summarise, the user has to provide the image of interest, the length α and curvature weights β, the regularization parameter μ, and has to choose the "diffusion time".

During this work, it was observed that all the mentioned parameters, including the quality of the image, influence the described fitting process in a very sensitive way. Thus, extensive fine tuning was necessary. A semi-automatic matlab script was written for this purpose. Note that the operational targets of the described algorithm are images and not videos or rather image sequences. For applying the algorithm in a convenient way for the purpose of cell contour tracking in the time domain, additional matlab routines had to be developed. It shall be mentioned that the fitting process itself is a non negligible error source with respect to the extracted cellular beating signals. Since the described algorithm depends sensitively on the provided parameters and since whole videos (comprising ~ 2700 frames) were needed to be analysed, it was not possible to fine tune the parameters for each single frame separately. This led to a number of frames where the fitting failed. Information extracted from those frames may lead to outliers

[7] In this thesis, zero intensity is associated with the colour black.

(a) The original image. The snake shall be fitted to the cell contour.

(b) The gradient of the original image is used to calculate the edge map.

(c) The edge map is converted into the gradient vector flow (gvf) field. The snake deforms in accordance with the force vectors.

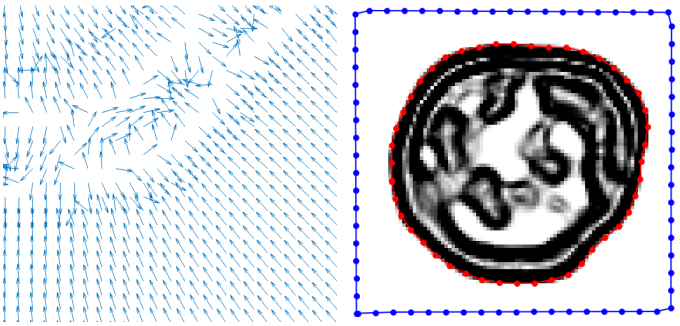

(d) Zoom into the the gradient vector flow field.

(e) Result of the fitting process showing the initial (blue) and the final (red) snake.

Figure 3.7.: Process of the active contour (snake) fitting. After the video underwent two frame wise preprocessing steps, an active contour was fitted to the cell contour in each video frame.

in the generated time series, which need to be filtered out.

After generating a series of contours $\hat{\boldsymbol{x}}_t(u) = [x_t(u),\, y_t(u)]$, a scalar time signal $s(t)$ should be extracted from those, which describes the beating behaviour of the cells. It is assumed that the beating happens along a distinct direction defined by the inner structure of the cell. The idea is to perform a principal component analysis of the contours in the spatial domain. As long as the cell is elongated, the vector corresponding to the largest principal value points into the direction of the largest variance (elongation) of the cell contour. Furthermore, this principal value is a measure of how large this elongation is. Thus, the time series comprising the largest principal values of the contour series represents the beating behaviour of the cell, if that beating happens along the direction of the largest elongation of the cell. It should be noted that u and t are discrete variables. $u \in [1, N_u]$ is the integer index of the coordinate pairs $[x_t(u),\, y_t(u)]$ whose union defines the snake at time point t. The number of coordinate pairs is given by N_u. The time t is related to the indices of the single video frames $i \in [1, N_i]$ via the recorded frames per second fps. The total number of video frames is given by N_i.

$$t = \frac{i}{\text{fps}} = i \cdot \Delta t \quad \text{with} \quad \text{fps}^{-1} = \Delta t \tag{3.3}$$

To generate the desired time series $s(t)$, the contour series $\hat{\boldsymbol{x}}_t(u)$ is transformed into its centre of mass coordinate system.

$$\boldsymbol{x}_t(u) = \hat{\boldsymbol{x}}_t(u) - \langle \hat{\boldsymbol{x}}_t \rangle_u \quad \text{with} \quad \langle \hat{\boldsymbol{x}}_t \rangle_u = \frac{1}{N_u} \sum_{u=1}^{N_u} \hat{\boldsymbol{x}}_t(u) \tag{3.4}$$

A principal component analysis of the contours is performed in the spatial domain. This can be done via a singular value decomposition.

$$\tilde{\boldsymbol{x}}_t(u) = \boldsymbol{x}_t(u)\, \boldsymbol{V}_t \quad \text{with} \quad \boldsymbol{U}_t\, \boldsymbol{S}_t\, \boldsymbol{V}_t^T = \begin{pmatrix} x_t(0) & y_t(0) \\ x_t(1) & y_t(1) \\ \vdots & \vdots \\ x_t(N_u) & y_t(N_u) \end{pmatrix} = \boldsymbol{x}_t(u) \tag{3.5}$$

Here $\tilde{\boldsymbol{x}}_t(u)$ are the transformed data. The singular values, found on the diagonal of $\boldsymbol{S}_t$, are equal to the principal values. The time series $s(t)$ representing the beating behaviour of the cells is given by the largest singular value.

$$s(t) = \max_i \operatorname{diag}(\boldsymbol{S}_t)_i \tag{3.6}$$

Figure 3.8 shows a beating signal generated with the active contour approach. One of the most prominent features of the signal are the outliers marked with a black circle. These result from an unsuccessful contour fitting. Compared to the signals generated with the mean intensity approach and the reference frame approach, this signal is rather noise free and it does not suffer from rigid body cell movement. Furthermore, the peaks are sharp and the slow approach towards the rest state is clearly visible. Although this

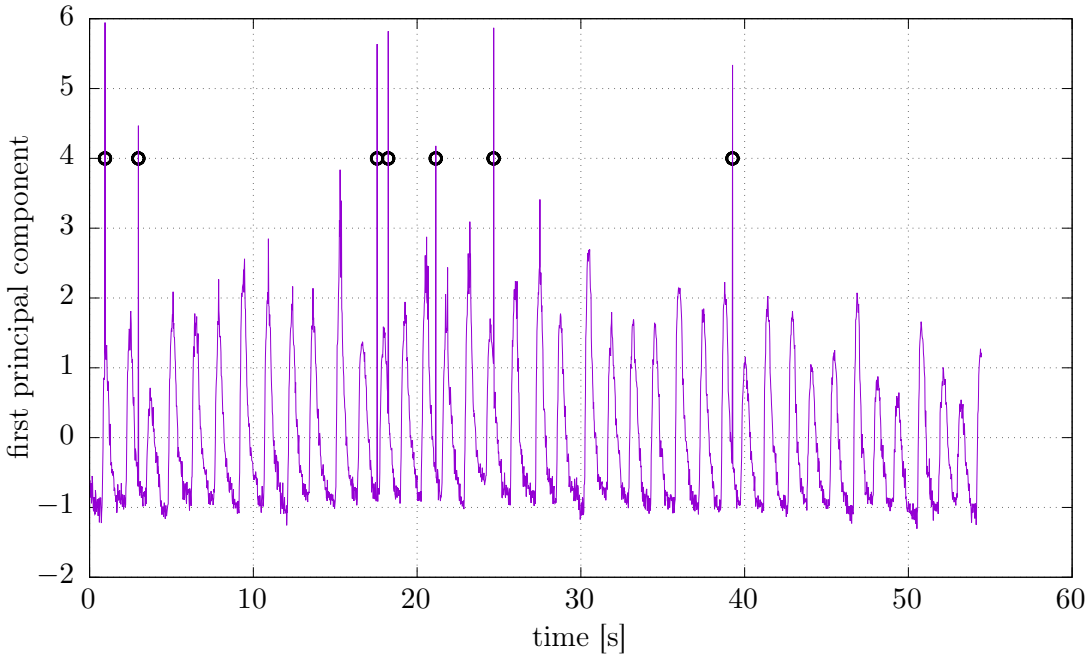

Figure 3.8.: Beating signal of cell 1 resulting from the active contour approach. Outliers resulted from an unsuccessful fitting process are marked with a black circle.

sounds like the active contour approach is superior to the other mentioned approaches, one should keep in mind the assumption which was made to generate a meaningful signal with the principal component analysis. Namely, that the cell beating happens along a distinct direction and that this direction corresponds to the largest principal component. This is a strict criterion not fulfilled by all cells. Since some cells buckle rather than contract, their beating cannot be geometrically described by the the longest axis of an ellipse which shortens and elongates. The active contour approach might break down as well if other objects beside the cells are present in the videos since the snake is fitted to them as well.

In general it is to say that the cell videos are diverse with respect to quality and other features. These features comprise background noise, closed or open cell contours, objects beside the cells, flickering of the background lightning, and so forth. Depending on the case at hand, the right approach, leading to a meaningful beating signal, has to be chosen. This can only be achieved by combining all approaches and deciding upon this broad data base.

3.2.2. Signal filtering

The generated time series give valuable information about the frequencies and the temporal form of the beating. Yet they also include features which do not relate to the beating itself, but to artefacts caused by the chosen approach or a sometimes poor qual-

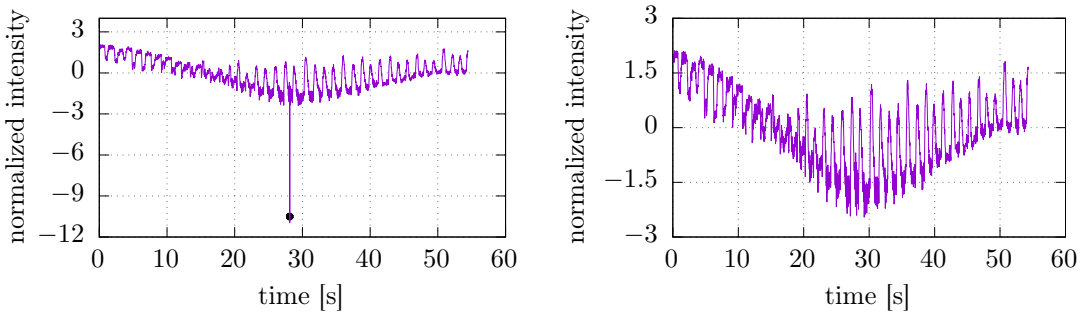

(a) Signal with outlier.

(b) Signal without outlier.

Figure 3.9.: Beating signal of cell 1 resulting from the reference frame approach before and after outliers were removed. After the filtering the signal was normalised.

ity of the video data. Those unwanted features can be removed by applying filtering methods yielding a clearer signal; clear in the sense that the signal mostly holds information about the beating behaviour of the cells. All generated time series underwent the same filter chain, which is explained in the following.

Outlier filter The first filtering is the removal of outliers. These outliers exist because of certain properties of the discussed approaches (see Sec. 3.2.1). The reference frame approach leads to one outlier at the very point in time at which the reference frame was chosen. Furthermore, if the fitting of the active contour to the outer cell contour fails in the active contour approach, outliers are produced as well. Outliers are defined as singular events in the time series which clearly diverge from the usual temporal behaviour. They are detected by eye. Either by looking at the time series itself or, in case of the active contour approach, by identifying the frames in which the fitting of the active contour failed. This is done by comparing the fit result with actual outer contour of the cell. Figure 3.9 shows the same time series before and after outliers were removed. It is to note that the time series is normalised again after it underwent the filtering process. This will be the case for all other filters discussed henceforth. An outlier with the index i^* is removed by deleting its value v_{i^*} from the time series $s(t_i)$ and shifting the following values backward in time. This results in the filtered time series $\hat{s}(\hat{t}_j)$.

$$s : t_i \to v_i \quad \text{with} \quad i \in [1,\, N_i] \tag{3.7a}$$

$$\hat{s} : \hat{t}_j \to \hat{v}_j \quad \text{with} \quad j \in [1,\, N_j] \quad \text{with} \quad N_j = N_i - 1 \tag{3.7b}$$

$$\hat{v}_j = v_k \quad \text{with} \quad k \in [0, N_i] \setminus i^* \tag{3.7c}$$

$$\hat{t}_j = t_j \tag{3.7d}$$

The number of samples of the unfiltered time series is given by N_i and the number of samples of the filtered time series is given by N_j. Note that this filtering technique changes the time scale of the signal. The unfiltered time signals comprise $N_i \approx 2700$

samples. Usually less then $\Delta N = N_i - N_j \approx 10$ samples are classified as outliers. Removing those samples results in a relative change of time scale of about $1 - N_i/N_j \approx 3 \cdot 10^{-3}$. This error, which is less than one percent, is considered negligible.

Band pass filter Undesired frequencies are removed from the beating signals next. This is done by simple band pass filtering. These frequencies can be caused by various reasons: Flickering of the microscope light source leads to high frequency noise in case of the mean intensity or reference frame approach; variations of the recorded thickness of the outer cell contour leads to noise in case if the active contour approach; and rigid body cell movement leads to low frequency noise in case of the reference frame approach. To remove those artefacts one has two know either the frequencies of those or the frequency of the desired beating signal. The latter is always known from the human eye approach or rather by the determinations of the beating frequency by eye (see Table 3.1). The lower boundary f_{low} of the frequencies which should remain in the filtered signal is given by halve of the beating frequency determined by eye f_{eye}. The upper bound f_{high} was chosen to be equal to 9 Hz.

$$f_{\text{low}} = \frac{1}{2} f_{\text{eye}} \tag{3.8a}$$

$$f_{\text{high}} = 9\,\text{Hz} \tag{3.8b}$$

Although the choice of the latter one sounds rather arbitrary, it is not. By investigating the frequency spectra of all the generated signals, it was observed that every kind of pronounced high frequency noise does not comprise frequencies less then 9 Hz. Furthermore, the fastest beating behaviour happens at about 1.4 Hz. Thus, by choosing the upper frequency bound to be 9 Hz, a large portion of the noise present in the signals can be removed while preserving the most important frequency components (up to six harmonics) of the beating signals. All high frequency noise is removed while leaving enough frequencies in the spectra for preserving at least six higher harmonics of the beating frequency. Usually only the first four harmonics are pronounced in the spectra.

The undesired frequencies are removed by transforming the unfiltered signal $s(t)$ into Fourier space $S(f)$. Frequencies beneath to lower bound f_{low} and frequencies above the upper bound f_{high} are removed from the spectra. The inverse Fourier transform of the filtered spectra $\hat{S}(f)$ yields the filtered signal $\hat{s}(t)$.

$$S(f) \equiv \mathscr{F}[s(t)](f) \tag{3.9a}$$

$$\hat{S}(f) \equiv \begin{cases} 0 & f < f_{\text{low}} \\ S(f) & \text{otherwise} \\ 0 & f > f_{\text{high}} \end{cases} \tag{3.9b}$$

$$\hat{s}(t) \equiv \mathscr{F}^{-1}[\hat{S}(f)](t) \tag{3.9c}$$

Figure 3.10 illustrates the described band pass filtering by comparing the spectra and the time series before and after filtering. It can be clearly seen in Figure 3.10c how

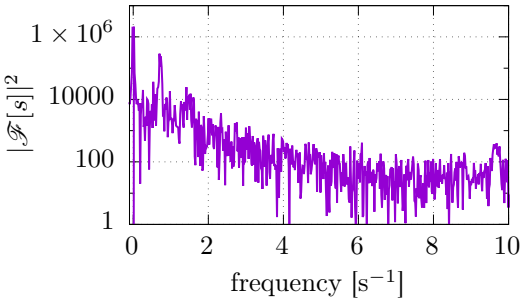

(a) Original frequency spectrum of $s(t)$.

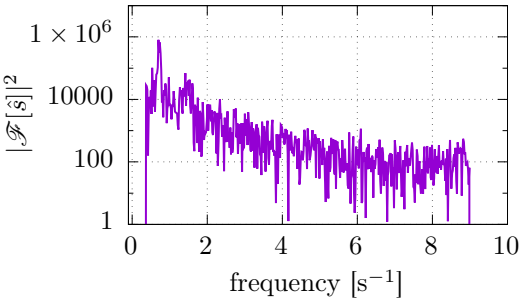

(b) Frequency spectrum of $\hat{s}(t)$ after band pass filtering. Undesired frequencies are set to zero.

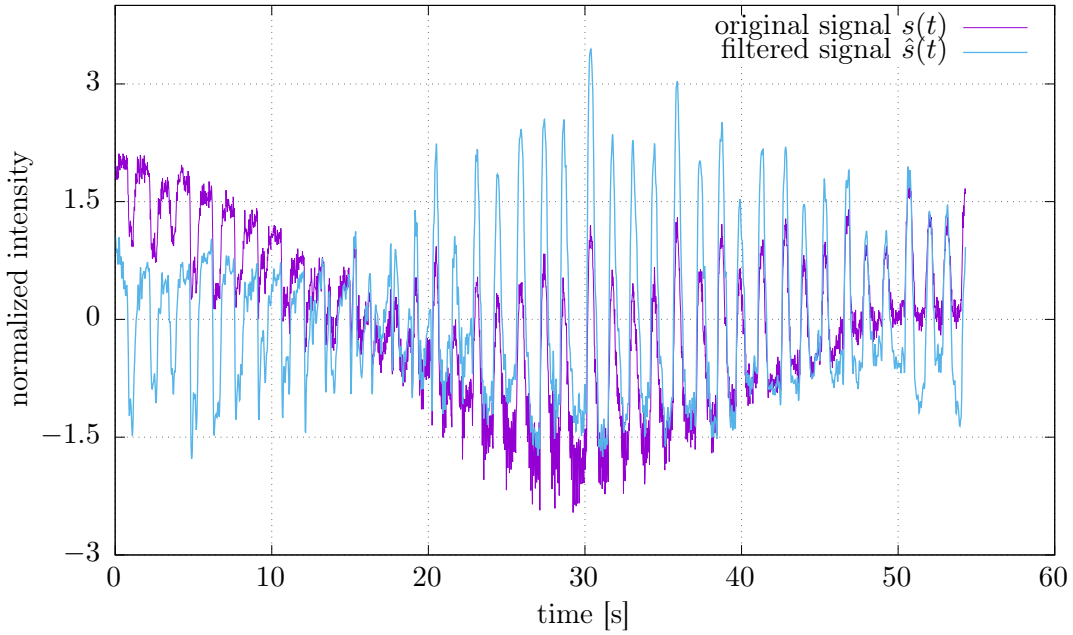

(c) Comparison of the filtered and unfiltered signal. During the band pass filtering frequencies considered low ($< 0.35\,\mathrm{Hz}$) and high ($> 9\,\mathrm{Hz}$) were removed.

Figure 3.10.: Beating signal of cell 1 resulting from the reference frame approach before and after it underwent band pass filtering. After the filtering the signal was normalised.

the low frequencies noise, caused by the rigid body cell movement, is removed by the band pass filtering. Furthermore, it can be insightful to notice what the spectra of the filtered and unfiltered beating signal (Figure 3.10a and Figure 3.10b) look like. All the interesting frequencies, meaning the frequency of the beating and the frequencies of the noise, are represented by sharp peaks. This is the same for all the other combination of cells and approaches. Thus, the different features of the generated signals can be very well distinguished in the frequency domain since they are all small band signals.

SVD filter After applying the band pass filter, the most prominent artefacts are removed, but some noise is still perceptible in the excited and rest states. To obtain a clearer signal, a last filter is applied to the data. This filter is based on a singular value decomposition (SVD) of the time delay embedding of the discrete input signal $s(t_i) = s_i$.

$$\boldsymbol{U}\,\boldsymbol{S}\,\boldsymbol{V}^T = \frac{1}{\sqrt{N}} \begin{pmatrix} s_1 & s_2 & \dots & s_d \\ s_2 & s_3 & \dots & s_{d+1} \\ \vdots & \vdots & \vdots & \vdots \\ s_{N-d+1} & s_{N-d+2} & \dots & s_N \end{pmatrix} \tag{3.10a}$$

$$\hat{s}(t_j) = U_1^j \quad \text{with} \quad j \in [1, N-d+1] \tag{3.10b}$$

The filtered signal $\hat{s}(t_i)$ is given by the first column of $\boldsymbol{U}$. Here, N is the number of samples the input signal $i \in [1, N]$, and d is the filter strength. Note that the input signal has to have a vanishing mean $\langle s(t_i) \rangle_i = 0$ and that the output signal is shorter than the input by $d-1$. In Figure 3.11 the effect of the SVD filter is shown. It can be seen how the noise in the excited and rest states is reduced while the overall form of the signal is preserved.

At this point, after applying all the mentioned filters, the signal is ready to be analysed and interpreted since many of the artefacts caused by the experimental measurement and the signal generation are drastically reduced. Yet, a last filter will be applied to produce a functional representation of the beating signal.

Fourier series filter The Fourier series filter converts the filtered beating signal $s(t)$ into a short Fourier series $f(t)$. This is achieved by only considering the dominant frequency $\tilde{\omega}$ in the spectrum of the beating signal and three higher harmonics. This means that the resulting Fourier series produces a very clean and periodic signal which is assumed to carry only the most relevant features of the cellular beating; like frequency and shape. Furthermore, the derivatives of the Fourier series are well defined. This makes it possible to easily approximate the periodic orbit of the beating in phase space. The

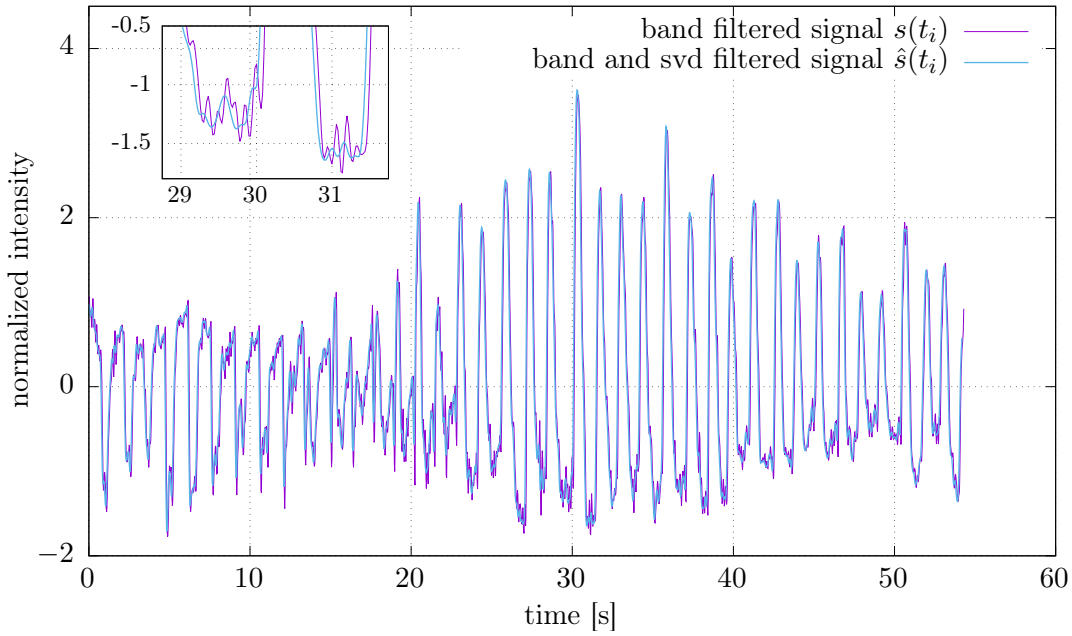

Figure 3.11.: Beating signal of cell 1 resulting from the reference frame approach before and after it underwent SVD filtering (Eq. (3.10)) with a filter strength of $d = 6$. After the filtering the signal was normalised.

Fourier series is given by the following equations.

$$f(t) = \sum_{k=1}^{N_f} a_k \cos(\omega_k t) + b_k \sin(\omega_k t) \tag{3.11a}$$

$$\omega_k = k\,\tilde{\omega} \quad \text{with} \quad \tilde{\omega} = \{\omega | \max_{\omega} |\mathscr{F}[s](\omega)|^2\} \tag{3.11b}$$

$$a_k = \frac{\mathrm{Re}\{\mathscr{F}[s](\omega_k)\}}{2\,N} \quad \text{and} \quad b_k = \frac{\mathrm{Im}\{\mathscr{F}[s](\omega_k)\}}{2\,N} \tag{3.11c}$$

Here, N is the number of samples of $s(t)$. The number of considered modes $N_f = 4$ is chosen to be constant for all analysed cells. The dominant frequency $\tilde{\omega}$ is given by the position of the maximum of the spectrum, and the Fourier coefficients are defined by the real and imaginary part of the Fourier transform of the signal. Considering a sampling rate of 50 Hz and a total frame number of about 2700 yields a frequency resolution of about $\Delta f = 0.02\,\mathrm{Hz}$ in Fourier space. Thus, the position of each harmonic is known up to a precision of $\Delta f = 0.02\,\mathrm{Hz}$. "Only" four modes are considered since the fourth mode mostly provides a negligible contribution[8] to the Fourier series. This is true for all analysed cells.

[8]Negligible contribution means $|\mathscr{F}[s](\omega_4)|^2 \ll |\mathscr{F}[s](\omega_1)|^2$.

Figure 3.12 shows the result of the Fourier series filter and compares the corresponding time series with the original signal (with removed outliers) and the SVD filtered signal. It can be seen how the peak and plateau behaviour is similar to those of the compared signals. Furthermore, the frequency of the Fourier time series matches very well with the temporal behaviour of the other two. Note that there exists a small offset between the Fourier time series and the original beating signal. Since the Fourier series is generated from the SVD filtered signal, it inherits its temporal properties, such as the temporal offset which is caused by the difference between the length of the SVD and the original signal (see Eq. (3.10)).

In total, four filters have been introduced which are applied successively to the generated beating signals. All of them are controlled with a set of specific parameters. Those filters are:

Outlier filter The outlier filter Eq. (3.7) removes clear outliers from the generated time series. Those are defined by eye.

Band pass filter Undesired frequencies are removed with the band pass filter Eq. (3.9). Undesired frequencies are frequencies which originate from artefacts caused by the measurement or from the signal generation approaches (e.g. noise or rigid body cell movement). The filter is controlled by the low cut off frequency f_{low} and by the high cut off frequency f_{high} (see Eq. (3.8)).

SVD filter After band pass filtering, the signal is further refined with the SVD filter Eq. (3.10). In general, this removes noise from the excited and rest states of the beating signal. The filter is controlled by the filter strength d.

Fourier filter In the last filtering step, all but four harmonics are removed from the signal's spectrum. This yields an analytic Fourier series representation with well defined derivatives. Those can be used to assign a periodic orbit to the beating signal. The Fourier filter is controlled by the number of harmonics to keep, which is equal four for all cells and signals.

3.3. Results

In this study, six cells were analysed. Three beating signals were generated per cell by applying the introduced approaches (Sec. 3.2.1). This yields 18 beating signals in total. The different approaches have been developed to account for the different characteristics of the cell video data, like background noise or rigid body cell movement. Each beating signal was filtered with the mentioned filter chain (Sec. 3.2.2) after generation. Only one (the best) signal per cell was chosen as a representative result. This choice was made by observing certain features of the signals, like noise or pronounced peak shapes and by comparing them to the video data, in terms of frequency and observed beating behaviour. See Figure A.2 in the appendix for an illustration of a poor and a good signal. Table 3.2 states which signal generation approach was chosen for which cell and which

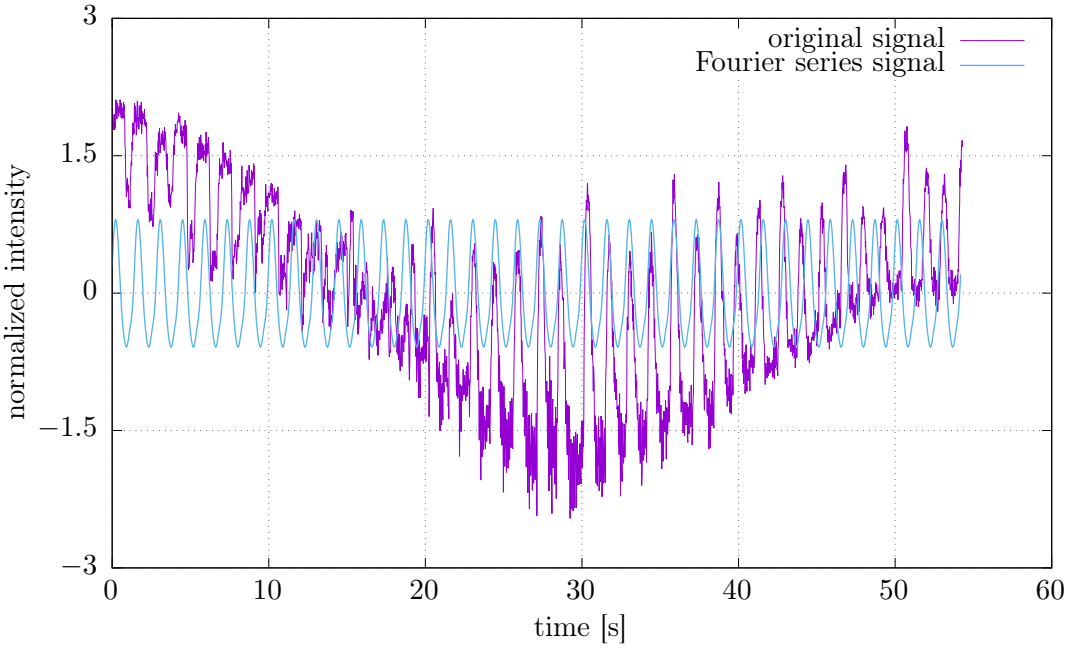

(a) Comparison of the Fourier time series with the raw signal (without outliers) of cell 1 generated with the reference image approach.

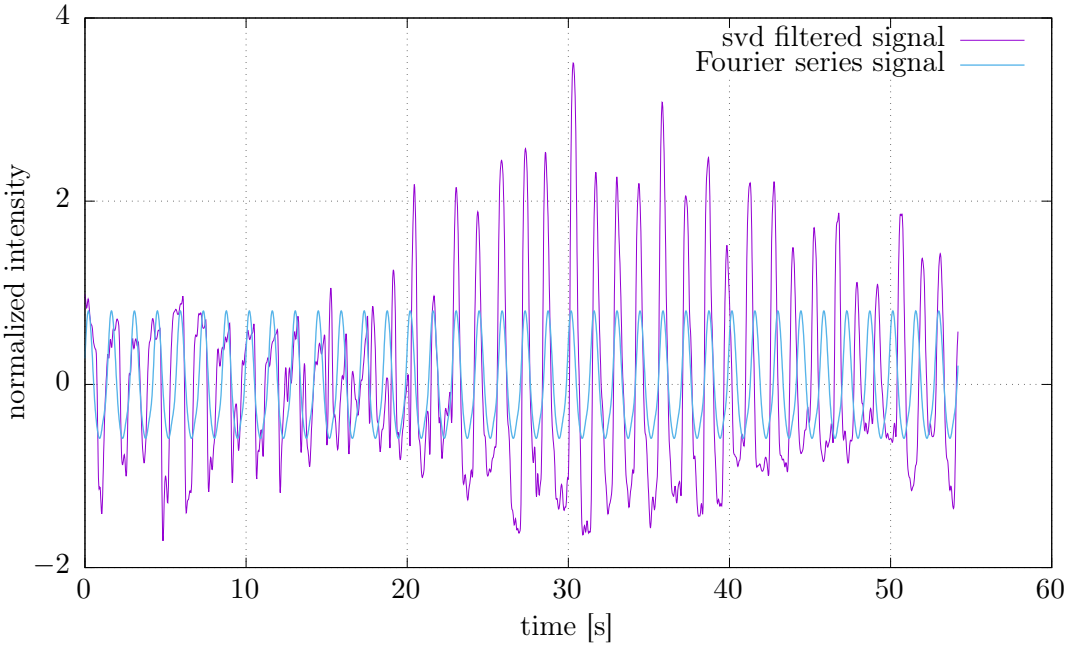

(b) Comparison of the Fourier time series with the SVD filtered signal.

Figure 3.12.: Time series of a Fourier series representing the beating signal of cell 1. The Fourier series was constructed from the dominant frequency and four harmonics of the SVD filtered signal (Figure 3.11). The frequency resolution is $\Delta f = 0.02\,\mathrm{Hz}$.

Cell	Approach	f_{low} [Hz]	d	f Eye [Hz]	f Appr. [Hz]	Figure
1	active contour	0.35	6	0.72 (±0.02)	0.72 (±0.02)	Figure A.1a
2	reference frame	0.26	6	0.51 (±0.02)	0.52 (±0.02)	Figure A.1b
3	active contour	0.20	16	0.39 (±0.02)	0.39 (±0.02)	Figure A.1c
4	active contour	0.70	6	1.40 (±0.02)	1.44 (±0.02)	Figure A.1d
5	reference frame	0.32	10	0.64 (±0.03)	0.61 (±0.02)	Figure A.1e
6	reference frame	0.35	20	0.70 (±0.02)	0.70 (±0.02)	Figure A.1f

Table 3.2.: For each cell the following information is shown: the approach which was chosen to analyse the beating of the cell (see Sec. 3.2.1), the lower cut off frequency of the band pass filter Eq. (3.9), the filter strength of the SVD filter Eq. (3.10), the beating frequency determined by watching the corresponding video and counting the beat events, the beating frequency determined by the dominant frequency of the SVD filtered signal, and a reference to the figure showing the cell. The error of the dominant frequency is given by the frequency resolution in Fourier space. The average frequency (with respect to the human eye approach) the cardiomyocytes feature is: $\langle f \rangle = 0.73\,(\pm 0.03)\,\text{Hz}$.

filter parameters have been used. Furthermore, it compares the beating frequencies calculated by watching the videos with the beating frequencies which resulted from the chosen approach.

The first result obtained is the temporal shape of the cell beating. This can be seen in Figure 3.13 for cell one. The SVD filtered signal and the corresponding Fourier time series are shown. Two phases can be distinguished.

Peak phase A fast change in amplitude before the local maximum (if the peaks point upwards) of the signal is reached.

Recover phase After the peak was reached the signal approaches its local minium with a steep slope as well, but close to the minimum the slope becomes less steep.

The observed shape of the beating signals compare very well to those shown in the past and recent literature [7, 8, 58, 9, 10]. But since the recent research focused solely on the determination of certain quantitative aspects of myocardial beating, like frequency and generated forces, no one ever discussed, at least to my knowledge, the mentioned qualitative features.

One might be obliged by intuition to call the peak *excited state* and the plateau-like recovery *rest state*. But this would mean that the cell **elongates** when it is excited, since its length, along the direction determined by principal component analysis of the active contour approach, increases. But muscle cells are known to **contract** when excited. One could argue that this behaviour might be due to a projection issue. Although a cardiomyocyte is a three dimensional object, only two dimensional video data were analysed. But all the analysed cells, except cell 3[9], are showing this *peak up behaviour*.

[9] Cell 3 shows *peak down behaviour*.

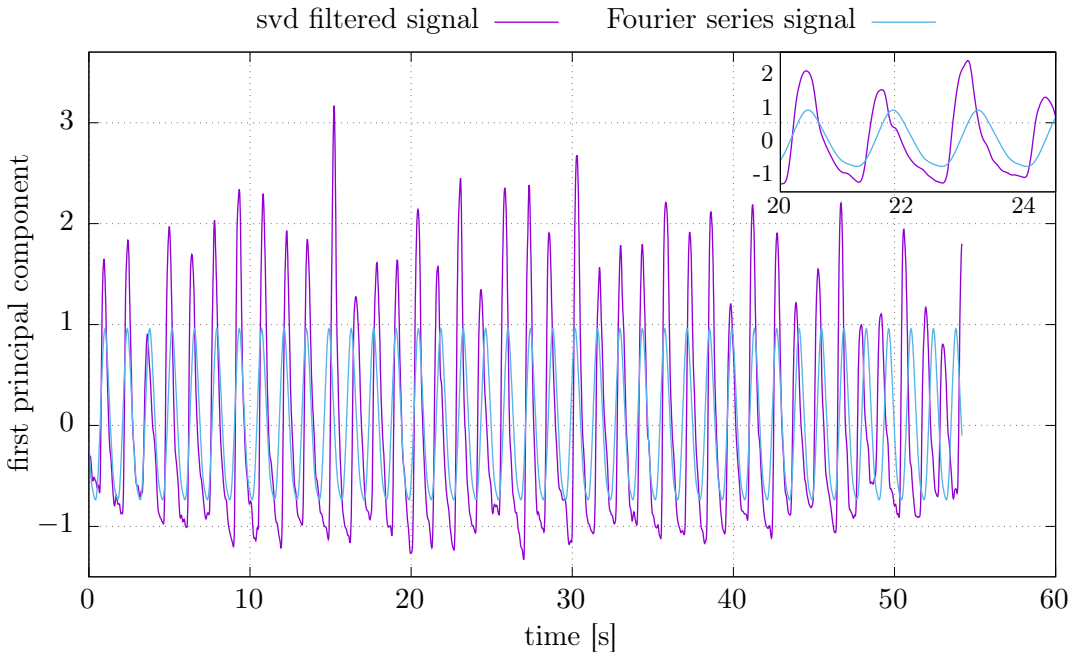

Figure 3.13.: Beating signal of cell 1 generated with the active contour approach. Shown is the SVD filtered signal and the signal generated with the corresponding Fourier series.

Furthermore, as the cells mature, they position their "active direction" parallel to the observed focal plane, as can be seen exemplary in Figure 3.2e. These two kinds of beating, namely the peak up and the peak down behaviour, were observed by Radmacher[10] et al. [7] as well, but (to my knowledge) were never discussed afterwards again. Radmacher et al. observed peak up and peak down behaviour during the analysis of myocardial clusters with the AFM. They tried to find the same behaviour with single cardiomyocytes, but did not succeed due to limitation of their measurement method. The results presented in this thesis suggest that even single cardiomyocytes show both peak up and peak down behaviour. One interpretation is rather astonishing, because peak up behaviour corresponds to an elongation of the cell. Since muscle cells are known to contract if excited, the following interpretation sounds more realistic. The observed behaviour is a mere geometrical effect caused by both, the arrangement of the myofilaments of the cells and the recorded focal plane. The direction of contraction of a cardiomyocyte is determined by their myofilaments. If those fibres are not aligned property, as it might be the case in a premature cardiomyocyte, the cell does not contract along one distinct direction but buckles. Additionally, only two spatial dimensions were observed during the experiments. Thus, the peak up behaviour might be a projection artefact caused by buckling cells.

[10] In their study, the peak up and peak down behaviour is swapped compared to the definition given in this thesis. This results from their AFM measuring method.

Note that only the active contour approach can be used to measure a concept like elongation or contraction since it measures the length of the cell along the direction given by the first principal component of the cell's shape. The other two approaches measure the mean intensity of a video frame which is rather related to the cross section area of a cell. Thus the active contour approach was used to determine if a cell shows peak up or peak down behaviour even if another approach was chosen to represent the cell's beating signal. Furthermore, the resulting behaviour was confirmed by watching the video data.

The beating signals of all cells are shown in the appendix Figure A.3 - A.8. Cell one, two, four, five, and six show peak up behaviour. Only cell three shows peak down behaviour. Compered to the other cells, cell three looks rather extraordinary (Figure A.1). Nevertheless, all the cells exhibit the two phases mentioned: the *peak phase* and the *recover phase*. Note that this was already observed by watching the video data (see the human eye approach in Sec. 3.2.1).

By facilitating the active contour approach, it is possible to estimate the maximum amount of strain a cell exhibits on average while it beats. Strain is the relative elongation of an object with respect to a fixed configuration state. Only the strain of cells whose beating signals are represented by the active contour approach has been estimated. These are cell one, three, and four. For estimating the maximum strain ε_0 of a cell, the extrema of it's **non-normalised** svd filtered beating signal $s(t)$ are determined and the averages of it's local maximal $s_{\max,i}$ and minimal $s_{\min,i}$ values are calculated.

$$\langle s_{\max} \rangle = \frac{1}{N_{\max}} \sum_{i}^{N_{\max}} s_{\max,i} \tag{3.12a}$$

$$\langle s_{\min} \rangle = \frac{1}{N_{\min}} \sum_{i}^{N_{\min}} s_{\min,i} \tag{3.12b}$$

$N_{\max}$ and $N_{\min}$ are the total numbers of the local maxima and minima, respectively. The error of those mean extremal values are considered to be the corresponding empirical standard deviation called $\sigma_{\max}$ and $\sigma_{\min}$, respectively. Figure 3.14 show exemplary the local maximal and minimal values of the svd filtered signal of cell 1. The maximum strain a cell under study exhibits on average is given by:

$$\varepsilon_0 = \frac{\langle s_{\max} \rangle - \langle s_{\min} \rangle}{\langle s \rangle}. \tag{3.13}$$

Here $\langle s \rangle$ is the temporal mean of the cell's beating signal. The error of the calculated maximum strain σ_{ε_0} is given by the sum of the empirical standard deviations of the mean extrema. This is the worst case error.

$$\sigma_{\varepsilon_0} = \frac{\sigma_{\max} + \sigma_{\min}}{\langle s \rangle} \tag{3.14}$$

In Table 3.3 the calculated maximal strains are shown for cell one, three and four. On

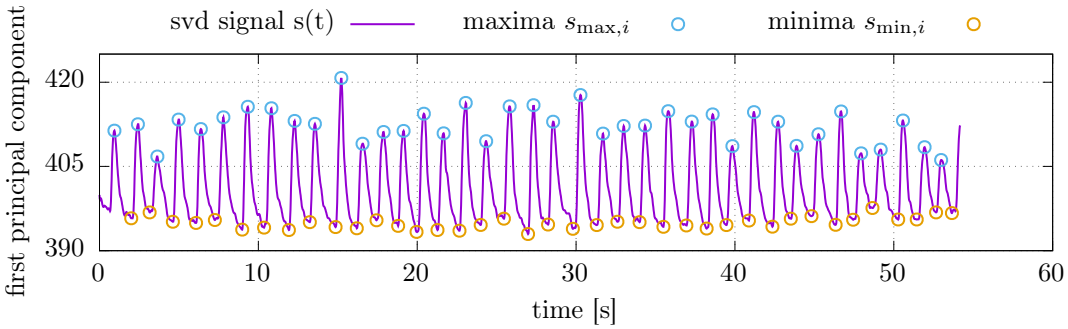

Figure 3.14.: Svd filtered beating series of cell 1 showing the local minima and maxima which are used for calculating the maximal strain the cell exhibits on average.

Cell	average strain
1	4 (±1) %
3	2.7 (±0.6) %
4	8 (±2) %
mean	5 (±2) %

Table 3.3.: Maximal strains the cells analysed with the active contour approach exhibit on average and its mean value.

average (over three cells) the premature cardiomyocytes under study exhibit a maximal strain of about 5 (±2) %. The error of the mean strain over all three cells, represents again the worst case scenario.

Additional observations can be made by considering the beating signals in the frequency domain. Figure 3.15 shows the frequency spectrum of cell 1 obtained by Fourier transforming its SVD filtered signal. The spectra of all cells can be found in the appendix Figure A.9 - A.14. The frequency spectra show that the beating events of the cells occur periodically with a very stable frequency. This is true for the measured time window of about one minute[11]. This is indicated by the very sharp peaks (harmonics) in the spectra. Thus the beating of the premature cardiomyocytes analysed is a small band signal. The frequencies given in Figure 3.2 were determined by locating the positions of the first harmonic in the corresponding spectra.

Since the beating signals are small band signals, it is self-evident to approximate them with a linear combination of sines and cosines or rather a Fourier series. These Fourier series need to comprise only few terms since the spectra of the beating signals contain rather few pronounced harmonics. As discussed in Sec. 3.2.2, the Fourier series are generated by considering only the first four harmonics. Approximating a measured beating signal with a Fourier series has the advantage that the signal is described as a

[11] Other studies found that the beating behaviour of cardiomyocytes is rather unstable, but these instabilities can only be seen in measurements several minutes long [7].

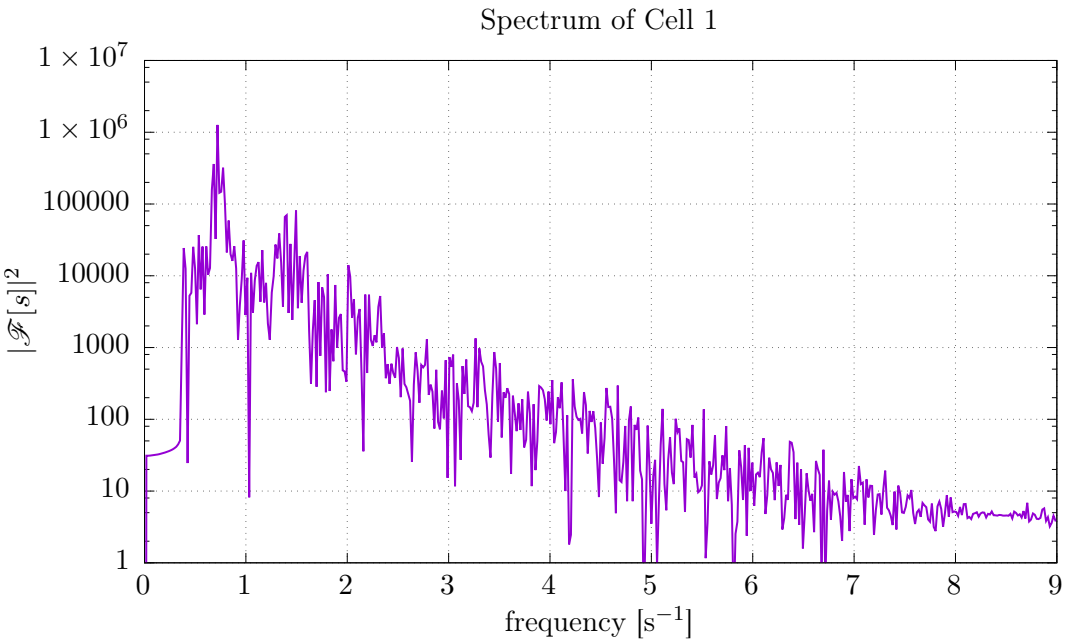

Figure 3.15.: Frequency spectrum of the SVD filtered signal of cell 1, generated with the active contour approach.

smooth and continuous function in time, rather then as a set of discrete values which still suffer from noise and alike. Thus, all derivatives of the approximated signals are known. For analysing the periodic motion of an oscillator, it is common practice to consider its limit cycle in phase space. In a two dimensional system, the phase space is spanned by the dynamic variable which oscillates and its first derivative. Considering the beating signals and their approximation as Fourier series, one can easily access both. Figure 3.16 shows the orbits, corresponding to the periodic beating of the analysed cells. To emphasise their similarity, the orbit corresponding to cell three was turned[12] by π. The first thing one might notice is the difference in magnitude of the amplitude (10^{-1}) and its derivative (10^0). This is caused by the peak behaviour of the beating signals. Furthermore, the orbits look like ellipses for a wide range of amplitudes, but buckle at their leftmost extent. This bifid shape emphasises the two phases of one beating event mentioned before: the peak phase and the recover phase. The buckling corresponds to the recover phase.

3.4. Summary

To qualitatively access the beating behaviour of premature cardiomyocytes, experiments were conducted by my collaborator Susanne Schlick. In collagen gel embedded cardiomy-

[12] All cells exhibit peak up behaviour, except cell three which exhibit peak down behaviour.

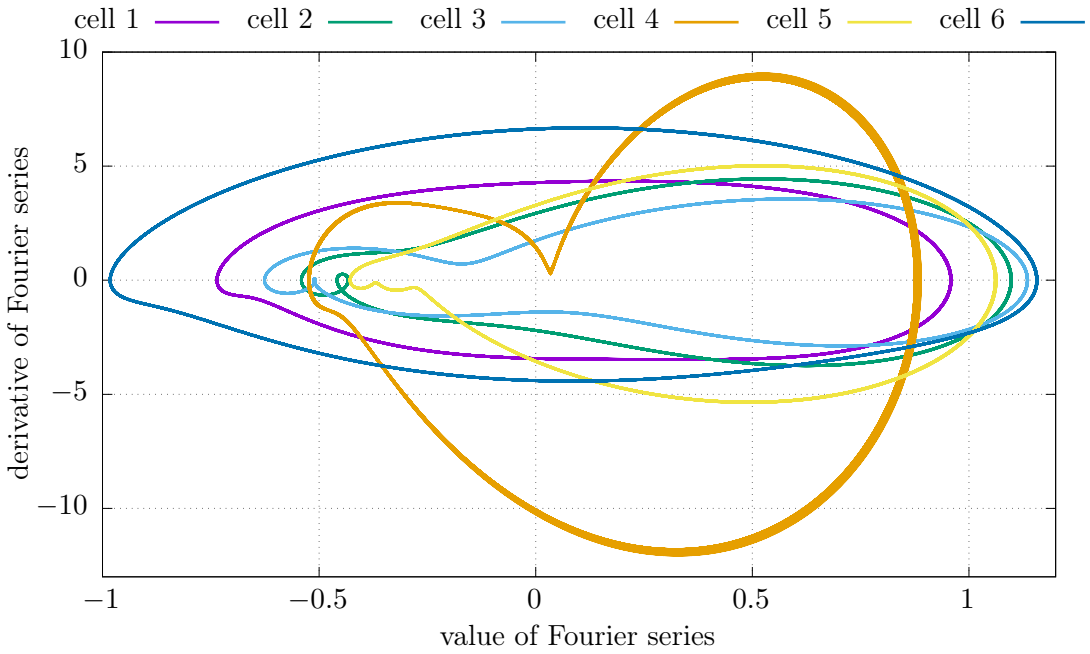

Figure 3.16.: Periodic orbits in phase space, generated with the corresponding Fourier series, showing the form the beating signal of the analysed cells.

ocytes were recorded with a camera attached to an optical microscope. The resulting video data were analysed with the four discussed approaches, yielding time series, showing the beating of premature cardiomyocytes. These time series were filtered with the introduced filter chain to remove certain artefacts caused by the measurements and the time series generation approaches. The main result of this analysis is the temporal from the beating behaviour of premature cardiomyocytes. Namely the two phases of a beat event: the peak phase and the recover phase. Furthermore, periodic orbits in phase space were constructed from the measured signals, which show the qualitative characteristic beating behaviour of premature cardiomyocytes in phase space.

4. Rheology of the Extracellular Matrix

Premature cardiomyocytes are able to synchronise their self-sustained beating behaviour. This synchronisation can be caused by a purely mechanical coupling mediated by the extracellular matrix [13]. It is manifest that the mechanical properties of the extracellular matrix are influencing this synchronisation behaviour. For gaining experimental insights into the viscoelastic properties of the extracellular matrix, dynamic shear rheometry experiments have been conducted. The experiments have been carried out by Susanne Schlick[1], Florian Spreckelsen[2], Florian Rehfeldt[3], and myself.

4.1. Experimental setup

During the dynamic shear rheometry experiments, samples of hydrogels, comprising collagen I, were placed in a shear rheometer. The used shear rheometer consists of a static and a rotating plate. By rotating the latter one, the sample confined by those plates is sheared. See Figure 4.1 for an abstract sketch of a shear rheometer. Two observables can be measured in this way: the strain ε, which is the normalised (with the sample height $h(r)$) displacement l of a point on a cycle (with radius r) if rotated by the angle φ, and the stress σ, which is the force F per area[4] A of the sample.

$$\varepsilon = \frac{l}{h(r)} = \frac{\varphi\, r}{h(r)} \tag{4.1a}$$

$$\sigma = \frac{F}{A} = \frac{F}{\pi\, r^2} \tag{4.1b}$$

Note that the rotating plate has the shape of a cone (Figure 4.1). This shape ensures that the measured strain and stress are equal over the whole radius of the plate. In the experiments, the height of the medium was around $h(r_0) \approx 100\,\mu$m. The radius r_0 was on the length scale of one cm.

The sample is stimulated by either a specific strain or stress signal and the corresponding stress or strain response is measured to analyse the rheological properties of the medium under study. During the conducted experiments, a strain stimulus $\varepsilon(t)$ was provided and the stress response $\sigma(t)$ of the sample was measured. Note that if the strain stimulus is a periodic function, the stress response will be periodic (with the same

[1] Institute of Pharmacology and Toxicology, University Medical Center Göttingen
[2] Biomedical Physics Group, Max Planck Institute for Dynamics and Self-Organization, Göttingen
[3] Third Institute of Physics - Biophysics, Georg-August-University Göttingen
[4] The area perpendicular to the axis of rotation.

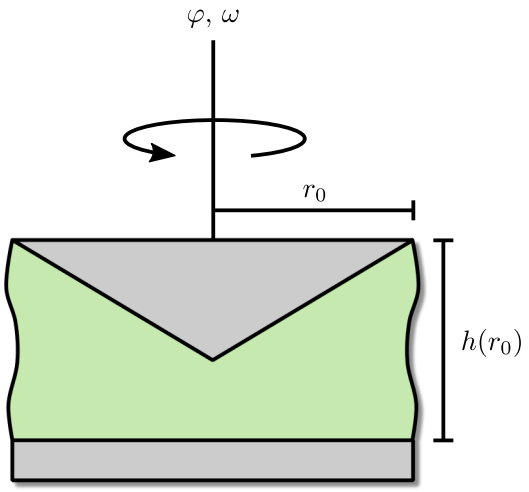

Figure 4.1.: Abstract sketch of a shear rheometer. The upper cone shaped plate rotates about the angle φ with the angular velocity ω and thus shears the sample (green). The radius dependent sample height $h(r)$ ensures that the measured strain and stress are independent of the radius r.

period T) after the transients behaviour has ceased.

$$\sigma(t) \equiv f(\varepsilon(t)) \tag{4.2a}$$

$$\sigma(t) = \sigma(t+T) \quad \text{if} \quad \varepsilon(t) = \varepsilon(t+T) \tag{4.2b}$$

The strain stimulus was chosen to be a sine function in all experiments.

$$\varepsilon(t) \equiv \varepsilon_0 \sin(\omega\, t) = \varepsilon_0 \sin(2\pi\, f\, t) \tag{4.3}$$

Thus, the strain stimulus and the corresponding stress response depend on the maximum strain or strain amplitude ε_0, and on the shear frequency f or angular velocity ω. In general, the stress response can be any nonlinear periodic function in time which depends on the mentioned parameters. If, however, the medium exhibits only linear responses, which are governed by linear phenomenological rheology (see Sec. 2.3), the stress responses will be sinusoidal function as well. The property which connects the stimulus and the response in this case is the complex modulus $G^*(\omega)$ or rather its real and imaginary part: the storage $G'(\omega)$ and the loss modulus $G''(\omega)$, respectively.

$$\sigma(t) = G'(\omega)\, \varepsilon + \frac{G''(\omega)}{\omega}\, \dot{\varepsilon} \tag{4.4a}$$

$$\sigma(t) = \sigma_0 \sin(\omega\, t + \delta) = G'(\omega)\, \varepsilon_0 \sin(\omega\, t) + G''(\omega)\, \varepsilon_0 \cos(\omega\, t) \tag{4.4b}$$

Note that Eq. (4.4b) only holds in the case of a sine stimulus (Eq. (4.3)). From Eq. (4.4a) it becomes evident that the phase lag δ between the strain stimulus and the stress response is caused by a non vanishing loss modulus $G''(\omega)$. By facilitating this phase

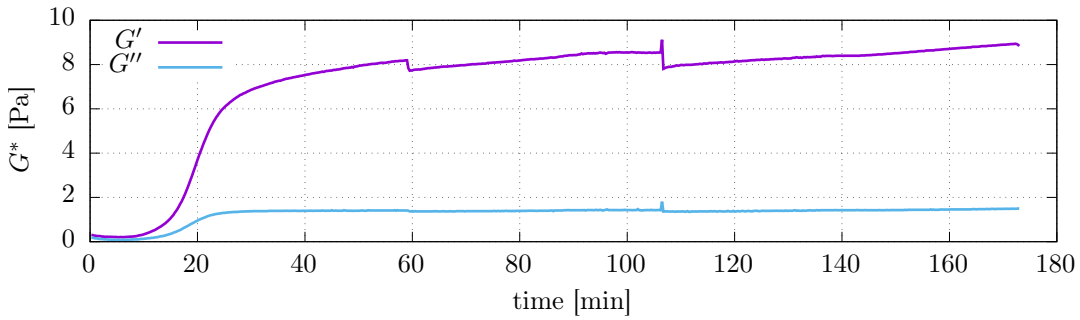

Figure 4.2.: Complex modulus of collagen over time. The strain amplitude is $\varepsilon_0 = 1\,\%$ and the shear frequency is $f = 1\,\mathrm{Hz}$.

lag, the loss and storage moduli can be determined by knowing the strain stimulus and the stress response. Note that a system which responds with a force (or stress) that is in phase with the corresponding elongation (or strain) conserves the deformation energy. Thus, the storage modulus $G'(\omega)$ is proportional to the average energy conserved during one cycle of oscillation and the loss modulus, which causes the phase lag between stress response and strain stimulus, is proportional to the average energy dissipated during one cycle of oscillation. Thus, the storage modulus can be considered as a measure of the elasticity or stiffness of a medium under study and the loss modulus can be considered as a measure of its viscous behaviour.

As soon as media with nonlinear viscoelastic responses are considered, the notions of the storage and loss modulus become meaningless since they are linear properties. In this cases only the direct strain stimulus compared with the corresponding stress response are measured in LAOS-experiments[5] [24]. Note that for every medium which behaves nonlinear, there is a regime of sufficient small maximum strains ε_0 in which it can be considered linear.

4.2. Data analysis

As already mentioned, a hydrogel comprising collagen I was analysed with a shear rheometer by applying a sine strain stimulus (Eq. (4.3)). The storage $G'(\omega)$ and the loss modulus $G''(\omega)$ of the medium have been measured over around three hours[6] at a constant maximum strain of $\varepsilon_0 = 1\,\%$ and a constant shear frequency of $f = 1\,\mathrm{Hz}$. In Figure 4.2, the measured results are shown. It can be seen that during the first 30 min, the medium under study becomes stiffer and a little bit more viscous. This behaviour is caused by the collagen which polymerises in the sample. After this initial polymerisation phase, the medium does not change its viscoelastic properties much more. Note that there are two jumps in the data; one at around 60 min and the other at around 105 min. These jumps are caused by mechanical perturbations of the table the rheometer resides

[5] LAOS is the acronym for **l**arge **a**mplitude **o**scillation **s**hear.
[6] This kind of measurement is called *time sweep*.

on. After the viscoelastic properties of the medium did not change anymore, thus after the time sweep, LAOS-experiments have been conducted since polymer gels are known to exhibit nonlinear viscoelastic behaviour[7] [24, 26].

In these LAOS-experiments the stress response $\sigma(t)$ of a sinusoidal strain stimulus $\varepsilon(t)$ (Eq. (4.3)) was measured for different maximum strains ε_0 and a constant shear frequency $f = 1\,\mathrm{Hz}$. Figure 4.3a and Figure 4.3b show the stress response (blue) to a strain stimulus (purple) for two different maximum strains of 3.16 % and 7.91 %, respectively. The corresponding stress response spectra are shown in Figure 4.3c and Figure 4.3d. It can be seen that the medium under study behaves rather linear[8] at a maximum strain of about $\varepsilon_0 = 3.16\,\%$. This is evident, since the corresponding spectrum comprises only one peak at the shear frequency of $f = 1\,\mathrm{Hz}$. Thus, the stress response is a sinusoidal function, just like the strain stimulus. At a maximum strain of about $\varepsilon_0 = 7.91\,\%$ the stress response does not behave linearly anymore. This is indicated by the additional harmonics in the corresponding Fourier spectrum. Since the stress response and the strain stimulus are periodic functions in time, they can be represented by a short Fourier series $F(t)$ as the few non-negligible harmonics indicate.

$$F(t) = \sum_{k=1}^{N} a_k \, \sin(\omega_k \, t) + b_k \, \cos(\omega_k \, t) \tag{4.5}$$

These Fourier series can be considered as noise free stimulus and response functions. In Figure 4.3e and Figure 4.3f the raw data and the Fourier fit of the corresponding stress responses are compared. It can be seen that the Fourier series represent very well the raw data. In Figure 4.3g and Figure 4.3h the Fourier series of the stress response (blue) to the strain stimulus (purple), at the two different maximum strains, are shown. The phase lag between the response and the stimulus is relatively small. Thus, only little amounts of energy are dissipated during one cycle of oscillation and thus the medium behaves rather elastic. In case of a linear response (at $\varepsilon_0 \leq 3.16\,\%$), this was predicted by the small (compared to the storage moduli) loss moduli which were measured during the time sweep measurements (Figure 4.2). In Figure 4.3h it can be seen how a nonlinear periodic stress response might look like. The shown nonlinear behaviour is called *strain stiffening*.

Another way of presenting the LAOS-data is in form of *Lissajous figures*. In Lissajous figures the stress response $\sigma(t)$ is plotted over the strain stimulus $\varepsilon(t)$. This yields closed (in case of periodic response and stimulus functions) curves $\sigma(\varepsilon)$ parametrised by time t. Figure 4.4 shows three Lissajous figures which correspond to three different maximum strains 3.16 %, 5.01, and 7.91 %, respectively. The Fourier series representations of the stress response and the strain stimulus are plotted in Figure 4.4. The corresponding Lissajous figures which comprise the raw data can be found in the appendix (Figure A.17). A linear stress-strain relation is indicated by an ellipsoid curve. As the nonlinear re-

[7] The collagen gel under study can be considered linear at maximum strains of around $\varepsilon_0 = 1\,\%$ as it can be seen later.

[8] This result validates the former assumption that the medium under study behaves linear at $\varepsilon_0 = 1\,\%$. Thus the complex modulus is a meaningful observable in this low amplitude regime.

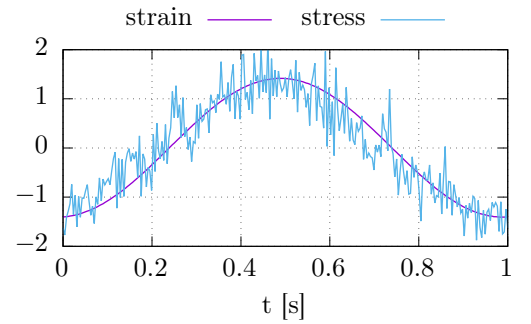

(a) Raw data at $\varepsilon_0 = 3.16\,\%$

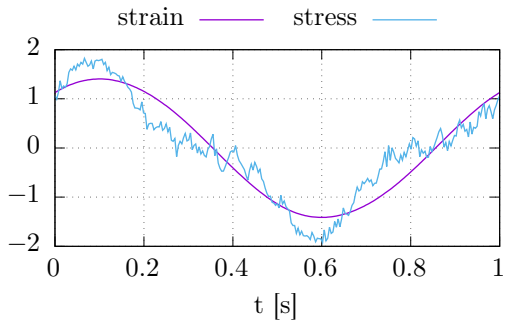

(b) Raw data at $\varepsilon_0 = 7.91\,\%$

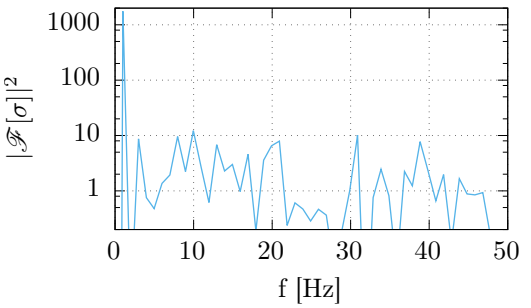

(c) Stress response spectrum at $\varepsilon_0 = 3.16\,\%$

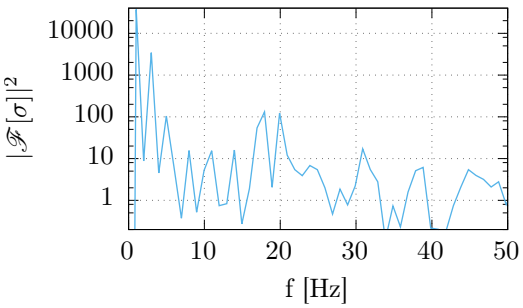

(d) Stress response spectrum at $\varepsilon_0 = 7.91\,\%$

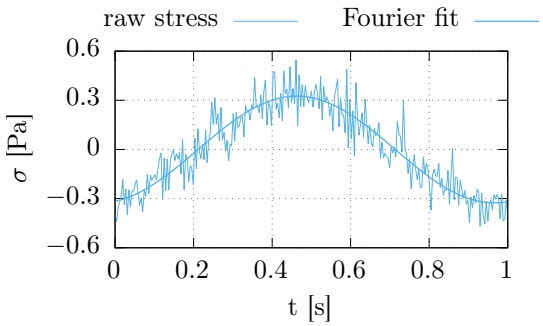

(e) Stress Fourier fit at $\varepsilon_0 = 3.16\,\%$

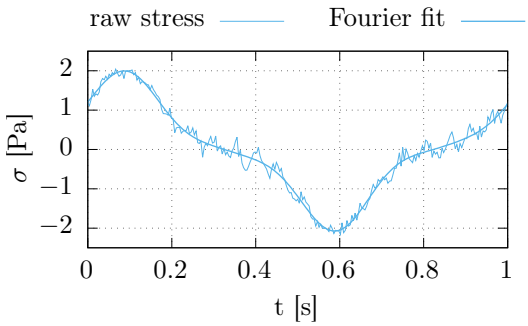

(f) Stress Fourier fit at $\varepsilon_0 = 7.91\,\%$

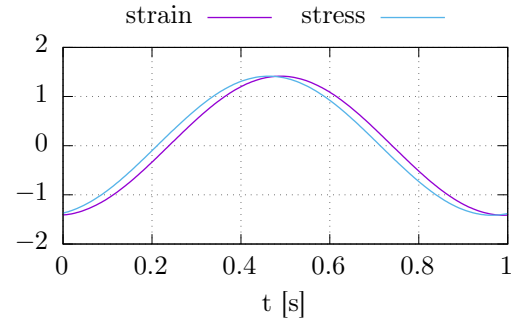

(g) Fourier fit at $\varepsilon_0 = 3.16\,\%$

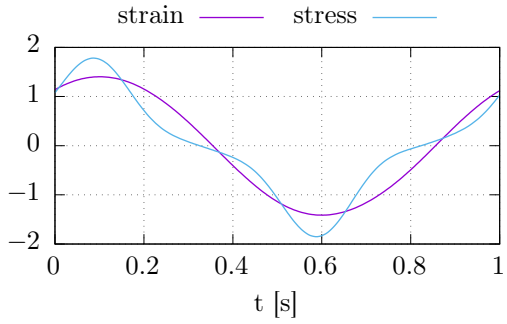

(h) Fourier fit at $\varepsilon_0 = 7.91\,\%$

Figure 4.3.: (a), (b) (g), (h) Strain stimulus $\varepsilon(t)$ and stress response $\sigma(t)$ at two different maximum strains ε_0 (left and right column). If compared directly, both signals are normalised to standard deviation one. (c), (d) The small band spectra of the stress response suggest (e), (f) a fit with a Fourier series. The shear frequency is $f = 1\,\mathrm{Hz}$.

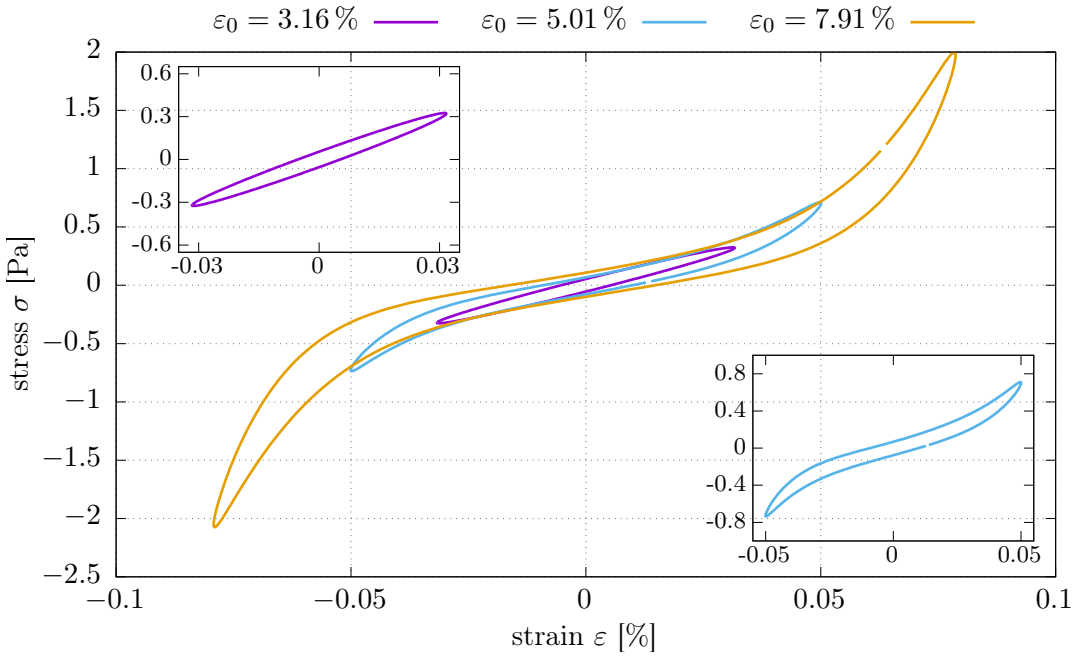

Figure 4.4.: Lissajous figures at different maximum strains ε_0 showing a linear stress response at lower maximum strain $\varepsilon_0 = 3.16\,\%$ and strain stiffening at higher maximum strain $\varepsilon_0 = 7.91\,\%$. The Lissajous figures are based on a Fourier fit. The Lissajous figures which comprise the raw experimental data are shown in Figure A.17. The shear frequency is $f = 1\,\mathrm{Hz}$.

sponse of a viscoelastic medium becomes more pronounced, the corresponding Lissajous curve deviates more from an elliptical shape. The phase lag between response and stimulus and thus the dissipated energy during one cycle of oscillation, is indicated by the width of the ellipsoid or rather the closed curve. Perfect elasticity corresponds to a curve which is a single line[9] and hysteresis corresponds to energy dissipation and thus viscous behaviour. As expected from the small phase lag between stimulus and response, the Lissajous curves shown in Figure 4.4 are rather narrow. The linear behaviour of the collagen gel at a maximum strain of $\varepsilon_0 = 3.16\,\%$ is represented by an elliptical curve[10] (blue). It has been shown already that the medium shows a nonlinear response at a maximum strain of $\varepsilon_0 = 7.91\,\%$. The corresponding Lissajous curve (orange) illustrates the mentioned strain stiffening behaviour very well. Strain stiffening means that the medium reacts with nonlinear increasing stress if it is elongated over a certain amount. It can be seen that the onset of the strain stiffening is around a strain of $\varepsilon \approx 4(\pm 1)\,\%$.

[9] A line like curve can still be closed, since the system under study travels on top of it back and forth during one cycle of oscillation.

[10] Since a Fourier series (Eq. (4.5)) with $N = 1$ has been used to fit this data, the Lissajous curve is an ellipsoid by construction. But it was already validated that the system behaves linear at maximum strains of $\varepsilon_0 \leq 3.16\,\%$.

As shown in Chap. 3, the premature cardiomyocytes under study exhibit a maximum strain of about $\varepsilon_0 = 5(\pm 2)\,\%$ on average. Thus the analysed range of maximum strains $\varepsilon_0 \in \{3.16\,\%, 5.01\,\%, 7.91\,\%\}$ will be of great avail for modelling and disusing the corresponding stress responses – at least in theory. There are some limitation to the applicability of the presented results. The first point to consider is a theoretical one. The dynamic shear measurements have been conducted by using a sinusoidal strain stimulus (Eq. (4.3)). This kind of stimuli comprise only one temporal frequency, and it was chosen to be constant at $f = 1\,\mathrm{Hz}$. Although cardiomyocytes beat on a well defined time scale of the magnitude of about 1 Hz, their beating signal is not a pure sinusoidal function of time, thus it comprises multiple time scales (see Figure 3.13 and Figure 3.15). It is not known a priori how a nonlinear medium will respond to a strain signal which comprises multiple time scales, if only the responses to signals comprising one time scale are known.

The second limitation are the experimental data themselves. During the experiments multiple sets of data have been acquired. Although all of them show the same qualitative behaviour, they differ quite noticeable in a quantitative sense with respect to different observables. These are the temporal end of the polymerisation phase and the height of the following plateau, if the time sweeps are considered (see Figure 4.2). Furthermore some LAOS-measurements have been conducted at the very edge of the measurement precision of the shear rheometer used, as it is indicated by the sometimes low signal to noise ratio (Figure 4.3a). Furthermore it is to note that the used collagen gels seem to be less stiff by at least one order of magnitude compared to those analysed by others [18, 59]. This could be related to differences regarding the preparation of the gels used, in particular the concentration of collagen.

Nevertheless, the acquired results are a good starting point for understanding and modelling qualitatively (and to some extent quantitatively) the viscoelastic properties of the extracellular matrix which couples the premature cardiomyocytes and aids their synchronisation.

4.3. Maxwell fluid approximation

For modelling and further understanding the viscoelastic response of the extracellular matrix, a linear approach is used. The coupling provided by the extracellular matrix shall be modelled with the Maxwell fluid. The Maxwell fluid was already introduced in Sec. 2.3. It is show in Figure 2.5a and again in Figure 4.5 for convince. The constitutive equations describing the viscoelastic behaviour of the Maxwell fluid are given in Eq. (2.9) and in Eq. (4.6) again.

$$\dot{\sigma} = E\,\dot{\varepsilon} - \frac{E}{\eta}\,\sigma \tag{4.6}$$

Since the Maxwell fluid is a linear viscoelastic model, its behaviour can be perfectly described in terms of the complex modulus $G^*(\omega)$. The real and imaginary part (the storage and the loss modulus, respectively) of the complex modulus of the Maxwell fluid

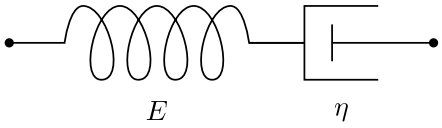

Figure 4.5.: Sketch of the Maxwell fluid. E denotes the elastic modulus of the linear spring and η denotes the viscosity of the dashpot.

are already known (Eq. (2.13)) to be:

$$G^*(\omega) = G'(\omega) + i\,G''(\omega) \tag{4.7a}$$

$$G'(\omega) = E\left(1 - \frac{E^2/\eta^2}{E^2/\eta^2 + \omega^2}\right) \tag{4.7b}$$

$$G''(\omega) = E\,\omega\,\frac{E/\eta}{E^2/\eta^2 + \omega^2}. \tag{4.7c}$$

Note that ω is the angular frequency of the provided stimulus, which is always the strain in the context of this thesis. In the following, the parameters which govern the viscoelastic behaviour of the Maxwell fluid shall determined from the acquired experimental data.

First, the elastic modulus E and the viscosity η of the final state (after the polymerisation phase (Figure 4.2)) of the extracellular matrix shall be determined. For that purpose Eq. (4.4a) (which describes the stress responses to a strain stimulus of a linear viscoelastic medium) is used together with the known storage (Eq. (4.7b)) and loss modulus (Eq. (4.7c)) of the maxwell model. This yields the following equation which describes the stress response $\sigma(t)$ of the Maxwell fluid in dependence on the strain stimulus $\varepsilon(t)$ and the corresponding strain rate $\dot{\varepsilon}(t)$:

$$\sigma(t) = E\left(1 - \frac{E^2/\eta^2}{E^2/\eta^2 + \omega^2}\right)\cdot\varepsilon(t) + E\,\frac{E/\eta}{E^2/\eta^2 + \omega^2}\cdot\dot{\varepsilon}(t). \tag{4.8}$$

If all temporal functions ($\sigma(t)$, $\varepsilon(t)$, and $\dot{\varepsilon}(t)$) and the angular frequency of the strain stimulus ω are known, Eq. (4.8) can be fitted to them via the elastic modulus E and the viscosity η. This is true in case of the LAOS-measurements, which were conducted at $\omega = 2\pi\,f = 2\pi\,\mathrm{rad\,Hz}$.

In the following the LAOS-data with a maximum strain of $\varepsilon_0 = 5.01\,\%$ (Figure 4.4) are used, since the premature cardiomyocytes analysed in Chap. 3 exhibited a maximum strain of around $\varepsilon_0 = 5(\pm 2)\,\%$ on average (Sec. 3.3). Note that at a maximum strain of $\varepsilon_0 = 5.01\,\%$, the stress response was already slightly nonlinear (Figure 4.4). Thus, a linear approximation of the stress response is needed first. This can be achieved by omitting the higher harmonics in the Fourier series representation (Eq. (4.5)) of the data. The original Fourier series representation and the corresponding linear approximation is shown in Figure 4.6a. The fit of Eq. (4.8) to the linear approximation of the LAOS-data

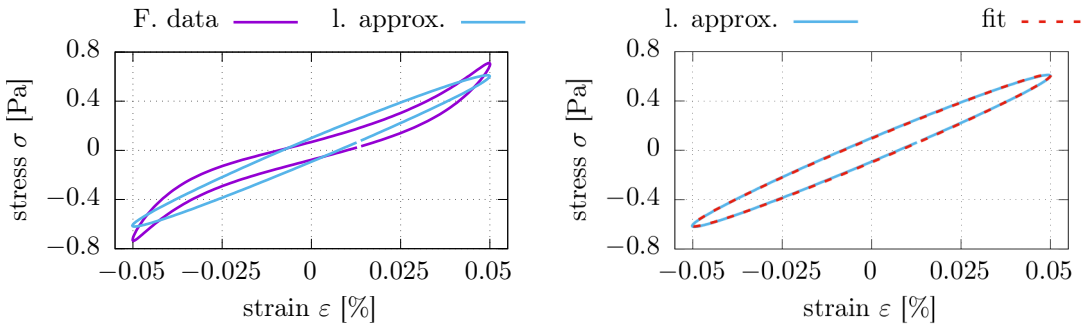

(a) Linear approximation (blue) of the LAOS-data (purple).

(b) Fit of Maxwell fluid (red) to the linear approximation (blue).

Figure 4.6.: Fit of the linear Maxwell fluid model to the LAOS-data obtained at a maximum strain of $\varepsilon_0 = 5.01\,\%$ and a shear frequency of $f = 1\,\mathrm{Hz}$.

Parameter	Value
E	$12.46\,\mathrm{Pa}$
η	$12.45\,\mathrm{Pa\,s^{-1}}$
E/η	$1\,\mathrm{s}$

Table 4.1.: Fitted viscoelastic parameters of the Maxwell fluid. E denotes the elastic modulus and η the viscosity. Note that the values have been rounded to the second decimal value.

is shown in Figure 4.6b. Both, the linear approximation of the slightly nonlinear data and the fit quality are convincing. The resulting elastic modulus E and the viscosity η are shown in Table 4.1.

Note that a high viscosity η in the context of the Maxwell model means that little energy is dissipated during one cycle of oscillation since the damper is in series with the spring (Figure 4.5). A very rigid damper acts like a rod and the elongations of the Maxwell model is governed by the energy conserving spring. Thus, the acquired results ($E \approx \eta$) make sense in the context of the narrow Lissajous curves (Figure 4.4), which indicate a rather energy conserving viscoelastic response of the extracellular matrix.

After fitting the Maxwell fluid model (Eq. (4.6)) to the viscoelastic response of the extracellular matrix after the polymerisation phase, it shall be analysed how the parameters of the model vary over time during the viscoelastic development of the system. For this purpose the conducted time sweep is facilitated (Figure 4.2). During the time sweep, the storage $G'(\omega)$ and the loss modulus $G''(\omega)$ of the medium under study have been recorded over around three hours. By solving Eq. (4.7b) and Eq. (4.7c) for the elastic modulus E and the viscosity η, which yields Eq. (4.9), they can be calculate from $G'(\omega)$ and $G''(\omega)$ at each recorded point in time. Thus the elastic modulus and the viscosity become functions of time $E \to E(t)$ and $\eta \to \eta(t)$. Note that the angular shear

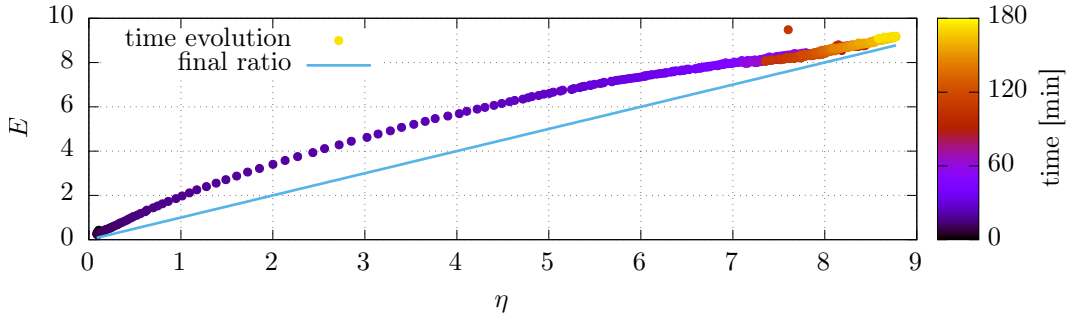

Figure 4.7.: Temporal evolution of the parameters of the Maxwell fluid. These are the elastic modulus E and the viscosity η. The blue line indicates the final ratio E/η after the polymerisation phase.

frequency is known to be $\omega = 2\pi\, f = 2\pi\,\mathrm{rad\,Hz}$.

$$E = G' \left(\frac{G''^2}{G'^2} + 1 \right) \tag{4.9a}$$

$$\eta = \frac{G''}{\omega} \left(\frac{G'^2}{G''^2} + 1 \right) \tag{4.9b}$$

Figure 4.7 shows the temporal development of $E(t)$ and $\eta(t)$. The time is colour coded to emphasise the relation between the elastic modulus $E(t)$ and the viscosity $\eta(t)$. To compare these results with the calculated values obtained from the fit to the LAOS-data, recorded after the polymerisation phase, the corresponding ratio E/η from Table 4.1 is drawn in blue. Although the time sweep was conduced in the **linear** response regime $\varepsilon_0 = 1\,\% \leq 3.16\,\%$, $E(t)$ and $\eta(t)$ converge against the ratio E/η predicted by the fit to the LAOS-data, which were recorded in the **nonlinear** response regime $\varepsilon_0 = 5.01\,\% \geq 3.16\,\%$. This finding validates the performed fitting of the linear Maxwell fluid model to the nonlinear LAOS-data – at least in the considered range of maximum strain. Furthermore, the temporal development of the elastic modulus and the viscosity show that the extracellular matrix becomes more viscous (increasing $\eta(t)$) and more elastic (increasing $E(t)$) over time, thus stiffer.

Note that, considering the discussion of the raw data (Sec. 4.2), the quantitative values of the results obtained in this section should be interpreted with great care. Nevertheless, the qualitative behaviour will be of avail when interpreting how the viscoelastic properties of the coupling of the self-sustained oscillators relates to the biological system of coupled premature cardiomyocytes.

5. Two Oscillator Model

Recent studies have shown that the direct and indirect mechanical coupling of cardiomyocytes leads to the synchronisation of their beating behaviour [13]. Synchronisation of nonadjacent premature cardiomyocytes can be observed in a petri dish. This raises the question of how the mechanical properties of the medium, acting as coupling agent, influence this effect. This chapter is dedicated to that question. It is studied how the material properties of a simple viscoelastic system, which provides the coupling for two self-sustained oscillators, influence their synchronisation behaviour. Note that this work was already published by my coworkers and me [60]. Thus, although some new results are shown, this chapter mainly orients itself on the mentioned publication[1].

It is evident to choose a self-sustained oscillator as a mathematical model for premature cardiomyocytes since they show self-sustained beating behaviour [31]. Self-sustained means that the oscillating objects use energy from an energy source to maintain their oscillating state. The harmonic oscillator for example, is *not* a self-sustained oscillator. In case of energy dissipation (damping), the exhibited oscillations will stop after all energy is drained from the system. In contrast, cardiomyocytes beat although they are damped by their environment.

Systems of coupled self-sustained oscillators and their synchronisation behaviour are subject of a vast number of studies [61, 62, 63, 64, 65, 66, 67]. These studies tackle different kinds of oscillators, ranging from simple one dimensional phase oscillators like the Kuramoto oscillator [34, 68], over amplitude oscillators like the Stuart-Landau oscillator [69, 70], to more dimensional oscillators used as models for different complex biological systems like cell calcium dynamics [13]. Usually those studies apply a purely elastic coupling in one dynamic variable and in this way neglecting the effects viscous coupling properties can introduce. Others, although incorporating some viscous coupling into their mathematical models and experiments, deal with very complex or specialised systems [71, 42, 72] and do not tackle the general question how viscoelastic coupling influences synchronisation compared to purely elastic coupling.

In this chapter, two Van der Pol oscillators [73] are coupled with the Maxwell model [74] to study the impact of viscoelastic coupling on their synchronisation behaviour. Premature cardiomyocytes exhibit asymmetric beating behaviour (Chap. 3). This motivates an additional questing. Namely, how an asymmetry in the potential generating the restoring forces of viscoelastically coupled oscillators is influencing their synchronisation behaviour. Thus, the classical Van der Pol equations are modified in a way such that they are able to produce asymmetric oscillations. The stability of the synchronous solutions of the system, in dependence on the viscoelastic coupling parameters and the

[1] Some text is directly copied and translated into passive.

asymmetry of the oscillations, are explored to study both: the impact of viscoelastic coupling on the synchronisation behaviour of self-sustained oscillators and the influence of the material properties of the medium, coupling the premature cardiomyocytes, on their synchronisation behaviour.

First, the mathematical models for the cardiomyocyte and the viscoelastic medium are introduced and motivated. Then, concepts of nonlinear dynamics, like bifurcation analysis, and the calculation of Lyapunov exponents and Poincaré maps, are applied to study the stability of the synchronised states of the system. A short summary and discussion of the obtained results and the limitations of this study is given at the end of this chapter.

5.1. Mathematical model

The model equations consist of two parts: two self-sustained oscillators and their coupling. Two of the most general amplitude oscillators used in many studies are the Stuart-Landau oscillator and the Van der Pol oscillator [73, 75, 35]. Both comprise only few parameters and span a two dimensional phase space. Since the Stuart-Landau oscillator is the normal form of a Hopf bifurcation, it only exhibits sinusoidal like oscillations. The Van der Pol oscillator however can be tuned to exhibit very nonlinear oscillations which are closer to those of cardiomyocytes. The most prominent, often called dimensionless[2], form of the Van der Pol oscillator is the following:

$$\ddot{x} = \mu \left(1 - x^2\right) \dot{x} - \omega^2 x. \tag{5.1}$$

In this equation, ω denotes the natural frequency[3] of the oscillator and μ is the parameter controlling the influence of the nonlinear damping. Figure 5.1 shows a representative example of the dynamics of the Van der Pol oscillator in case of a stable limit cycle. Considering the case of $\mu = 0$, the Van der Pol oscillator would be equivalent with the well known harmonic oscillator. For $\mu > 0$, the nonlinear damping drives a trajectory towards the symmetric and stable limit cycle of the system. This limit cycle becomes unstable for $\mu < 0$. That means that a trajectory would diverge to infinity or would approach the fixed point of the Van der Pol oscillator. There exists only one fixed point in phase space at $(x = 0, \dot{x} = 0)$ whose stability depends on μ.

Note that the system Eq. (5.1) consists of four terms but is controlled by two parameters rather than four. Obviously and without loss of generality, one out of four parameters can always be absorbed into the others, which would leave three parameters. Considering the Van der Pol oscillator as physical system, introduces in general two physical dimensions. One dimension in which time is measured and one in which the value of the dynamic variable x is measured. Thus, and by considering the *Buckingham-*Π *theorem*, the Van der Pol oscillator can be fully described by only one dimensionless

[2] As long as the Van der Pol oscillator is considered as a physical system, I do not agree with this convention as discussed in the following.

[3] Although ω is called natural frequency, the oscillation frequency depends on μ as well; but it is much more sensitive to ω.

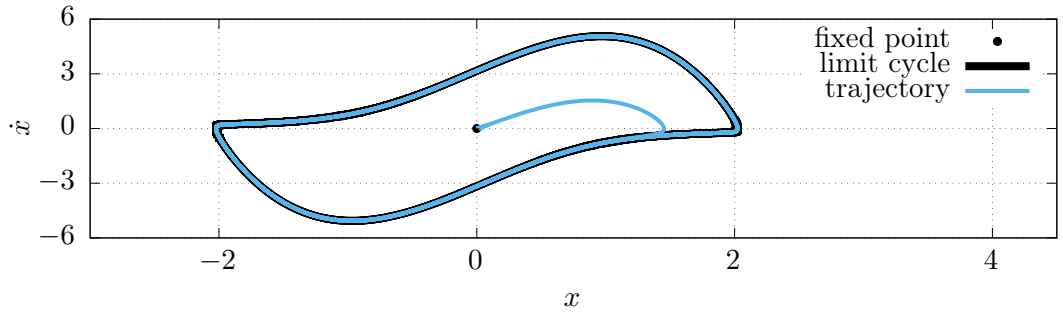

(a) Phase space dynamics: A trajectory starting close to the unstable fixed point and approaching the limit cycle.

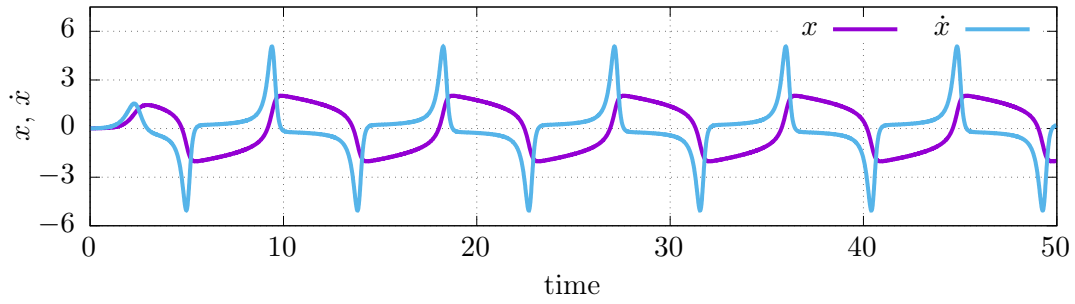

(b) Time domain dynamics: The same trajectory showing the oscillations of the dynamic variable x and its first derivative $\dot{x}$.

Figure 5.1.: Dynamics of the Van der Pol oscillator Eq. (5.1) with $\mu = 3$ and $\omega = 1$.

parameter. Having two parameters left means that either the dependent (x) or the independent (time) variable is still measured in terms of its physical dimension and not in terms of a system property (parameter combination). This is obviously time, since the statement $\left(1 - x^2\right)$ would be meaningless with a non-dimensionless dynamic variable. Furthermore, the very prominent choice of the semi-dimensionless form of the Van der Pol equation has important implications for the bifurcation behaviour of the system. Since ω enters only in squared form, the last term will always describe a linear restoring force independent of the sign of ω. Furthermore, the maximal amplitude of the limit cycle oscillations is fixed by the expression $\left(1 - x^2\right)$ rather than $\left(a - x^2\right)$. Thus, no single Hopf bifurcation is possible. Although this implications do not cause any problems with the following analysis, it is useful to keep them in mind when interpreting the results and the meaning of the parameters.

The Van der Pol oscillator exhibits symmetric[4] oscillations. For generating non-symmetrical oscillations, the restoring force of the Van der Pol oscillator, given by a harmonic potential, is perturbed by an exponential function.

$$\ddot{x} = \mu \left(1 - x^2\right) \dot{x} - \omega^2 \left(x + \varepsilon\, c \left[e^{c\, x} - 1\right]\right) \tag{5.2}$$

Here ε is called perturbation parameter and it is small in magnitude compared to all other parameters. $|c|$ is the length scale of the asymmetry introduced by the perturbation. The sign of c defines the side of the harmonic potential which is influenced stronger. Note that this perturbation does not change the fact that there exists only one fixed point and one potential limit cycle in the phase space. Figure 5.2 shows a comparison between the dynamics exhibited by the classical Van der Pol oscillator Eq. (5.1) and the asymmetric system Eq. (5.2). The additional term, controlled by the length scale of the asymmetry c, makes it possible to analyse how asymmetric oscillations influence the synchronisation behaviour of self-sustained oscillators in addition to the viscoelastic properties of the coupling. A comparison of the asymmetric oscillations generated by the introduced model with the beating signal of cell 1 can be seen in Figure 5.3. The qualitative similarities are evident. Both signals show the peak and the recover phase. Note that the signal generated by the asymmetric Van der Pol equation is inverted in time. The "recover phase" lies right before the peak phase, not right after it, like in the beating signal of the cardiomyocytes. This is a general property of the Van der Pol oscillator and cannot be overcome by just inverting the time in the system of differential equations (Eq. (5.2)), since a time inversion would render the limit cycle unstable. Furthermore, some quantitative linear transformations were necessary to emphasise the qualitative similarities of the two signals (see the caption of Figure 5.3). Since the following analysis focuses on the general and thus qualitative influence of viscoelastic coupling on the synchronisation behaviour of self-sustained oscillator, this is not a problem in general.

The perturbation used to make the oscillations of the Van der Pol oscillator asymmetric has the side effect that it renders the formerly linear restoring force nonlinear. To separate the effect of a asymmetric restoring force from a (symmetric) nonlinear restoring

[4]Symmetric in the sense of a point reflection in phase space.

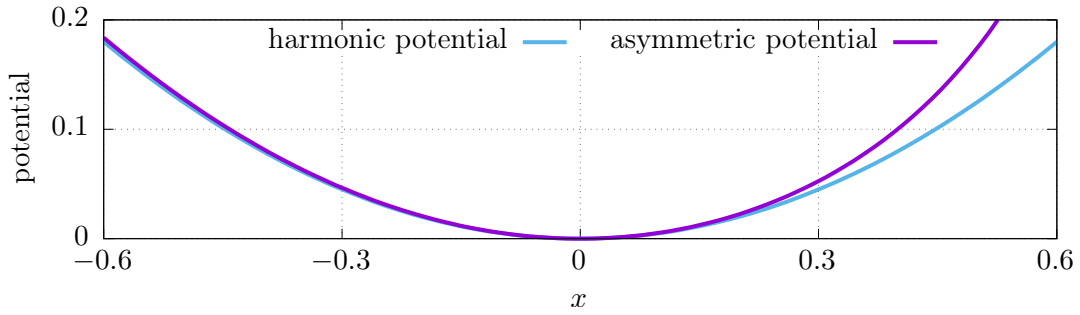

(a) The two potentials generating the restoring forces.

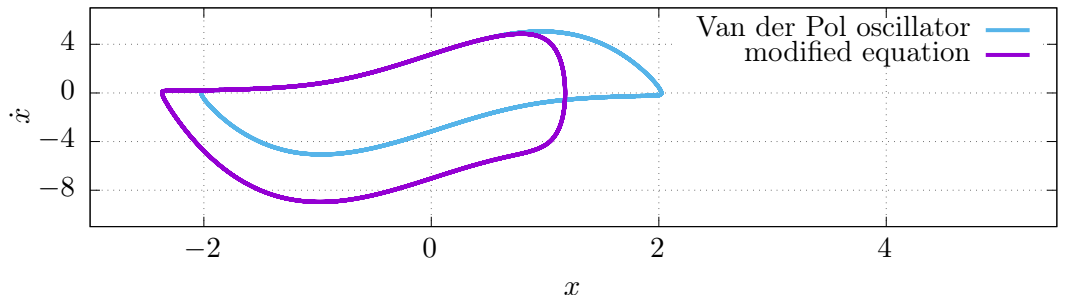

(b) Phase space portrait of the symmetric and asymmetric system.

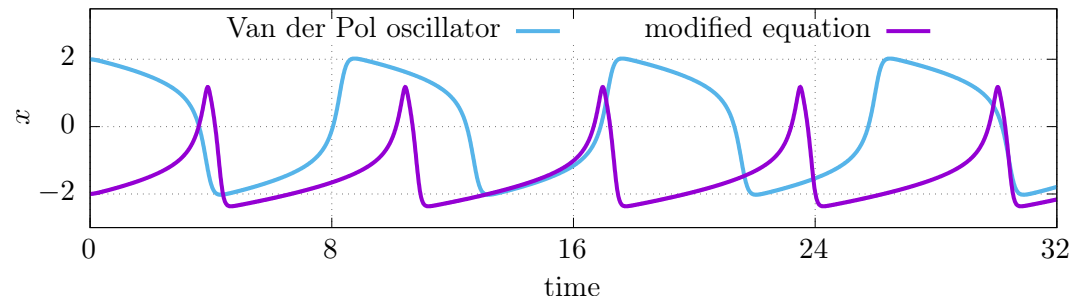

(c) Symmetric and asymmetric oscillations in the time domain.

Figure 5.2.: Comparison of the classical Van der Pol oscillator Eq. (5.1) with the asymmetric system Eq. (5.2). The parameters used are: $\mu = 3$, $\omega = 1$, $c = -8$, $\epsilon = 10^{-3}$.

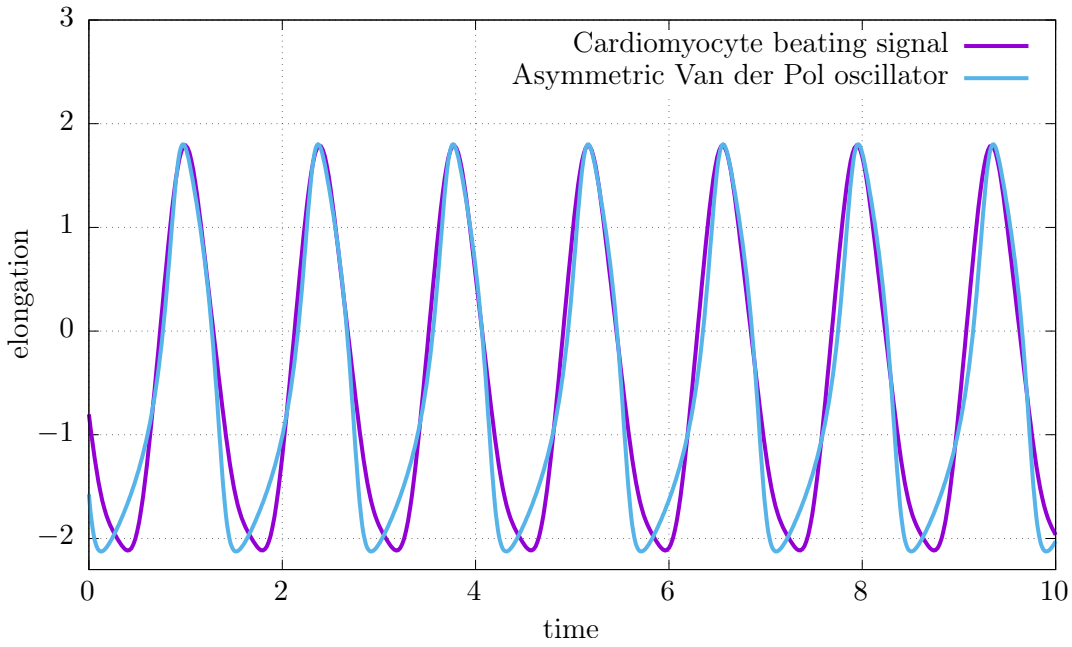

Figure 5.3.: Comparison of the oscillations generated by the asymmetric Van der Pol oscillator Eq. (5.2) with the beating signal of cell 1. The beating signal is represented by the corresponding Fourier series (see Figure 3.13). The following parameters were chosen for the mathematical model: $\mu = 5$, $\omega = 4.0$, $c = 4$, $\varepsilon = 10^{-3}$. For emphasising the qualitative similarities, the oscillations of the mathematical model were shifted in time by -6.8 and the amplitude of the beating signal was enlarged by a factor of 7.3 and shifted by -0.42.

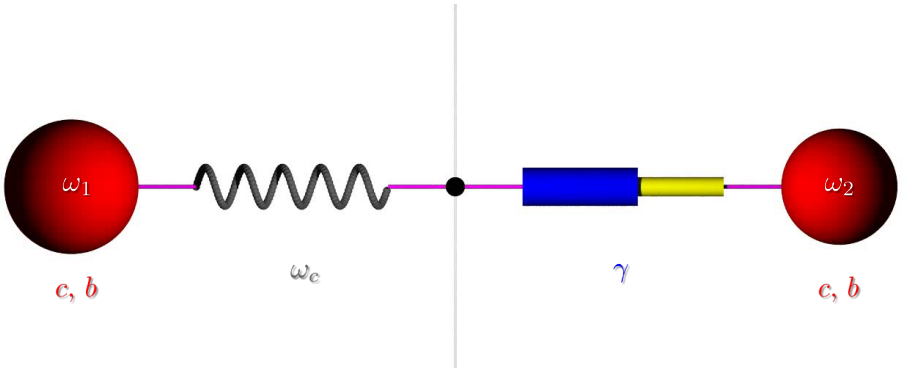

Figure 5.4.: Sketch of the Maxwell model (series connection of a harmonic spring with spring constant ω_c^2 and a linear damper with damping constant γ) which couples two oscillators with distinct natural frequencies ω_1, ω_2 like in Eq. (5.4). The position of the black dot in the middle corresponds to the value of the dynamic variable d.

force on the synchronisation behaviour of self-sustained oscillators, an additional term is introduced.

$$\ddot{x} = \mu\left(1 - x^2\right)\,\dot{x} - \omega^2\left(x + \varepsilon\, c\left[e^{c\,x} - 1\right] + b\,x^3\right) \tag{5.3}$$

Here $b \geq 0$ is the strength of the symmetric but nonlinear part of the restoring force. In the case of $c = 0$, Eq. (5.3) is called *Van der Pol-Duffing oscillator*.

The full model under study consists of two oscillators given by Eq. (5.3) coupled by a Maxwell fluid. The Maxwell fluid consists of a harmonic spring in series with a linear damper. The spring constant of the spring is ω_c^2 and the time scale on which the damping acts is γ^{-1}. We call ω_c elastic coupling parameter and γ fluidity (inverse viscosity) or viscous coupling parameter. Putting everything together yields the following system of differential equations:

$$\ddot{x}_1 = \overbrace{\mu\left(1 - x_1^2\right)\dot{x}_1 - \omega_1^2\left(x_1 + \varepsilon\, c\left[e^{c\,x_1} - 1\right] + b\,x_1^3\right)}^{\text{oscillator}} + \overbrace{\omega_c^2\,\left(\Delta x - d\right)}^{\text{elastic coupling}} \tag{5.4a}$$

$$\ddot{x}_2 = \mu\left(1 - x_2^2\right)\dot{x}_2 - \omega_2^2\left(x_2 + \varepsilon\, c\left[e^{c\,x_2} - 1\right] + b\,x_2^3\right) - \omega_c^2\,\left(\Delta x - d\right) \tag{5.4b}$$

$$\dot{d} = \overbrace{\gamma\,\left(\Delta x - d\right)}^{\text{viscous creep}} \quad \text{with} \quad \Delta x := x_2 - x_1. \tag{5.4c}$$

A sketch of the above system is shown in Figure 5.4. Although the two coupled oscillators are identical with respect to their asymmetry c and the strength of the symmetric nonlinear part of the restoring force b, they differ with respect to their natural frequencies ω_1 and ω_2. Thus, nonidentical oscillators are considered. For convenience, the parameter space of the natural frequencies $(\omega_1, \omega_2)^{\mathrm{T}}$ is parametrized by a centre of mass like parameter system $(\bar{\omega}, \omega_r)^{\mathrm{T}}$:

$$\begin{pmatrix}\omega_1\\ \omega_2\end{pmatrix} = \begin{pmatrix}\bar{\omega}(1 - \omega_r/2)\\ \bar{\omega}(1 + \omega_r/2)\end{pmatrix} \Leftrightarrow \begin{pmatrix}\bar{\omega}\\ \omega_r\end{pmatrix} = \begin{pmatrix}\frac{\omega_1 + \omega_2}{2}\\ \frac{\omega_2 - \omega_1}{\bar{\omega}}\end{pmatrix}. \tag{5.5}$$

Here $\bar{\omega}$ is the mean of the natural frequencies and ω_r is their relative deviation with respect to the mean. As discussed before, the time scale of this system can still be chosen to eliminate one parameter comprising the physical dimension of time. This is used to fix $\bar{\omega} = 1$.

To understand how the coupling was introduced, the following more abstract equations might be useful to consider.

$$\ddot{x}_1 = \overbrace{f_1(x_1, \dot{x}_1)}^{\text{oscillator}} + \overbrace{\sigma}^{\text{coupling}} \tag{5.6a}$$

$$\ddot{x}_2 = f_2(x_2, \dot{x}_2) - \sigma \tag{5.6b}$$

The oscillators are represented by f_i and the function which couples them is denoted by σ. The stress-strain relation of the Maxwell fluid (see Sec. 2.3) is given by:

$$\dot{\sigma} = E\,\dot{\varepsilon} - \frac{E}{\eta}\,\sigma \quad \Leftrightarrow \quad \begin{matrix} \sigma = E\,(\varepsilon - d) \\ \dot{d} = \frac{E}{\eta}\,(\varepsilon - d) \end{matrix}. \tag{5.7}$$

Renaming $E \to \omega_c^2$ and $E/\eta \to \gamma$, identifying the strain along the Maxwell fluid $\varepsilon = \Delta x = x_2 - x_1$, and by inserting Eq. (5.7) into Eq. (5.6) yields the coupled system Eq. (5.4). The coupling is an elastic spring, which adjusts its effective rest length over time, to fit its current elongation. d can be understood as this adjustment which happens on the time scale given by γ^{-1}. If the fluidity is equal to zero ($\gamma = 0$), the rest length of the spring stays constant. Thus, the coupling can be considered as perfectly elastic. If the fluidity approaches infinity $\gamma \to \infty$, the spring adjusts its rest length instantaneously which is equivalent to the case of no coupling.

The coupling in its present form (the last terms of Eq. (5.4a) and Eq. (5.4b)) was introduced to follow the standard approach of mutually coupling oscillators diffusively. Thus, the results of the following analysis of the system are comparable inside the field of nonlinear dynamics which deals with networks of coupled oscillators. This coupling approach shall be called pendulum approach or *pendulum picture* henceforth. It can be understood easily by considering the two coupled pendulums in Figure 5.5a. Two pendulums are coupled via a spring. The dynamic variables x_1 and x_2 are the displacements from their **reference positions**. Thus, the length of the spring between them is changed by the **difference** of their displacements: $\Delta x = x_2 - x_1$. If the length of the spring is changed, it exerts a force proportional to its elongation $\Delta x > 0$ or compression $\Delta x < 0$. In case of an elongation, the exerted restoring force F_r pulls the two pendulums together. Pendulum 1 is pulled in **positive** direction $F_{r,1} \propto +\Delta x$ while pendulum 2 is pulled in **negative** direction $F_{r,1} \propto -\Delta x$. Thus. their equation of motion look like:

$$F_{\text{total},i} = F_{\text{internal},i} \pm k\,\Delta x. \tag{5.8}$$

Where k is the proportionality factor of the restoring force. This kind of coupling **does not** describe the coupling between premature cardiomyocytes – at least not on the first glance.

The coupling of two cardiomyocytes is shown in Figure 5.5b. It shall be called *cardiomyocyte picture* henceforth. Two cardiomyocytes are coupled via a spring. The

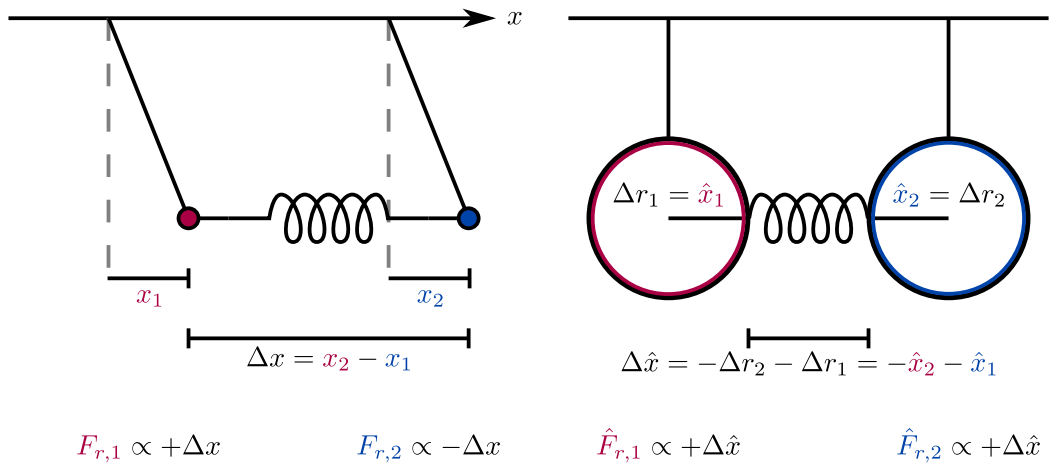

(a) Coupling in the pendulum picture.

(b) Coupling in the cardiomyocyte picture.

Figure 5.5.: The two equivalent coupling scenarios: the pendulum picture and the cardiomyocyte picture.

dynamic variables $\hat{x}_1$ and $\hat{x}_2$ are the variations of their **radii**. Thus, the length of the spring between them is changed by the negative **sum** of these variations: $\Delta\hat{x} = -\hat{x}_2 - \hat{x}_1$. If **both** radii decrease $\Delta x_2, \Delta x_1 < 0$, the spring is elongated $\Delta x > 0$ and if **both** radii increase $\Delta x_2, \Delta x_1 > 0$ the spring is compressed $\Delta x < 0$. In case of an elongation, the exerted restoring force $\hat{F}_r$ pulls on both radii of the cardiomyocytes. Thus, the radii feel a force which tries to **increase** them **both**: $\hat{F}_{r,1} = \hat{F}_{r,2} \propto +\Delta\hat{x}$. Thus. their equation of motion look like:

$$\hat{F}_{\text{total},i} = \hat{F}_{\text{internal},i} + k\,\Delta\hat{x}. \tag{5.9}$$

To use the developed system of equations (Eq. (5.4)), which comprises two oscillators coupled in the pendulum picture, for describing coupled cardiomyocytes, the pendulum picture coupling (Eq. (5.8)) must be equivalent to the cardiomyocyte picture coupling (Eq. (5.9)). This is shown in the following.

Eq. (5.10) describes the two coupled oscillators in the cardiomyocyte picture.

$$\ddot{\hat{x}}_1 = \mu\left(1-\hat{x}_1^2\right)\dot{\hat{x}}_1 - \omega_1^2\left(\hat{x}_1 + \varepsilon\, c\left[e^{c\,\hat{x}_1} - 1\right] + b\,\hat{x}_1^3\right) + \omega_c^2\,\left(-\hat{x}_2 - \hat{x}_1 - d\right) \tag{5.10a}$$

$$\ddot{\hat{x}}_2 = \mu\left(1-\hat{x}_2^2\right)\dot{\hat{x}}_2 - \omega_2^2\left(\hat{x}_2 + \varepsilon\, c\left[e^{c\,\hat{x}_2} - 1\right] + b\,\hat{x}_2^3\right) + \omega_c^2\,\left(-\hat{x}_2 - \hat{x}_1 - d\right) \tag{5.10b}$$

$$\dot{d} = \gamma\,\left(-\hat{x}_2 - \hat{x}_1 - d\right) \tag{5.10c}$$

By renaming $\hat{x}_1 \to x_1$ and $-\hat{x}_2 \to x_2$ Eq. (5.10) becomes Eq. (5.11).

$$\ddot{x}_1 = \mu\left(1-x_1^2\right)\dot{x}_1 - \omega_1^2\left(x_1 + \varepsilon\, c\left[e^{c\,x_1} - 1\right] + b\,x_1^3\right) + \omega_c^2\,\left(x_2 - x_1 - d\right) \tag{5.11a}$$

$$\ddot{x}_2 = \mu\left(1-x_2^2\right)\dot{x}_2 - \omega_2^2\left(x_2 - \varepsilon\, c\left[e^{-c\,x_2} - 1\right] + b\,x_2^3\right) - \omega_c^2\,\left(x_2 - \hat{x}_1 - d\right) \tag{5.11b}$$

$$\dot{d} = \gamma\,\left(x_2 - x_1 - d\right) \tag{5.11c}$$

Except for the term which introduces the asymmetric oscillations Eq. (5.11) is identical to Eq. (5.4). Thus, both systems are equivalent as long as symmetric oscillations are considered ($c = 0$). This means that the introduced system of equations Eq. (5.4) can be used as a tool to analyse the influence of viscoelastically coupling on the synchronisation behaviour of self-sustained oscillators and to relate those results to the coupled premature cardiomyocytes. Note that, while changing from the pendulum picture into the cardiomyocyte picture, x_2 changes its sign.

Now the term $\ddot{x}$ on the left hand side of Eq. (5.4a) and Eq. (5.4b) shall be discussed. One might be obliged to argue that this term is related to inertia force and that the system, comprising the premature cardiomyocytes and the collagen hydrogel providing their coupling, exists in a regime of low Reynolds numbers. Thus, the effect of the inertia term should be negligible. For a simple reason, this is not the case here. Second derivatives in time are necessary for a system to exhibit oscillatory behaviour. Furthermore, there is no need to interpret the oscillatory part of the system (the two Van der Pol oscillators) in a purely mechanical sense. Originally the Van der Pol oscillator was introduced as an abstract relaxation oscillator studied in the context of triode oscillations [73]. In the context of this thesis, the modified Van der Pol oscillator is used as an abstract and simplified model for the inner cell dynamics, which leads in the end to a self sustained oscillation of the cell membranes and these membranes are coupled via a Maxwell fluid.

There exists a vast number of rheological models as discussed in Sec. 2.3. For coupling the two modified Van der Pol oscillators, the Maxwell fluid was chosen over the Voigt material and other generalised series-parallel models, composed of multiple springs and dampers. The goal of this study is to get first insights into how viscoelastic coupling can influence the synchronisation of two coupled self-sustained oscillators. To do that, a model with a minimum number of parameters, one describing the elastic component and one describing the viscous component, is utile. By varying the parameter related to the viscous properties, the Voigt material becomes a solid rod or a elastic spring in the limit cases; where the Maxwell fluid becomes a elastic spring or a perfect liquid. The latter one sounds more reasonable to model a hydrogel.

Note that Eq. (5.4c), which represents the viscous creep, is a linear differential equation with time dependent inhomogeneity $\Delta x(t)$. This kind of equation can be solved with a Green's function approach. Doing this yields[5]:

$$d(t) = d_0\, e^{-\gamma\, t} + \gamma \int_0^t e^{-\gamma(t-\tau)}\, \Delta x(\tau)\, \mathrm{d}\tau. \tag{5.12}$$

Here $d(t = 0) = d_0$ is the initial condition which decays to zero over a time scale given by γ^{-1}. This means that Eq. (5.4c) introduces a distributed time delay coupling with an exponential integral kernel between the two oscillators under consideration. In this context, γ^{-1} can be considered as the amount of temporal memory of the distributed time delay coupling. Thus, small viscous coupling parameters γ correspond to a long

[5] See Sec. B.2 for the calculation.

temporal memory and large γ to a short one. Other studies have analysed the influence of distributed time delay coupling on amplitude death [63, 69], amplitude and phase dynamics [37], and the synchronisation of networks [38, 70] using identical and non-identical Stuart-Landau oscillators. Most of those studies discussed different kinds of time delay distribution and their influence on the mentioned topics. In this thesis the type of distribution will not change but the influence of the memory length on the synchronisation behaviour of in- and anti-phasic synchronisation states of two non-identical Van der Pol like oscillators will be analysed. Although the focus lies on the meaning of γ in the context of a viscoelastic coupling, the results obtained might be interesting in the field of coupled oscillators with distributed time delay as well and the reader is encouraged to keep this second possible interpretation of d and γ in mind while reading this chapter.

To summarise, the self-sustained and asymmetric (peak and recover phase (Chap. 3)) nature of the beating of premature cardiomyocytes motivated the choice of self-sustained oscillators, which are able to exhibit asymmetric oscillations, for analysing how the viscoelastic properties of their coupling is influencing their synchronisation. This self-sustained oscillators are a modified Van der Pol oscillators. For producing asymmetric oscillations, the former linear restoring force of the Van der Pol oscillator was modified with a exponential term. To distinguish between the effect of a *nonlinear asymmetric* restoring force and a *nonlinear symmetric* restoring force, an additional modification was performed. The final system under study consists of two modified and non-identical (with respect to their natural frequencies ω_i) Van der Pol oscillators coupled viscoelastically by a Maxwell fluid (Eq. (5.4), Figure 5.4). The Maxwell fluid was chosen because it utilises viscoelasticity in the form of only two parameters: its elasticity ω_c and its fluidity (inverse viscosity) γ. In the following it is analysed how the stability of the synchronised oscillating states of the system depends on the viscoelasticity of the coupling and on the parameters controlling the form of the oscillations. A comprehensive summary of all system parameters is given in Table 5.1 along with their default values. Note that for interpreting the results of this stability analysis in context of the coupled premature cardiomyocytes, one has to change from the pendulum picture into the cardiomyocyte picture, which changes the sign of $x_2 \to -\hat{x}_2$.

5.2. Results

As in systems with non-viscous but purely elastically coupled oscillators, the model Eq. (5.4) exhibits synchronisation of periodic oscillations in terms of phase locking. For analysing the fundamental differences between viscous and elastic coupling, it useful to focus solely on synchronisation states with 1:1 phase locking. In this case, only two types of synchronisation states remain: in-phase (1:1 phase locking) and anti-phase (-1:1 phase locking) synchronisation. Since the two Van der Pol oscillators have in general distinct

Parameter	Symbol	Default
damping constant	μ	3
mean of natural frequencies	$\bar{\omega}$	1
deviation of natural frequencies	ω_r	0.1
perturbation magnitude	ε	10^{-3}
length scale of asymmetry	c	0
strength of cubic nonlinearity	b	0
elastic coupling parameter	ω_c	1
viscous coupling parameter	γ	0.1

Table 5.1.: Summary of all system parameters. If not stated otherwise, all parameter values are set to these default values.

natural frequencies, it is not possible to obtain perfect 1:1 or -1:1 phase locking[6] in the sense of a constant phase lag of $\Delta\varphi = 0$ or $\Delta\varphi = \pi$, respectively. Therefore, in-phase and anti-phase synchronisation is defined as $0 \leq \Delta\varphi < \pi/2$ or $3\,\pi/2 < \Delta\varphi < 2\,\pi$, and $\pi/2 < \Delta\varphi < 3\,\pi/2$ with $\Delta\varphi \in [0, 2\,\pi)$, respectively. The model Eq. (5.4) is able to exhibit both, a slower[7] in-phase synchronisation and a faster anti-phase synchronisation state as shown in Figure 5.6. Note that a synchronised solution of two or many oscillators is, as well as the periodic solution of a single oscillator, given by a periodic orbit (closed one dimensional structure) in phase space. That is because all dynamic variables are "entangled" and exhibit periodic variations with identical periods in both cases. The time translation symmetry, which is common to all dynamic variables, makes the structure one dimensional. Thus, the dynamics of two or many synchronised oscillators can be viewed as the dynamics of one single oscillator of higher dimensionality in phase space. The ratio between the frequencies of the anti- and in-phase synchronisation state shown in Figure 5.6 is $f_{\text{anti}}/f_{\text{in}} \approx 2.03$. As shown in Figure 5.7, this ratio does not change much with respect to the viscous coupling parameter γ and it depends linearly on the elastic coupling parameter ω_c. Note that by changing from the pendulum picture into the cardiomyocyte picture, the sign change of $x_2 \to -\hat{x}_2$ makes the in-phase state in the pendulum picture the anti-phase state in the cardiomyocyte picture and the anti-phase state of the pendulum picture becomes the in-phase state in the cardiomyocyte picture. Whenever it is necessary to distinguish between those pictures, the synchronised states of the cardiomyocyte picture will be explicitly called: *in-phase-cmc* state and *anti-phase-cmc* state.

5.2.1. Synchronisation with symmetric linear restoring force

Each stable synchronisation state corresponds to an asymptotically stable, periodic orbit in phase space. In the following the case of a symmetric and linear ($c = 0$, $b = 0$) restoring

[6] There exists a singular parameter limit case which force the oscillators to perfectly synchronise in-phasic: $\omega_c \to \infty$ and $\gamma = 0$. In this case, the Maxwell fluid would be equivalent to a solid rod.

[7] In terms of the periods of the shown periodic solutions.

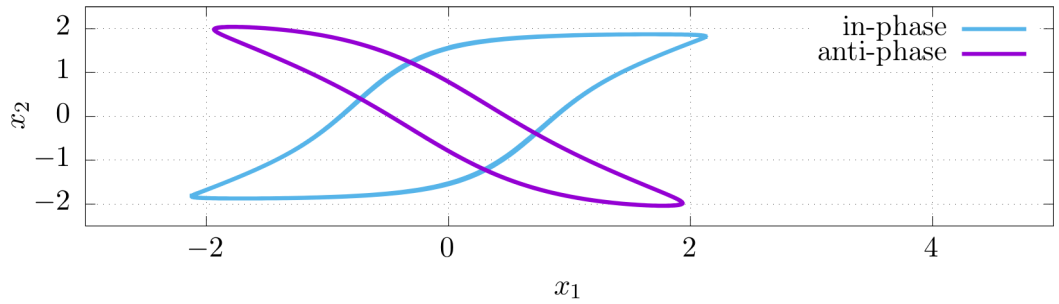

(a) Phase space projection of the periodic orbits of the in- and anti-phase synchronisation state.

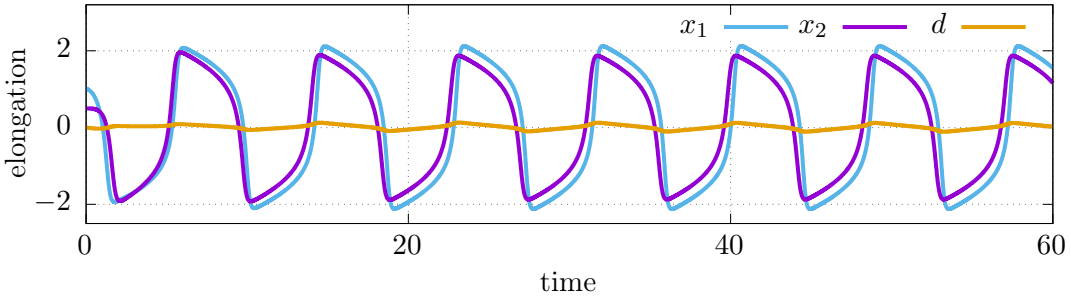

(b) Slow in-phase synchronisation state.

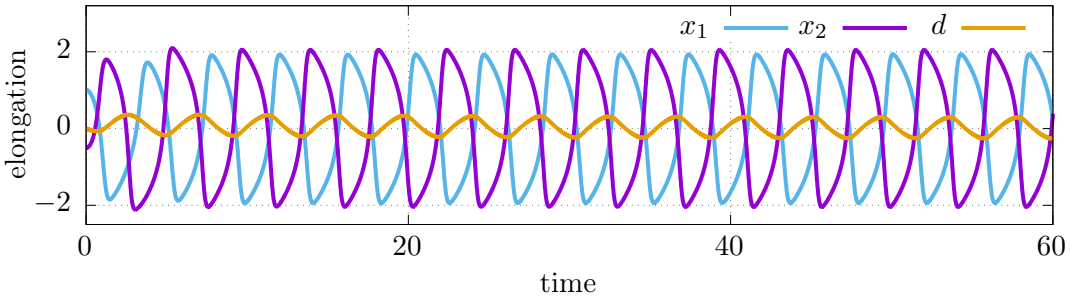

(c) Fast anti-phase synchronisation state.

Figure 5.6.: Two coexisting stable periodic solutions of the model under study Eq. (5.4). The initial conditions determine in which state the coupled oscillators will end up.

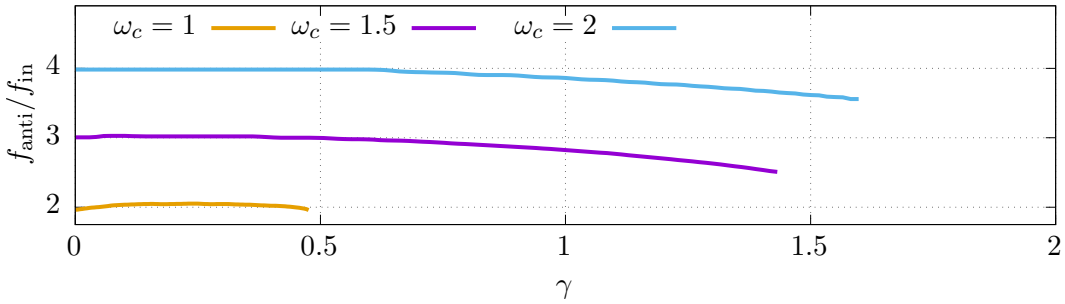

(a) Frequency ratio with respect to the viscous coupling parameter γ.

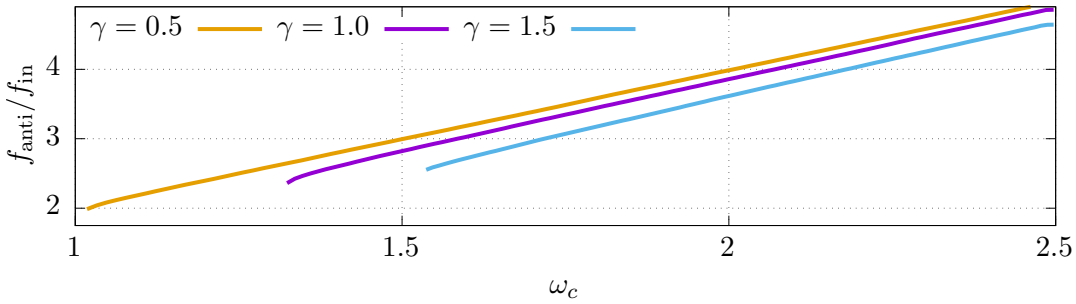

(b) Frequency ratio with respect to the elastic coupling parameter ω_c.

Figure 5.7.: Ratio between the frequencies of the in- and anti-phase synchronisation states. The length of the lines is determined by the ω_c-γ parameter regime in which the in- and anti-phase synchronisation states coexist (see Figure 5.9 below in the text).

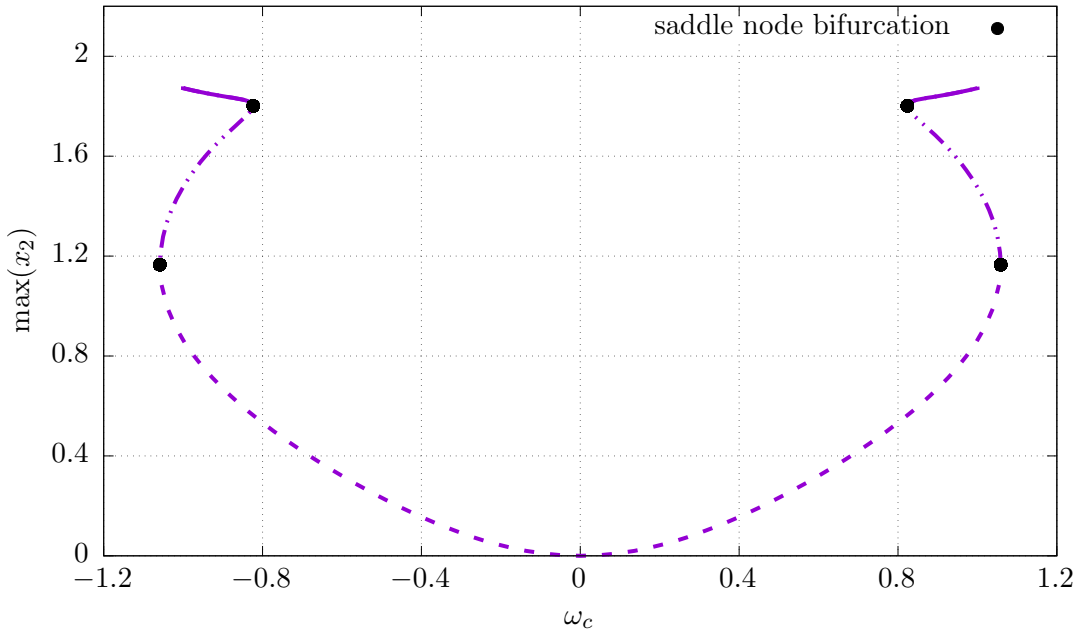

Figure 5.8.: Bifurcation diagram of the in-phase orbit. Periodic orbits are represented by a scalar value, the maximum amplitude of the second oscillator $\max(x_2)$, in dependence on the elastic coupling parameter ω_c. For a given ω_c value, the number of $\max(x_2)$ values is equivalent to the number of coexisting orbits. Solid lines denote globally stable orbits and dashed lines denote unstable orbits (dotted dashed: periodic saddle, dashed: periodic repeller). The points where saddle node bifurcations occur are marked with a black circle.

force is considered. It is analysed how the stability of the two periodic orbits, in-phase (1:1) and anti-phase (-1:1), depends on the elastic and viscous coupling parameters ω_c and γ, respectively. For doing this, the bifurcation analysis tool AUTO [76, 77] was used.

The orbits are born and perish due to saddle node bifurcations which are pair productions and pair annihilations of stable orbits with their unstable counterparts. These bifurcations can easily be found by varying the elastic coupling parameter ω_c, since the coupling strength of the two oscillators vanishes in the limit of $\omega_c \to 0$ and without coupling there is no synchronisation. Figure 5.8 shows a bifurcation diagram of the in-phase orbit while varying ω_c. It can be seen that the in-phase synchronisation state (stable in-phase orbit) exists until the elastic coupling parameter decreased to $\omega_c \approx 0.8$. A saddle node bifurcation happens at this point. The stable orbit collides with an unstable one and both cease to exist. Since the model equations Eq. (5.4) depend only on ω_c^2, the diagram possesses a reflection symmetry at $\omega_c = 0$.

The parameter value at which the in-phase synchronisation state is born is called bifurcation value ω_c^*. The bifurcation value might change by varying an additional

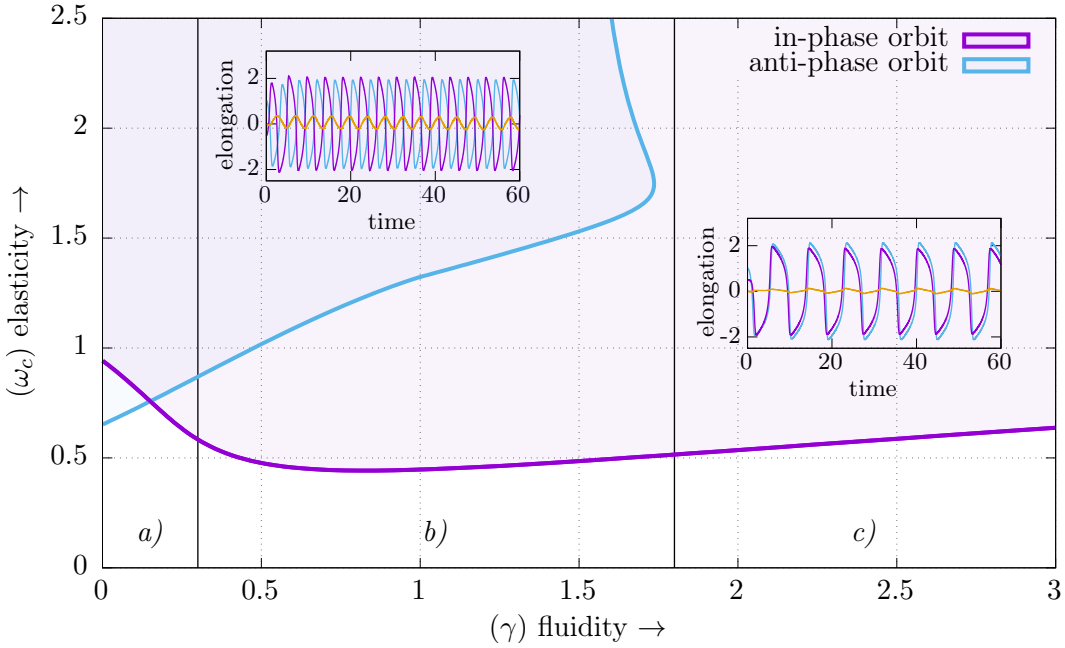

Figure 5.9.: Phase diagram (spanned by the elastic ω_c and viscous γ coupling parameter) showing the continuation curves of the saddle node bifurcations which give rise to the different synchronisation states. Above each line, the corresponding asymptotically stable periodic orbit exists. Note that both synchronisation states coexist if parameter combination which lie above both lines are considered. In this case, the initial conditions decide in which state the system will end up. The vertical black lines separate three different regions of interest.

model parameter p. Thus, the bifurcation value might depend on this parameter $\omega_c^* \equiv \omega_c^*(p)$. Following the bifurcation value in parameter space while varying p is called *continuation*[8]. Such a continuation, featuring the elastic and viscous coupling parameter $\omega_c^* \equiv \omega_c^*(\gamma)$, is shown in Figure 5.9. The phase diagram shows a blue and a purple saddle node bifurcation curve corresponding to the anti-phase and the in-phase orbit, respectively. Above those curves the corresponding orbit exists. On the curves the stable orbits collide with their unstable counterparts and vanish due to a saddle node bifurcation. Below both curves only quasi-periodic solutions exist corresponding to not synchronised states. The anti-phase and the in-phase orbit are both located on the same two dimensional torus in phase space. Quasi-periodic solutions are filling this torus. Increasing the fluidity γ yields three distinct effects, which can be seen in the different parts *(a), b), c)*) of Figure 5.9. If the two oscillators are coupled purely elastically

[8]Note that the choice of the domain and the codomain with respect to the relation $\omega_c^* \equiv \omega_c^*(p)$ is arbitrary. One could start with finding a bifurcation value p^* and flowing this value while varying ω_c. The curves in parameter space given by $\omega_c^* \equiv \omega_c^*(p)$ and $p^* \equiv p^*(\omega_c)$ are identical.

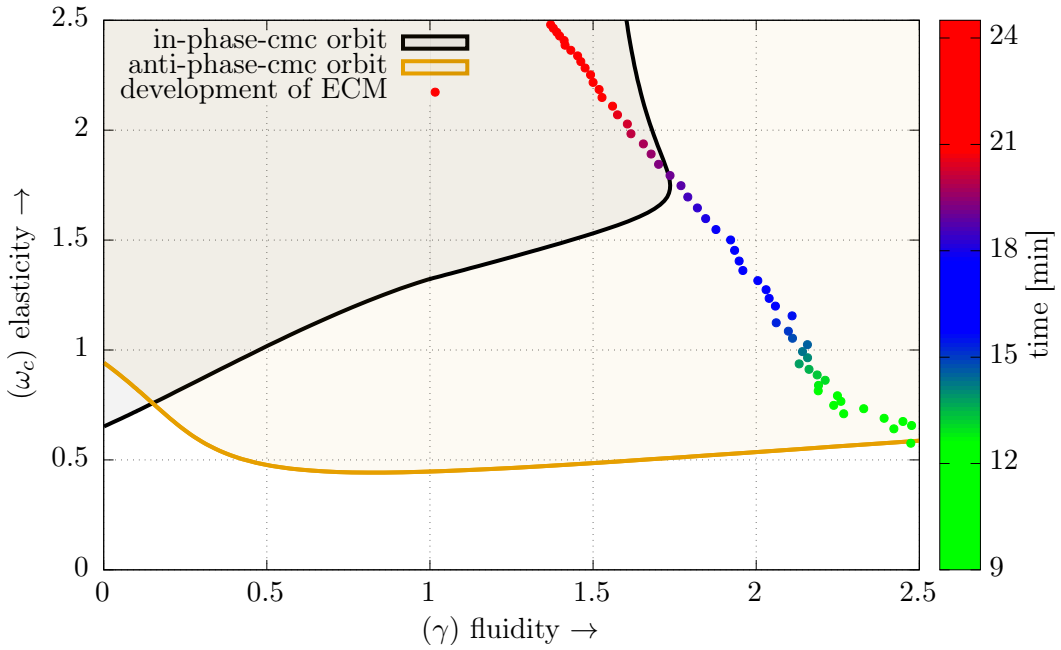

Figure 5.10.: Phase diagram (spanned by the elastic ω_c and viscous γ coupling parameter) in the cardiomyocyte picture. Above each line, the corresponding stable synchronisation state exists. The colour coded dots show the stiffening of the extracellular matrix (ecm) over time (Figure 4.2, Figure 4.7).

($\gamma = 0$), the anti-phase orbit emerges before the in-phase orbit does when increasing the elastic coupling strength ω_c. As soon as the fluidity γ reaches a certain value, one observes a behaviour which is the other way round (part *a)*). At higher fluidity (part *b)*), a strictly increasing elastic coupling strength is necessary for the anti-phase orbit to emerge while the elastic coupling strength needed for the in-phase orbit to emerge stays nearly constant. Furthermore, there is a critical value of γ at which the system will never reach an anti-phase synchronisation regardless of the value of ω_c. If the fluidity γ is increased even further (part *c)*), a strictly increasing elastic coupling strength ω_c is needed for the in-phase orbit to emerge. This is because a fluidity approaching infinity would describe a medium which does not provide any diffusive coupling at all (e.g., liquid water). In terms of the model equations Eq. (5.4), the limit $\gamma \to \infty$ leads to a spring which adapts its rest length infinity fast, thus providing no coupling forces.

These results indicate that systems composed of periodically oscillating components which are coupled viscoelastically may have a tendency to synchronise in-phase at low coupling strengths if the viscosity of the system is sufficiently low. Or considering the delay coupling interpretation Eq. (5.12); systems with a short temporal memory (large γ) may have a tendency to synchronise in-phase.

Figure 5.10 shows the discussed phase diagram (Figure 5.9) translated into the cardiomyocyte picture. Here, the in-phase state corresponds to the anti-phase-cmc state

and the anti-phase state corresponds to the in-phase-cmc state. Additionally, the temporal stiffening behaviour of the extracellular matrix, extracted from the time sweep measurements (Chap. 4, Figure 4.2, Figure 4.7), is shown. When the cells and the collagen gel are brought together, the medium is rather liquid. After some time, the medium is remodelled by fibroblasts and becomes stiffer [21, 22, 18, 15, 78, 19]. The phase diagram of the cardiomyocyte picture (Figure 5.10) suggests a stiffness boundary, given by the bifurcation curve of the in-phase-cmc orbit, the extracellular matrix has to cross before the cardiomyocytes are able to synchronise since no in-phase-cmc synchronisation can be found (independent of the elastic coupling parameter ω_c) if the fluidity γ of the extracellular matrix is to high. Note that, given the temporal path the medium takes in the phase diagram, the anti-phase-cmc orbit is stable before the in-phase-cmc orbit. This raises the question, why the premature cardiomyocytes to not synchronise in an anti-phase manner. The inner mechanism which makes premature cardiomyocytes contract – the inner calcium oscillations in context of the excitation-contraction coupling (Sec. 2.1) – might be the reason. By sensing the mechanical signals of their neighbours, the excitation-contract coupling of premature cardiomyocytes might by triggered sooner; thus, shifting the phase of their inner calcium oscillations. Because of the following refractoriness, this phase shifts can only lead towards an in-phasic entanglement and not away from it.

The frequencies of the two synchronisation states (of the pendulum picture) can be easily determined by inverting the average time between two distinct (with positive derivative) roots of adjacent oscillations. This can be done for every ω_c-γ-parameter combination shown in the phase diagram (Figure 5.9); yielding frequency maps in parameter space. Two frequency maps are shown in Figure 5.11. The two maps were generate by using two different sets of initial conditions to define which frequency is shown in the parameter regime in which both states coexist. One set favours the anti-phase synchronisation state (Figure 5.11a) while the other favours the in-phase state (Figure 5.11b). In all other parameter regimes, the frequency of the only existing state is shown regardless of the initial conditions chosen. In the regime in which no synchronisation state exists and only quasi periodic solutions occur (gray region below both yellow lines), no single oscillation frequency can be determined. The amplitude of the second oscillator x_2 was used for calculating the maps. Furthermore, two line scans of Figure 5.11a are provided in Figure 5.12.

It can bee seen that the frequency of the anti-phase synchronisation state depends linear on the elasticity ω_c of the coupling and decreases slightly with its fluidity γ. In the context of a distributed time delay coupling Eq. (5.12), this means that the frequency of the anti-phase state does not change much with the coupling's time scale of memory γ^{-1}. The frequency of the in-phase synchronisation state is bound by a small frequency window given by the frequencies of the single **uncoupled** oscillators. Thus, the frequency of the in-phase state is rather constant with respect to the viscoelastic coupling parameters. The only noticeable dependence is that the in-phase frequency converges against the mean of the frequencies of the uncoupled oscillators with increasing coupling strength ω_c (see subplot in Figure 5.12). This suggests that the two synchronisation

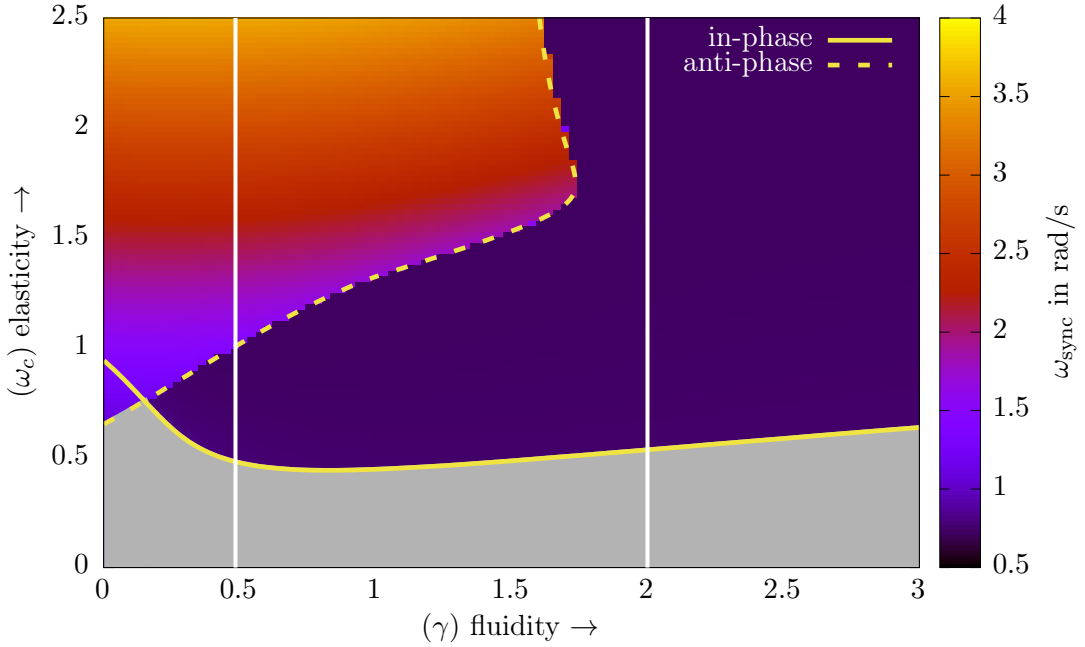

(a) Frequency map generated with initial conditions favouring the anti-phase state. The vertical white lines denote line scans shown in Figure 5.12.

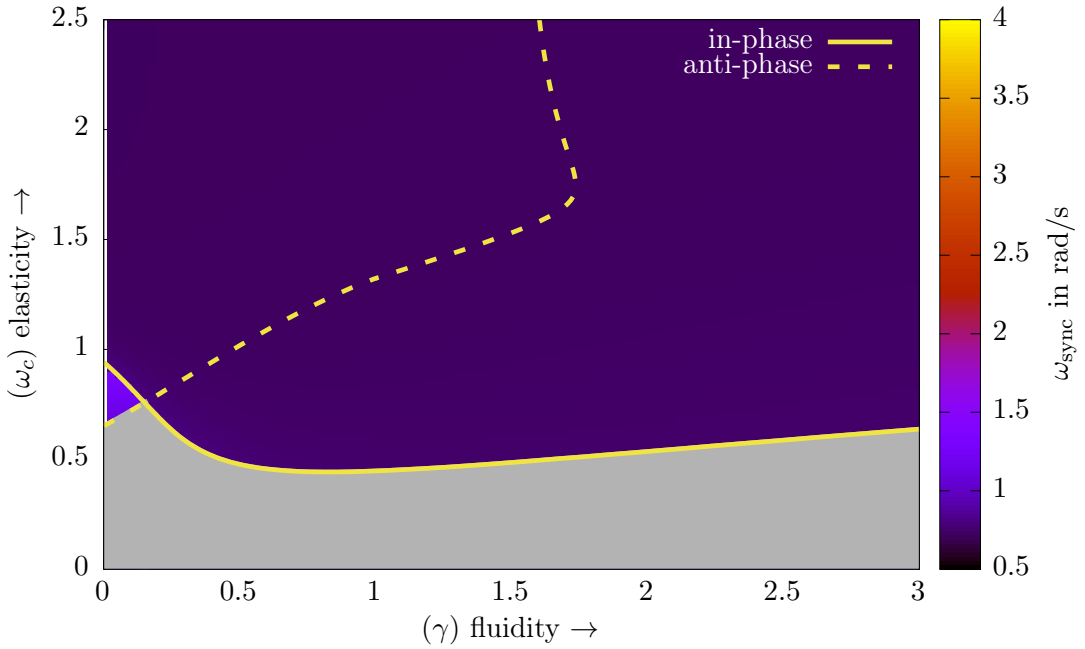

(b) Frequency map generated with initial conditions favouring the in-phase state. See Figure A.15 for a colour map providing a higher contrast.

Figure 5.11.: Maps in parameter space showing the colour coded frequencies of the different synchronisation states in dependence on the elastic ω_c and viscous γ coupling parameter. Above the bifurcation curves (yellow lines), the corresponding synchronisation state exists (see Figure 5.9). In case of two coexisting synchronisation states, the initial conditions determine which state is reached; thus, which frequency is shown. In the absence of synchronisation (below both yellow lines), no meaningful frequency can be determined.

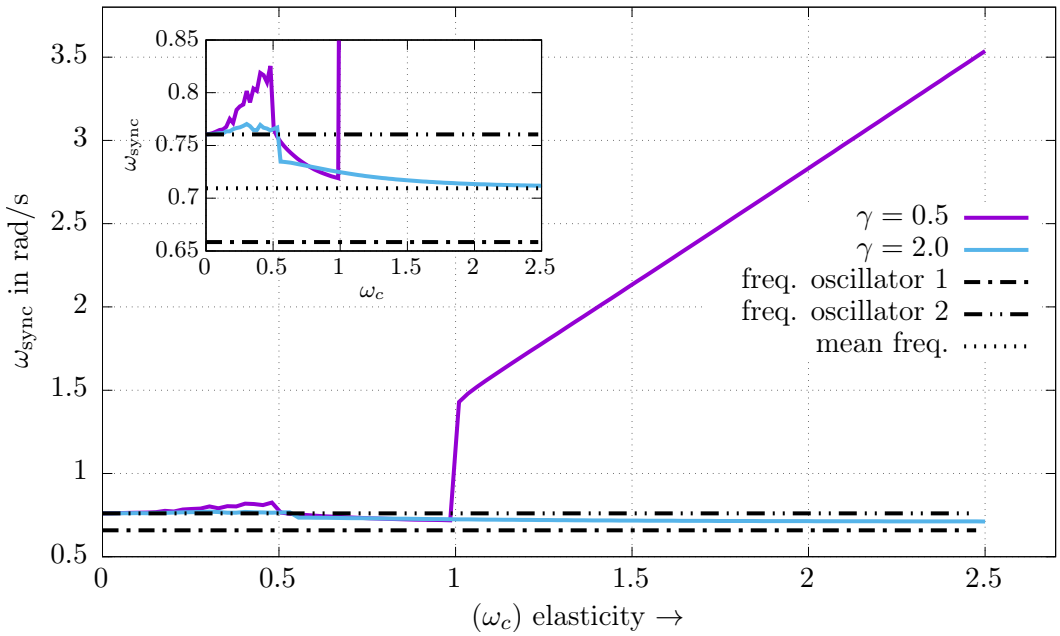

Figure 5.12.: Two line scans of the frequency map (Figure 5.11a) at different γ values. The dashed black lines denote the frequencies of the two **uncoupled** ($\omega_c = 0$) oscillators and their average frequency. The subplot shows a zoom with respect to the frequency axis. Note that the very steep in- or decreases of the synchronisation frequency are actual discontinuous caused by the saddle node bifurcations.

states are dominated by different components of the system.

The very existence of the anti-phase state might be caused by the linear elastic spring in the coupling (Figure 5.4) since a more fluid coupling (large γ) renders the anti-phase state unstable (Figure 5.9) and its frequency can perfectly be tuned by the spring's spring-constant ω_c^2. In this case, the linear spring dominates the two coupled oscillators and defines the time scale of the oscillations observed in the system. On the other hand, in case of the in-phase synchronisation, the dynamics is dominated by the two coupled self-sustained oscillators. The frequency of the in-phase synchronisation state is defined by the natural frequencies of the coupled oscillators and does not depend significantly on the coupling parameters.

In Figure A.16, the form of oscillations exhibited by the in- and anti-phase synchronisation states are compared. The form of oscillations of the in-phase state stays rather constant while varying the elastic coupling strength ω_c and it is similar to the oscillations exhibit by a single uncoupled oscillator. The form of oscillation of the anti-phase state changes while the elastic coupling strength is varied. With increasing ω_c, the oscillations become more sinusoidal; thus they become more similar to the oscillation a harmonic oscillator would exhibit. This supports the theory that the anti-phase synchronisation state is dominated by the linear spring and that the in-phase state is dominated by the properties of the coupled oscillators.

Considering the synchronisation of premature cardiomyocytes and switching into the cardiomyocyte picture, this result raises the question why cardiomyocytes to not show in reality the very high frequencies the in-phase-cmc (the anti-phase state in the pendulum picture) state exhibits. This can be explained by considering the excitation-contraction coupling again. Since cardiomyocytes are refractory after they have beaten, they cannot adopt to frequencies which are much higher than their on natural frequency. Furthermore, these results suggest an optimal elasticity ω_c of the extracellular matrix for the cardiomyocytes to synchronise. The very elastically might be optimal for which the in-phase-cmc state features a frequency which is similar to the natural frequencies of premature cardiomyocytes.

5.2.2. Synchronisation with asymmetric restoring force

It was analysed how the viscoelastic coupling parameters are influencing the synchronisation of two viscoelastically coupled Van der Pol oscillators ($c = 0$, $b = 0$). The question which role the (a)symmetry ($|c| \geq 0$, $b = 0$) of their oscillations plays shall be tackled now. The dimensionless Van der Pol equations were modified to produce asymmetric oscillations. In this context, the parameter c was introduced, which is the length scale of asymmetry in the potential generating the restoring force (see Eq. (5.2) and Figure 5.2). For analysing how the resulting asymmetry of the oscillations is influencing the synchronisation behaviour of the coupled oscillators, a bifurcation diagram with respect to c was calculated and is shown in Figure 5.13[9]. For the symmetric case

[9]The L^2-norm was chosen to emphasise the reflection symmetry at $c = 0$ and it is defined as follows: Let T be the period of an orbit, N the number of dimension of the system, and u_k the dynamic variables. Then $L^2\text{-norm} \equiv \sqrt{\frac{1}{T}\int_0^T \sum_{k=1}^N u_k(t)^2 \, \mathrm{d}t}$.

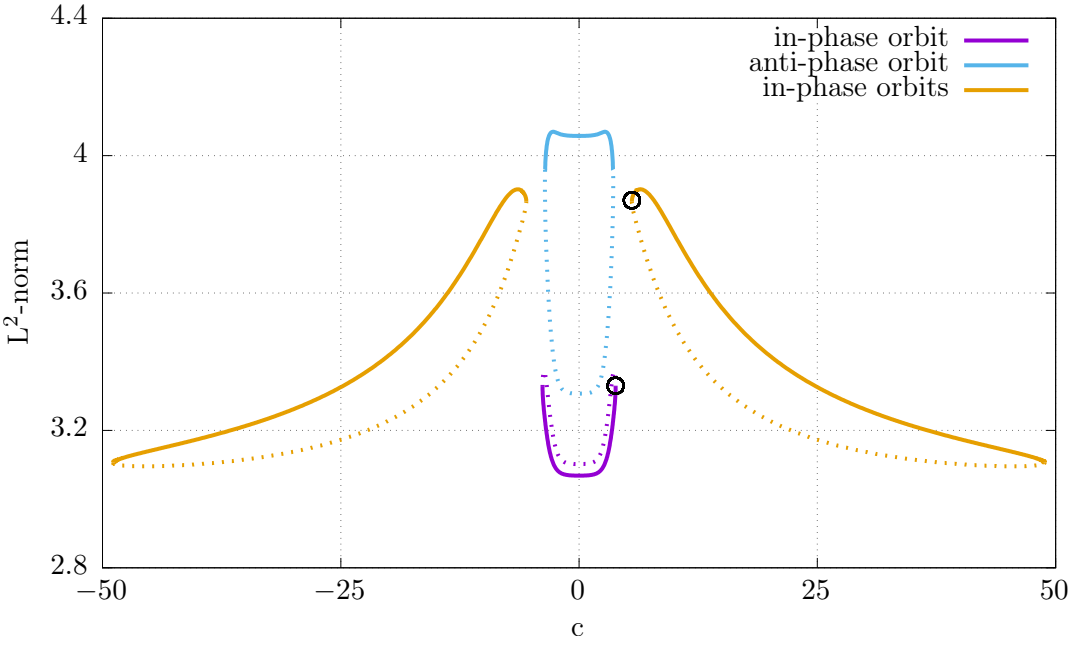

Figure 5.13.: Bifurcation diagram showing stable and unstable periodic solutions of the two viscoelastically coupled van der Pol oscillators with asymmetric restoring force. Unstable periodic solutions are marked as dotted lines. Plotted is the L^2-norm of each orbit vs. the asymmetry parameter c. Furthermore, two saddle node bifurcations are marked with black circles.

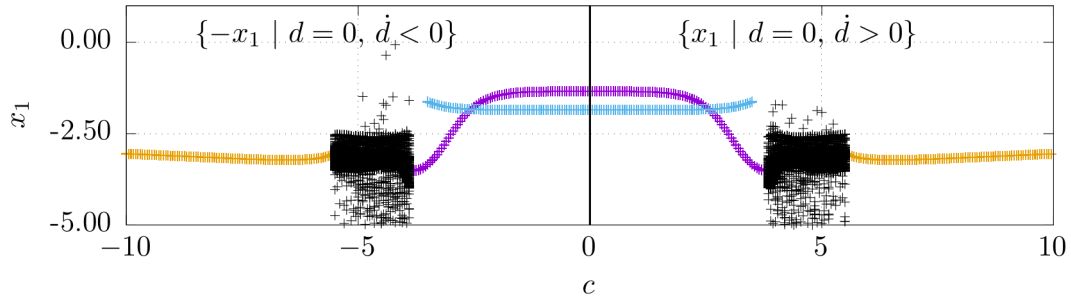

(a) Bifurcation diagram created via plotting the elongation of the first oscillator x_1 of the associated Poincaré map. Two different Poincaré surfaces were chosen to emphasise the symmetry.

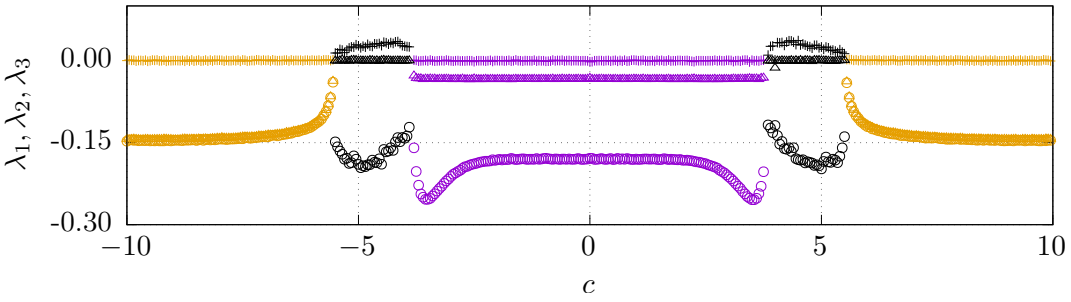

(b) The three largest Lyapunov exponents λ_1, λ_2, λ_3 of the system Eq. (5.4), both vs. the asymmetry parameter c.

Figure 5.14.: Lyapunov exponents and a bifurcation diagram revealing a chaotic solution. The colours indicate the type of solution. Purple: in-phase orbit, blue: anti-phase orbit, orange: in-phase orbit, and black: chaotic region.

($c = 0$), the two asymptotically stable, coexisting, periodic orbits correspond to the in- and anti-phase synchronisation states and their unstable counterparts can be seen. The purple and the blue line correspond to the in- and anti-phase orbit respectively. As the asymmetry increases ($|c| > 0$), all orbits remain until a critical value is reached where they vanish due to a saddle node bifurcation (the anti-phase orbit vanishes before the in-phase orbit does). After that point, there is a region in which no synchronisation takes place. As it can be seen in Figure 5.14, the system has a chaotic solution in this region since the largest Lyapunov exponent is greater than zero ($\lambda_1 > 0$). If the oscillations become even more asymmetric, a saddle node bifurcation takes place which gives rise to a single asymptotically stable in-phase orbit, which is stable for a wide range of $|c|$ values, denoted by the colour orange. The oscillations of this synchronisation state are shown in Figure 5.15. Note that the new born synchronisation state can be classified as in-phasic since the phase lag between the two oscillators is $\Delta\varphi \approx 5\,\pi/11 < \pi/2$.

It shall be analysed now, how the existence of chaotic solutions depends on the viscous effects of the coupling. Figure 5.16 shows the two largest Lyapunov exponents λ_1 and λ_2 of the system in γ-c parameter space. One can see that the system exhibits chaos

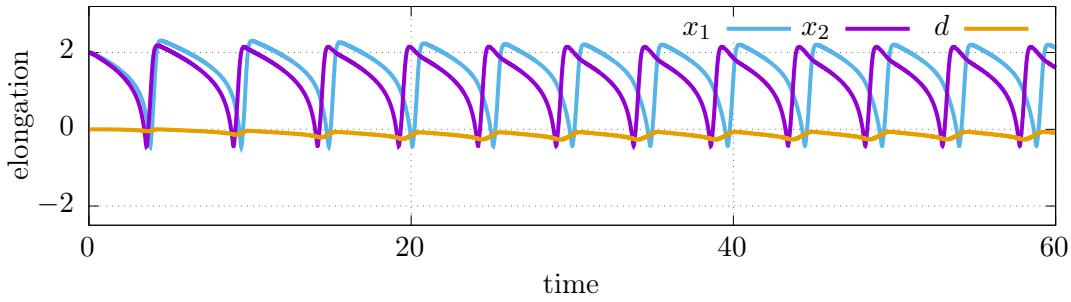

Figure 5.15.: Transient ($t < 20$) and asymptotically stable in-phase synchronisation state occurring at $c = -20$ (Figure 5.13). See Figure 5.6 for comparison.

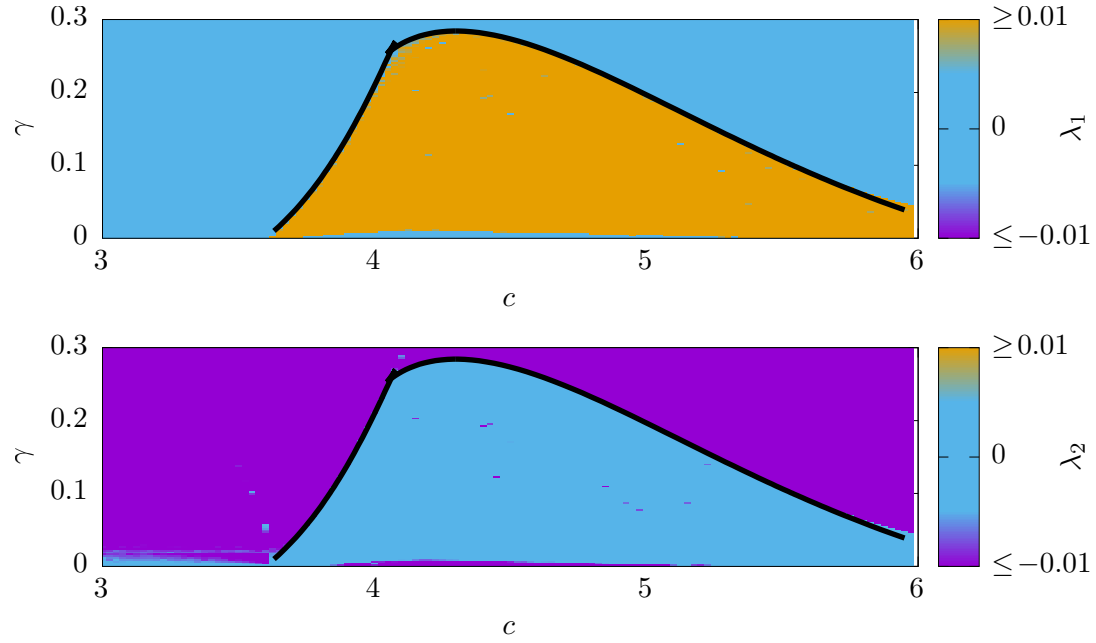

Figure 5.16.: Two largest Lyapunov exponents λ_1 and λ_2 showing a parameter regime in which the system exhibits chaotic dynamics. The chaotic regime is bordered by the bifurcation curve of the saddle node bifurcations marked in Figure 5.13. Note that for vanishing viscous coupling parameter γ, the largest Lyapunov exponent is zero independent of the asymmetry parameter c.

($\lambda_1 > 0$) only for a specific c-range, which depends on the fluidity γ. This result was checked by continuing the two saddle node bifurcations marked in Figure 5.13 and by plotting their bifurcation curves on top of the Lyapunov exponent map. By increasing γ, the bifurcation points come closer together until they annihilate each other, leaving a stable and continuous (with respect to c) in-phase solution without any chaotic regime in between. Note that there is no chaos to be found at $\gamma = 0$ ($\lambda_1 \leq 0$). In this case, the second largest Lyapunov exponent is equal to zero as well. This can be explained by looking at the first derivative of the dynamic variable d in Eq. (5.4c). Since $\gamma = 0 \Rightarrow \dot{d} \equiv 0$ a perturbation in d will neither grow nor decay. This is also true for a perturbation in the direction of the limit cycle corresponding to one of the two synchronisation states. Because there are two dimensions in phase space in which a perturbation will be constant in average, there have to be two Lyapunov exponents equal to zero. Furthermore, we have calculated the Lyapunov exponents in ω_c-c parameter space with $\gamma = 0$. There was no chaos to be found. Thus, chaotic oscillations occur for the coupled system only in the case of viscous coupling ($\gamma > 0$) and asymmetric restoring forces ($|c| > 0$).

The obtained results show that in-phase synchronisation is favoured over anti-phase synchronisation by self-sustained oscillators which exhibit asymmetric oscillations. This can be explained by recalling that the frequency and the oscillation form of the anti-phase synchronisation state is dominated by the elastic spring in the coupling, which forces the self-sustained oscillators to oscillate more sinusoidal if synchronised anti-phase (see Figure 5.12 and Figure A.16). Sinusoidal oscillations are symmetric. In addition to the nonlinear damping of the oscillators, the introduced asymmetry parameter c enforces non-sinusoidal oscillations in terms of an asymmetric oscillations form. Thus, non vanishing values of c render it more difficult for the elastic spring to take over. Since the self-sustained oscillators maintain their natural oscillation properties if synchronised in-phase (see Figure A.16), asymmetric oscillations can be featured without problems by this state. Nevertheless, increasing the asymmetry c increases the frequency shift between the coupled oscillators. This means that an increasing effective coupling strength is needed for maintaining synchronisation. Thus, if the coupling strength is not increased, all synchronisation ceases to exist at a certain value of c. Since the analysed system equations Eq. (5.4) of the pendulum picture are not equivalent, with respect to the asymmetry term, to the system equations of the cardiomyocyte picture (Eq. (5.11)), this results cannot be interpreted directly in context of synchronisation behaviour of premature cardiomyocytes.

5.2.3. Synchronisation with symmetric nonlinear restoring force

In the previous section, the synchronisation behaviour of two viscoelastically coupled self-sustained oscillators was studied with the focus on their nonlinear and asymmetric restoring force. The asymmetry was introduced by perturbing the formerly linear restoring force by an exponential term Eq. (5.2). In this section it is analysed how a nonlinear but symmetric restoring force affects in general the synchronisation behaviour of self-sustained oscillators. For this purpose a system Eq. (5.4) with a symmetric but nonlinear restoring force ($c = 0$, $b \geq 0$) is studied: two viscoelastically coupled Van der

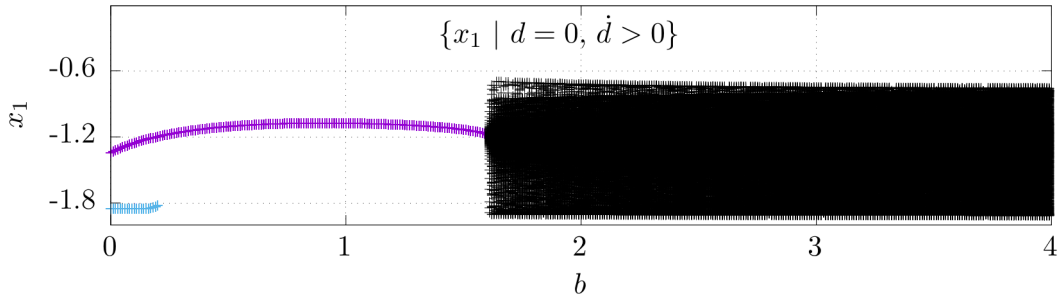

(a) Bifurcation diagram created via plotting the elongation of the first oscillator x_1 of the Poincaré map.

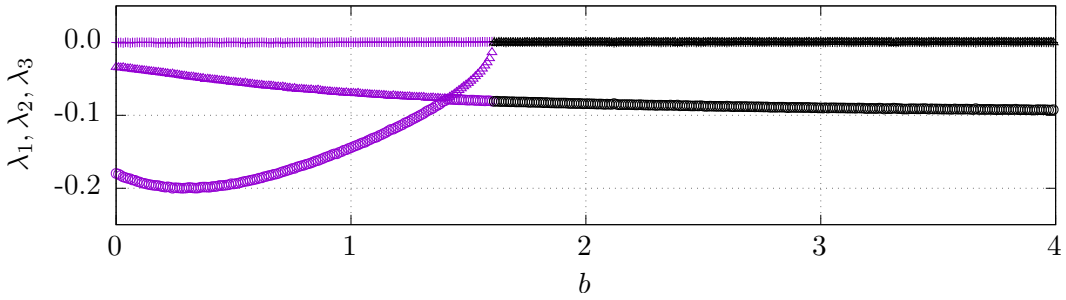

(b) The three largest Lyapunov exponents λ_1, λ_2, λ_3 of the system Eq. (5.4).

Figure 5.17.: Lyapunov exponents and bifurcation diagram of two coupled Van der Pol-Duffing oscillators. The colours indicate the type of solution. Blue: in-phase orbit, purple: anti-phase orbit, and black: no 1:1 phase locking.

Pol Duffing oscillators.

For analysing how the symmetric but nonlinear restoring force influences the dynamics of the coupled oscillators a bifurcation diagram based on a Poincaré map and the three largest Lyapunov exponents were calculated and are shown in Figure 5.17. In the case of a linear restoring force ($b = 0$) the two coexisting periodic orbits correspond to the in- (purple) and anti-phase (blue) synchronisation states can be seen. As the strength of the nonlinearity in the restoring force increases ($b > 0$), the orbits remain until a critical value $b \approx 0.2$ is reached. At this point the anti-phase solution vanishes. The in-phase solution remains until another critical point $b \approx 1.6$ is reached at which the in-phase solution vanishes, too. After this point, no 1:1 synchronous state is found to be stable anymore. This was checked by calculating the Poincaré map and the Lyapunov exponents up to $b = 20$. Furthermore, no other coexisting attractors were found by varying the initial condition at different values of b.

Figure 5.18 shows the largest two Lyapunov exponents of the system in the γ-b-parameter space. It can be seen that the described behaviour does not depend qualitatively but quantitatively on the viscous coupling parameter γ. The second critical value of b, after which no synchronised solution exists (blue area), increases with γ.

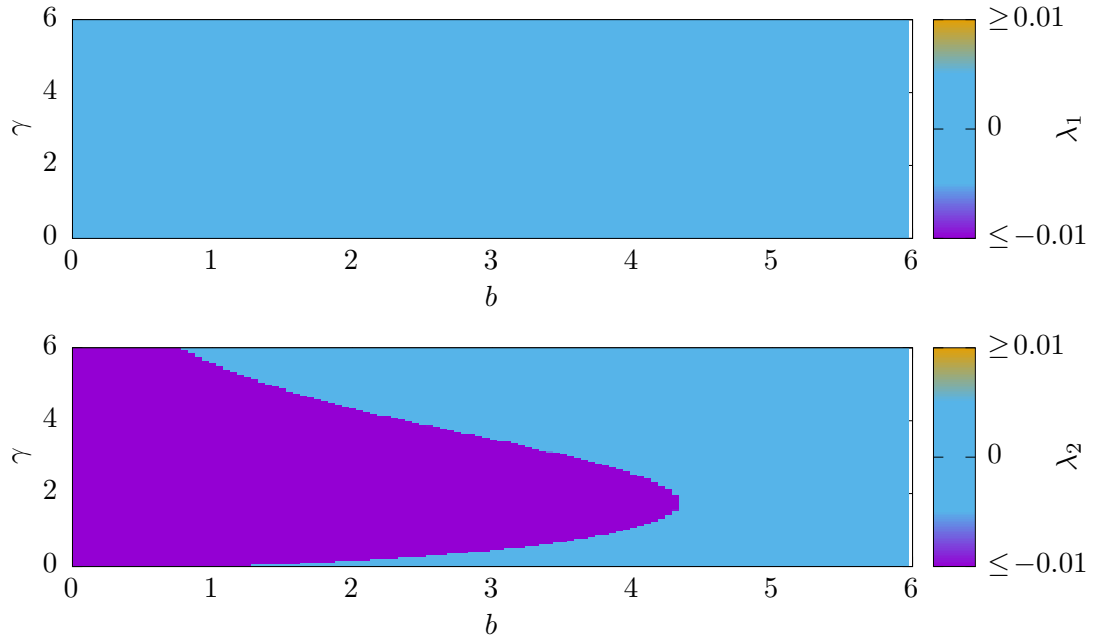

Figure 5.18.: Two largest Lyapunov exponents λ_1 and λ_2 showing a parameter regime in which the symmetric system $|c| = 0$ exhibits a synchronised dynamics ($\lambda_2 < 0$). Important to note: For vanishing viscous coupling parameter γ an additional Lyapunov exponent is equal to zero since $\dot{d} = 0$.

Thus a high fluidity seems to have a stabilizing effect. If γ becomes to large, this effect diminishes, since a very high fluidity effectively decreases the coupling strength between the two oscillators. In contrast to the results obtained when analysing the asymmetric nonlinear restoring force ($|c| \neq 0$, $b = 0$), the regime where neither the in-phase nor the anti-phase orbit exists is not chaotic, as the Lyapunov exponents (Figure 5.17b) indicate. Furthermore, there is no new in-phase orbit to be found as the parameter controlling the strength of the nonlinear part in the restoring force increases. Another difference is that the anti-phase orbit vanishes way before the in-phase orbit does.

In summary, it was found that the in-phase synchronisation state is favoured by a nonlinearity b in the restoring force. This can be explained by recalling again that the frequency and the oscillation form of the anti-phase synchronisation state is dominated by the elastic spring in the coupling. This spring enforces the oscillation frequency of the anti-phase state (see Figure 5.12). The strength of the nonlinearity of the restoring force b (Eq. (5.3)) introduces an additional time scale competing with the oscillation time scale enforced by the elastic coupling ω_c. If the mismatch is high enough, the anti-phase state ceases to exist. In the in-phase synchronisation state however, the oscillators are allowed to oscillate with the frequencies defined by their inner properties: ω_i and b (Eq. (5.4)). Thus a higher value of b does not negatively affect the in-phase synchronisation state as fast as the anti-phase synchronisation state. But since a higher value of b effectively increases the frequency shift between the oscillators and since the effective coupling strength was kept constant, even the in-phase orbit stops to exist at a certain value of b; because for a certain frequency shift there needs to be a certain minimal coupling strength for synchronisation to occur. These results can be interpreted in context of the synchronisation of premature cardiomyocytes by switching into the cardiomyocyte picture. Here, the anti-phase state becomes the in-phase-cmc state. On the first glance, the obtained results seem to suggest that rather non-sinusoidal oscillations, which are exhibited by cardiomyocytes, frustrate the in-phase-cmc synchronisation of these. However, this is not true. The reason for that might be again the inner excitation-contract coupling (Sec. 2.1) which prevents, due to its temporal refractoriness, cardiomyocytes to feature the frequencies of the in-phase-cmc state. Thus the above reason for the anti-phase state (or the in-phase-cmc) to cease at nonlinear oscillations, is not valid in case of premature cardiomyocytes. Thus, the biological system is able to synchronise in-phase in the presence of non-sinusoidal oscillations.

5.3. Summary

The aim of this chapter was to analyse how the synchronisation behaviour of self-sustained oscillators depends on the viscoelastic properties of their coupling. This study was motivated by premature cardiomyocytes which are able to synchronise with each other if they are coupled mechanically via the viscoelastic extracellular matrix surrounding them [13]. Premature cardiomyocyte exhibit self-sustained and asymmetric beating behaviour (Chap. 3). Thus a simple self-sustained oscillator, the Van der Pol oscillator was chosen as mathematical system and its restoring force was modified for him to ex-

hibit asymmetric oscillations as well. In this context, the asymmetry parameter c was introduced. To understand how the viscoelastic properties of the medium, coupling the cardiomyocytes, influences their synchronisation behaviour, it has to be understood how a viscoelastic coupling influences the synchronisation of self-sustained oscillators in general. Thus, two modified Van der Pol oscillators were coupled with a simple viscoelastic system: the Maxwell fluid. The simplicity of this model makes it possible to understand and study its viscoelastic behaviour in terms of only two parameters: its elastic coupling parameter ω_c and its viscous coupling parameter γ. Two modified Van der Pol oscillators were coupled via the Maxwell fluid and they were found to synchronise in-phase as well as anti-phase. The stability of these two synchronisation states was analysed by means of the viscoelastic coupling parameters and the asymmetry of the exhibited oscillations. It was found that the in-phase synchronisation state is favoured by both a more fluid coupling (high γ) and more asymmetric oscillations (high c). Furthermore, it was found that the properties, in terms of oscillation form and frequency, of the in-phase state are determined by the properties of the coupled components. However, the properties, in particular the frequency, of the anti-phase synchronisation state are mostly determined by the linear elastic spring and its spring constant ω_c^2.

The results were obtained in general for the used self-sustained oscillators which where coupled like in the pendulum picture (Figure 5.5a). To interpret these in context of the synchronisation of premature cardiomyocytes, it was necessary to introduce the cardiomyocyte coupling picture (Figure 5.5b). By switching from the pendulum picture to the cardiomyocyte picture, the synchronisation states swap their meaning. The in-phase and anti-phase synchronisation states of the pendulum picture become the anti-phase-cmc and in-phase-cmc synchronisation state in the cardiomyocyte picture, respectively.

With this in mind, it can be better understood why premature cardiomyocytes may only synchronise in-phase if the extracellular matrix reaches a certain stiffness. The medium in which they are embedded is more fluid in the beginning but becomes more elastic and viscose over time [21, 22, 18, 15, 78, 19]. Figure 5.10 suggest a synchronisation boundary the medium has to overcome in this way for the in-phase-cmc synchronisation state to be stable. Because of the temporal refractoriness of their inner excitation-contraction coupling (Sec. 2.1), cardiomyocytes can only feature certain beating frequencies. The frequency of the in-phase-cmc state, however, is not bound and determined by the elastic coupling parameter ω_c. This suggests a optimal elasticity of the extracellular matrix for the cardiomyocytes to synchronise in-phase. Namely, the very elasticity at which the frequency of the in-phase-cmc state can be featured by the premature cardiomyocytes.

Even though these results are very interesting, there are certain limitations caused by the chosen model. First, the Maxwell fluid does not model the viscoelastic properties of polymer gels in general. Usually, those complex compounds cannot be described without tremendous mathematical effort in terms of *Prony series* and *fractional derivatives* [20, 25, 26]. On the other hand, the parameters of those models often cannot be interpreted in a straightforward way. Thus, it might be a good idea to avoid those for generating a first qualitative understanding and return to them as soon as quantitative results are sought. Second, the inner properties of the premature cardiomyocytes were neglected in this

study. Until today it is an open question how the mechanosensing of cardiomyocytes works. Furthermore, it is unknown how synchronisation is made possible by changes of their inner biological structure. It is known however that once cardiomyocytes are synchronised, they maintain the beating frequency of the synchronised state for a long period of time[10] after the coupling between them has ceased [13]. This effect of a sustained shift in natural frequency cannot be modelled by the simple self-sustained oscillator used. Thus, the presented results may not explain how the synchronised state is maintained by a system of cardiomyocytes but may enlighten the way towards it. Furthermore, its was found that the excitation-contraction coupling, which makes the cardiomyocyte contract, may be a very important feature to consider if one tries to model their synchronisation behaviour. Thus, later studies which try to mathematical model a system of synchronising cardiomyocytes, may want to incorporate the features of an excitable system, which can show temporal refractoriness, into the equations representing the cardiomyocytes.

Considering the analysed mathematical model Eq. (5.4) as a pure dynamical system, the obtained results are interesting in two other contexts. First, in the context of distributed time delay coupling. As already said, effects like amplitude death [63, 69] and the synchronisation of networks of self-sustained oscillators [38, 70], to only name a few, have been studied in systems comprising distributed time delay coupling. Since the viscoelastic coupling chosen in this thesis can be interpreted as distributed time delay coupling as well Eq. (5.12), the present study enqueues itself in this interesting field of research. It was shown that the memory γ^{-1} of the distributed time delay coupling, comprising an exponential integral kernel, determines which synchronised solutions are found to be stable. A short memory favours in-phase synchronisation while, in case of a long memory, in- and anti-phase synchronisation states coexist.

Second, in the context of in- and anti-phase synchronisation of two-oscillator systems in general. Throughout literature many systems are found to synchronise in-phase and/or anti-phase. But there is a distinct branch of studies which is focused on the very root of synchronisation research, namely, on Huygens' experiment of two coupled pendulum clocks. Many studies have tried to reproduce his observations mathematically and experimentally [71, 42, 43]. The question which properties a physical system needs to possess to exhibit either in- or anti-phase synchronisation is subject of recent studies [43]. By analysing how the synchronisation behaviour of two self-sustained oscillators depends on the viscoelastic properties of their coupling, a little more light was shed in the field of synchronisation research.

[10] More than a hundred oscillations.

6. Conclusion

In this thesis it was analysed how the synchronisation behaviour of self-sustained oscillators is influenced by the viscoelastic properties of their coupling. This question was motivated by the early development stage of artificial heart tissue in which the synchronisation of beating premature cardiomyocytes is aided by the viscoelastic polymer gel surrounding them. To tackle this task, a mathematical model was developed which comprises two asymmetric oscillating Van der Pol oscillators which were coupled with a Maxwell model (Chap. 5).

They were found to synchronise in-phase as well as anti-phase. The stability of these two synchronisation states was analysed by means of the viscoelastic coupling parameters (Sec. 5.2.1) and the asymmetry of the exhibited oscillations (Sec. 5.2.2 and Sec. 5.2.3). It was found that the in-phase synchronisation state is favoured by both a more fluid coupling and more asymmetric oscillations. Furthermore, it was found that the oscillation form and frequency of the in-phase state are determined by the properties of the coupled oscillators. The properties, in particular the frequency, of the anti-phase synchronisation state however, are mostly determined by the linear elastic spring of the coupling and its spring constant. These results were related to the synchronisation behaviour of premature cardiomyocytes. It was shown that the mathematical model system suggests both a stiffness boundary which the viscoelastic properties of the extracellular matrix have to overcome and an optimal elasticity of the extracellular matrix for the premature cardiomyocytes to synchronise in-phase (Sec. 5.2.1). These results are interesting in two contexts: first, in the context of bioengineering and second, in the context of the branch of nonlinear dynamics, in which networks of coupled oscillators are studied.

Furthermore, first experimental insights were provided and analysed which characterise the model system – the premature state of the engineered heart muscle (Sec. 2.2). Videos of beating premature cardiomyocytes have been studied to extract the following features of their beating behaviour: frequency, oscillation form, and scale of contraction (Chap. 3). It was found that the analysed premature cardiomyocytes have a mean beating frequency of $\langle f \rangle = 0.73\,(\pm 0.03)\,\mathrm{Hz}$, feature asymmetric oscillations in terms of a peak and recover phase, and that their exerted maximum strain is $\varepsilon_0 = 5(\pm 2)\%$ on average (Sec. 3.3). A video and signal analysis procedure was developed to extract those quantities (Sec. 3.2) and periodic orbits representing the beating behaviour of premature cardiomyocytes in phase space were generated.

Rheological experiments have been conducted as well, to access the viscoelastic properties of the medium surrounding the premature cardiomyocytes (Chap. 4). It was shown how the extracellular matrix becomes stiffer over time during the polymerisation of the comprised collagen I and the stress response of the extracellular matrix to a sinusoidal

strain stimulus was analysed in a regime which covers the maximum strain the premature cardiomyocytes exhibit on average (Sec. 4.2). These findings have been used to relate the parameters of the Maxwell model to experimental quantities over time (Sec. 4.3).

The analysis of the presented mathematical model uncovered a limitation which in subsequent studies should be to avoided. Premature cardiomyocytes beat in consequence of inner calcium oscillations in context of the so called excitation-contraction coupling (Sec. 2.1). Thus, they posses properties of excitable systems like refractoriness, which turned out to be an important feature in context of their mechanically driven synchronisation. Simple limit cycle oscillators do not feature refractoriness. Thus, they are only applicable as a mathematical model for cardiomyocytes to a limited extent.

Furthermore, the extracellular matrix is not only composed of collagen but of fibroblasts, which stiffen the medium as well (Sec. 2.2). This further stiffening may lead to a stress response of the extracellular matrix that is more nonlinear than considered in this thesis. Since a linear model was chosen here, it remains an open question how this nonlinear stress response might influence the synchronisation behaviour of premature cardiomyocytes. Thus, viscoelastic models which feature nonlinear stress responses should be considered in subsequent studies.

To conclude, this thesis provided first experimental insights into the beating behaviour of premature cardiomyocytes found in the biological engineered heart muscle system and into the rheological properties of the extracellular matrix. In addition, a mathematical model of viscoelastically coupled self-sustained oscillators was developed and it was analysed how their synchronisation behaviour depends on the viscoelastic properties of their coupling. The results provide first insights into the mechanically driven synchronisation mechanism of premature cardiomyocytes and enqueue themselves into the broad field of research in which networks of coupled oscillations are studied. Last but not least, this thesis paves the way for subsequent studies dealing with both, the mathematical modelling of the synchronisation behaviour of premature cardiomyocytes in the context of the engineered heart muscle system and the synchronisation of viscoelastically coupled self-sustained oscillators.

A. Additional Figures

A.1. Pictures of the analysed premature cardiomyocytes

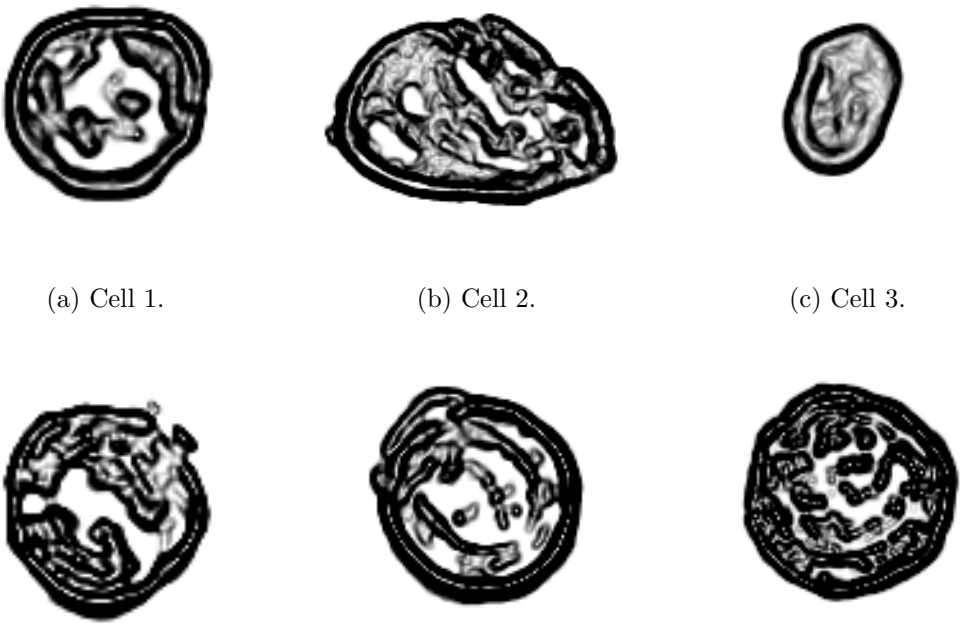

(a) Cell 1. (b) Cell 2. (c) Cell 3.

(d) Cell 4. (e) Cell 5. (f) Cell 6.

Figure A.1.: All the six cells whose beating behaviour was analysed are shown here.

A.2. Good vs. poor cell beating signals

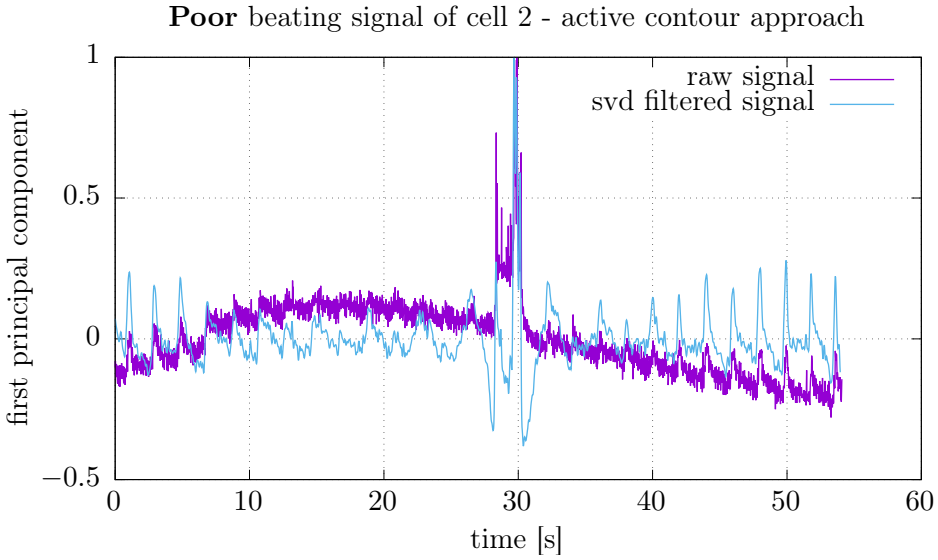

(a) Poor beating signal generated with the active contour approach. There are no clear pronounced peaks indicating the beating events. The dominant frequency is 0.278 Hz, which is far less then the beating frequency determined by eye: 0.51 (±0.02) Hz.

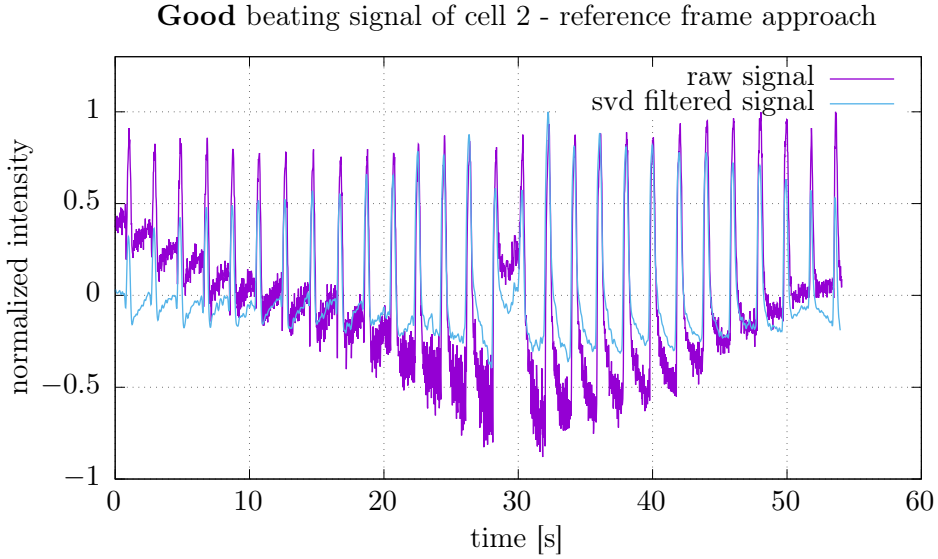

(b) Good beating signal generated with the reference frame approach. There are clear pronounced peaks indicating the beating events. The dominant frequency is 0.52 (±0.02) Hz, which is almost equal to the beating frequency determined by eye: 0.51 (±0.02) Hz.

Figure A.2.: Comparison of a good and a poor beating signal, generate with two different approaches from the video data of cell two.

A.3. All cell beating signals

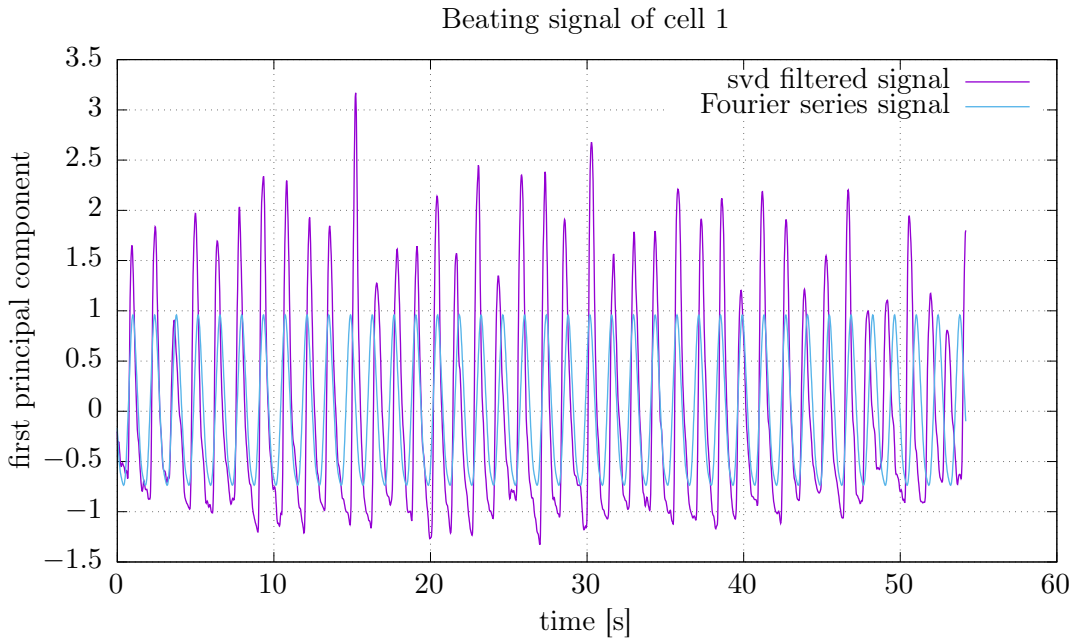

Figure A.3.: Beating signal of cell 1 generated with the active contour approach. Shown is the svd filtered signal and the signal generated with the corresponding Fourier series.

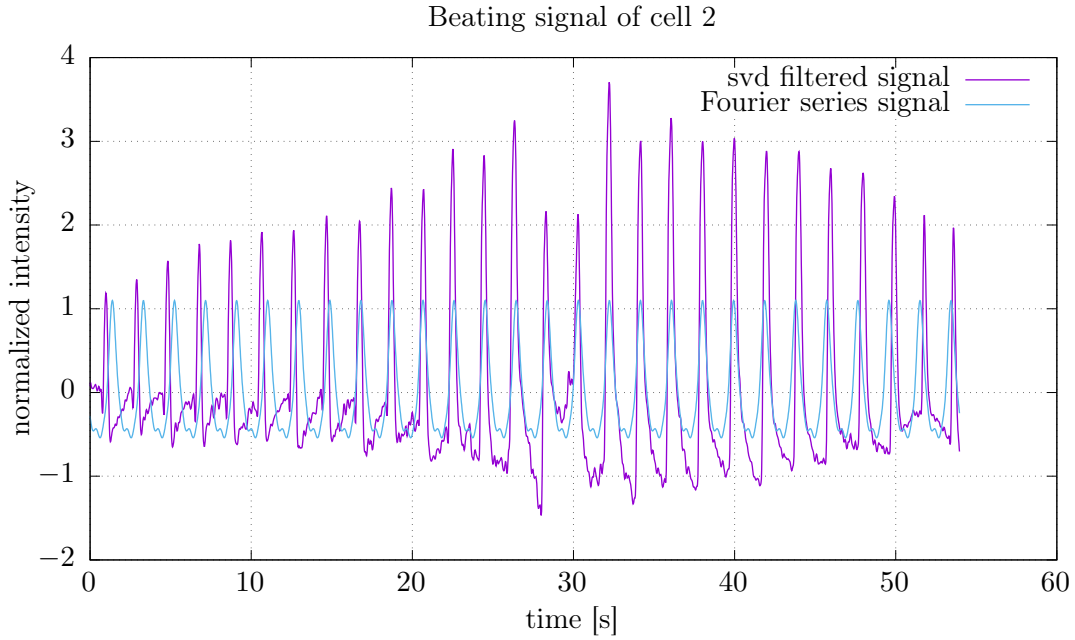

Figure A.4.: Beating signal of cell 2 generated with the reference frame approach. Shown is the svd filtered signal and the signal generated with the corresponding Fourier series.

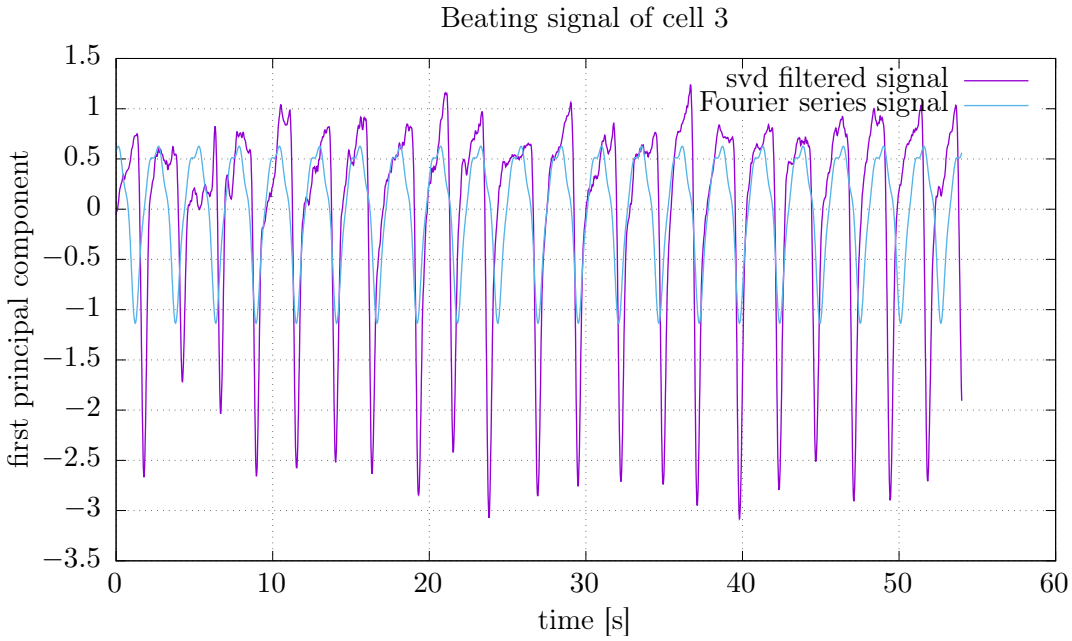

Figure A.5.: Beating signal of cell 3 generated with the active contour approach. Shown is the svd filtered signal and the signal generated with the corresponding Fourier series.

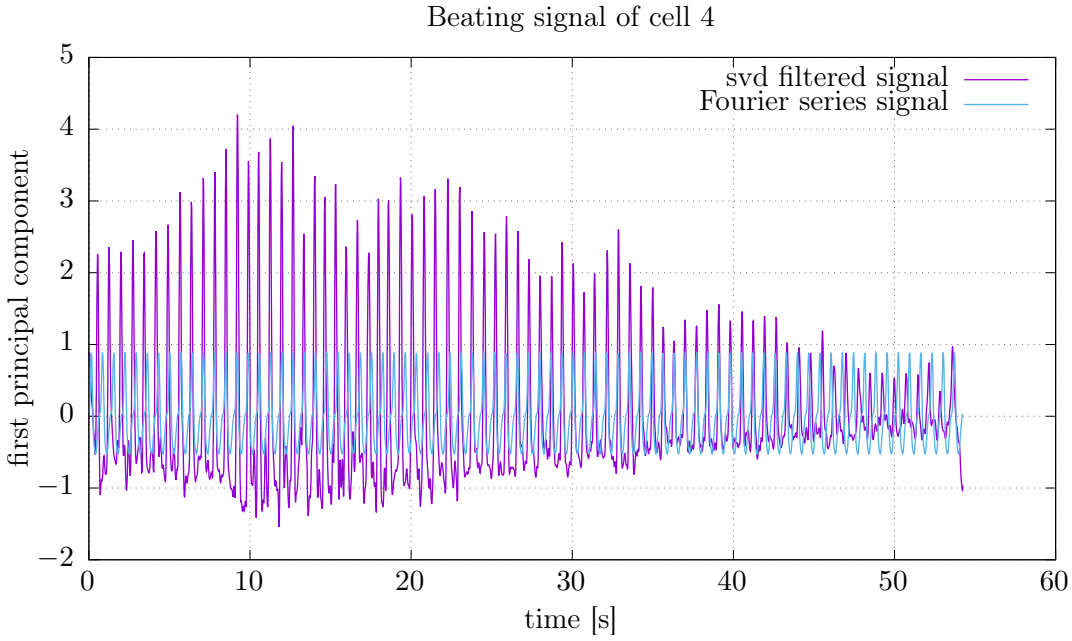

Figure A.6.: Beating signal of cell 4 generated with the active contour approach. Shown is the svd filtered signal and the signal generated with the corresponding Fourier series.

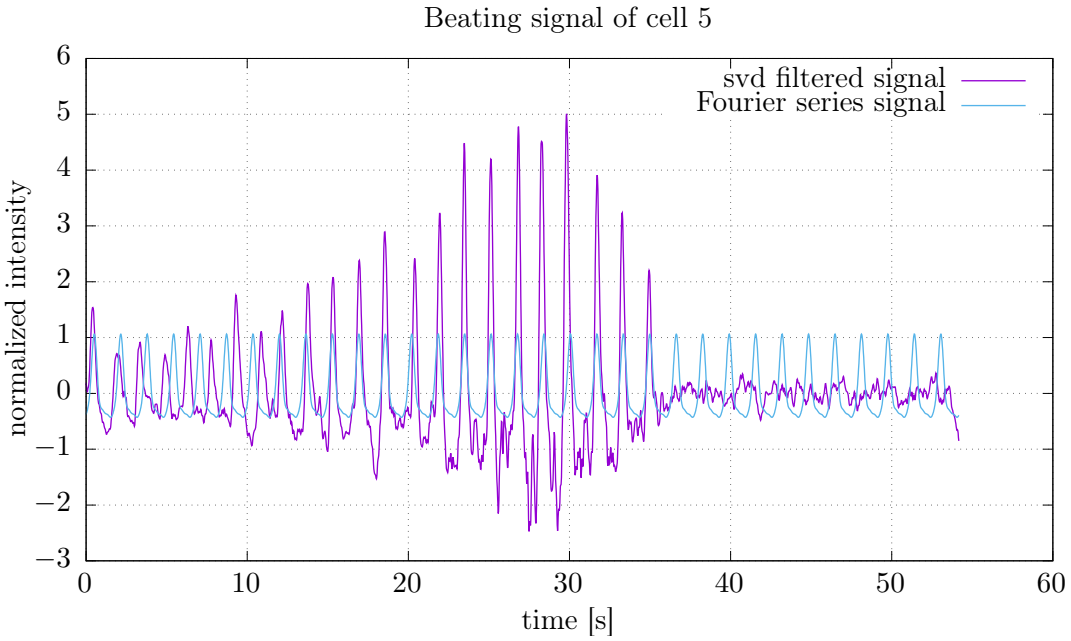

Figure A.7.: Beating signal of cell 5 generated with the reference frame approach. Shown is the svd filtered signal and the signal generated with the corresponding Fourier series.

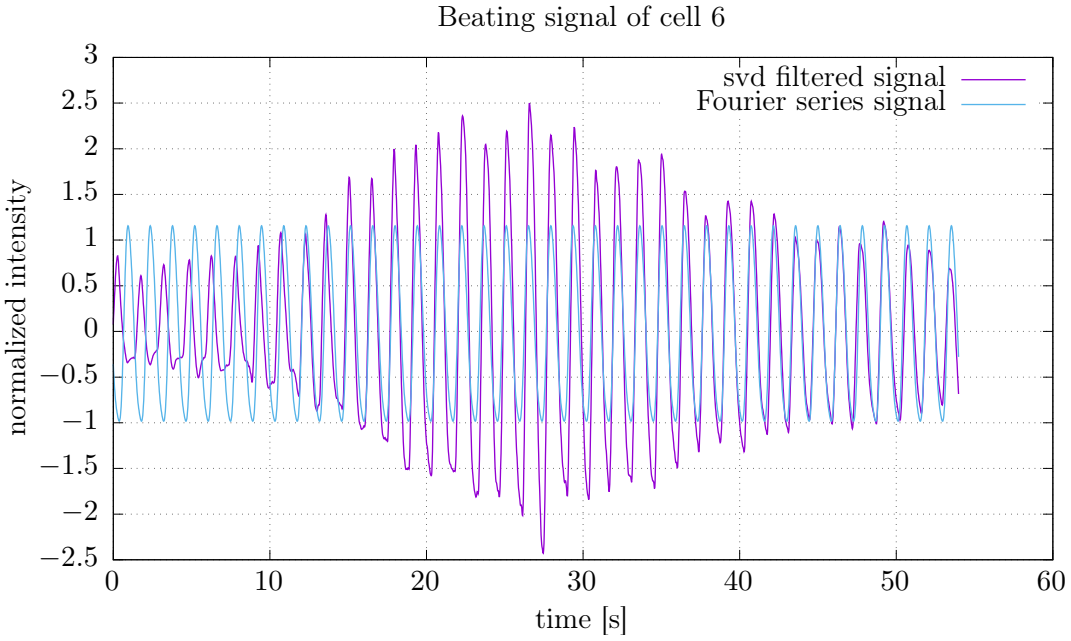

Figure A.8.: Beating signal of cell 6 generated with the reference frame approach. Shown is the svd filtered signal and the signal generated with the corresponding Fourier series.

A.4. Spectra of cell beating signals

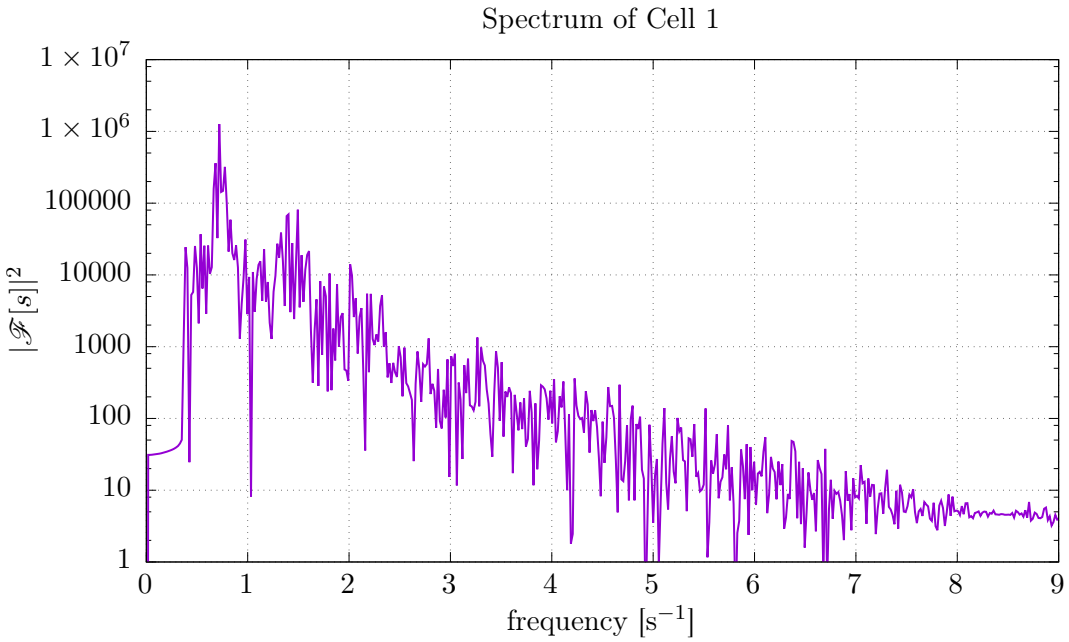

Figure A.9.: Frequency spectrum of the svd filtered signal of cell 1, generated with the active contour approach.

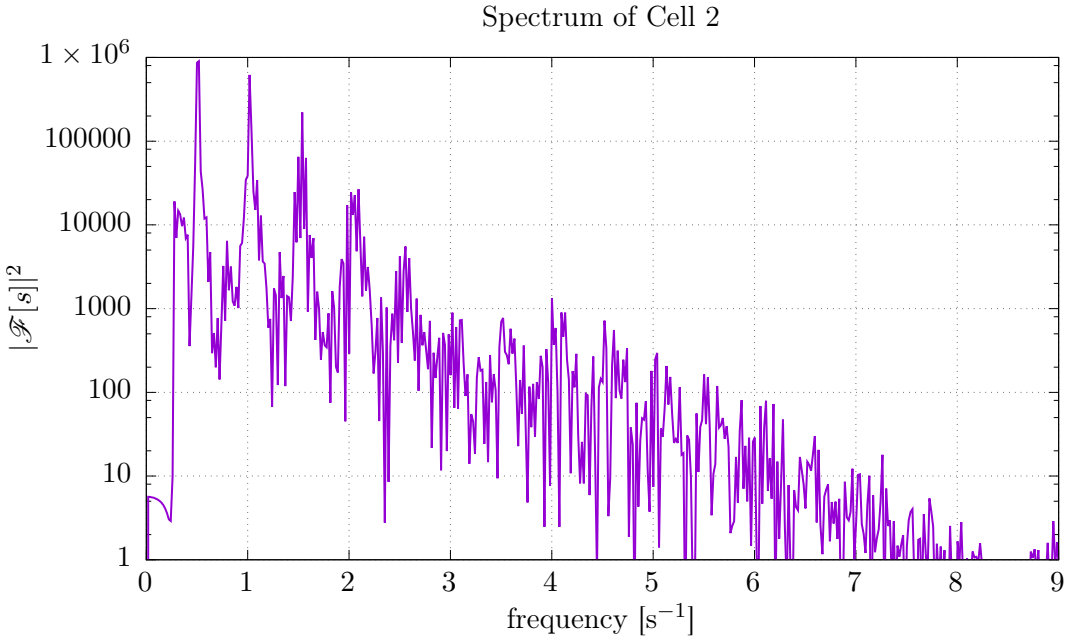

Figure A.10.: Frequency spectrum of the svd filtered signal of cell 2, generated with the reference frame approach.

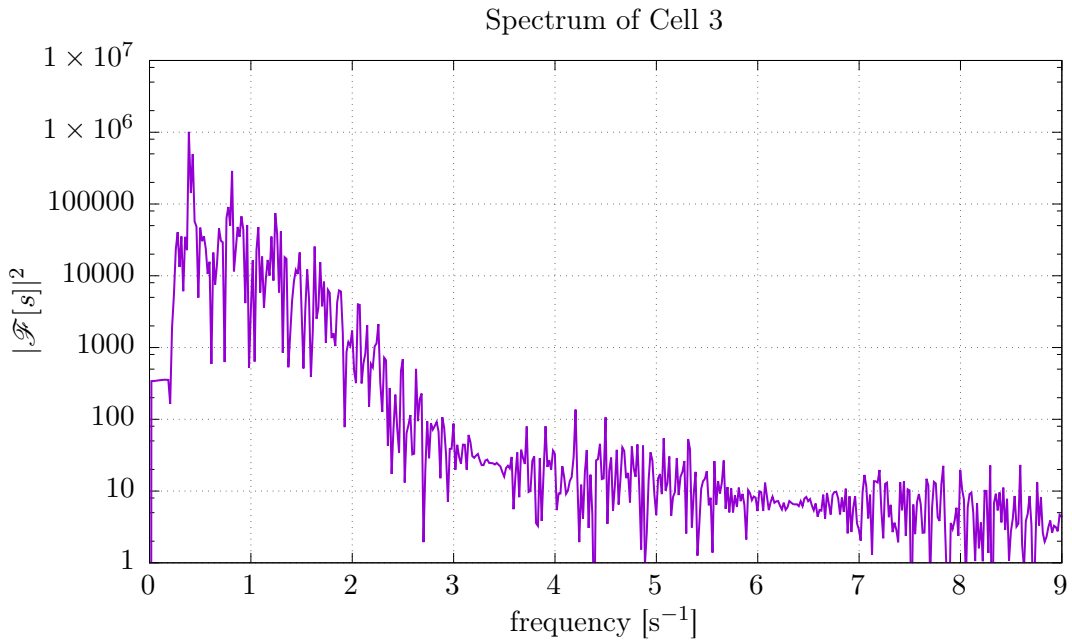

Figure A.11.: Frequency spectrum of the svd filtered signal of cell 3, generated with the active contour approach.

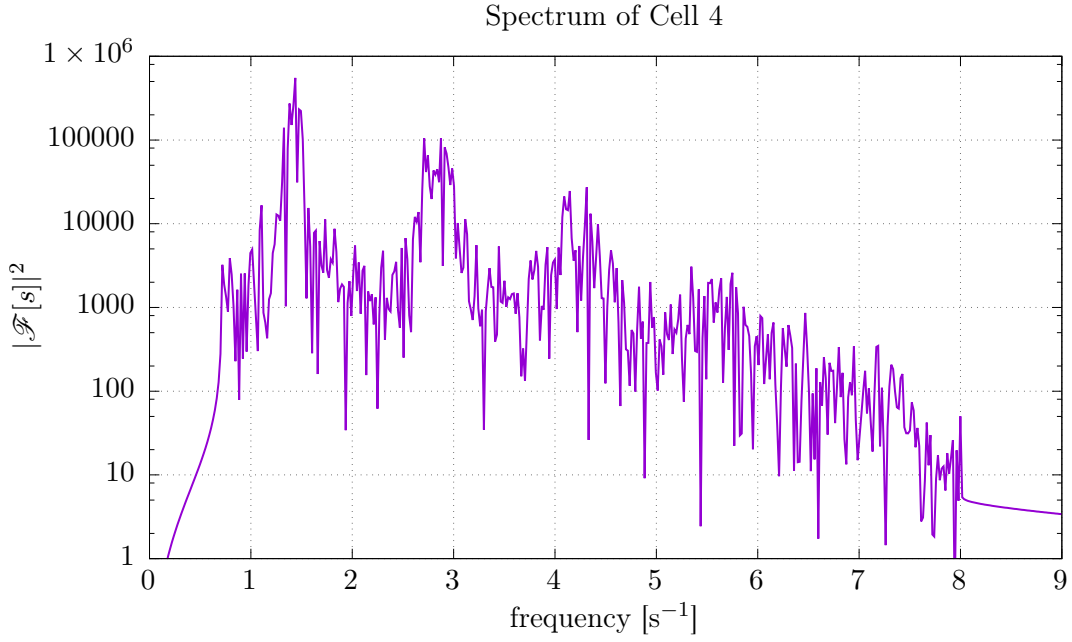

Figure A.12.: Frequency spectrum of the svd filtered signal of cell 4, generated with the active contour approach.

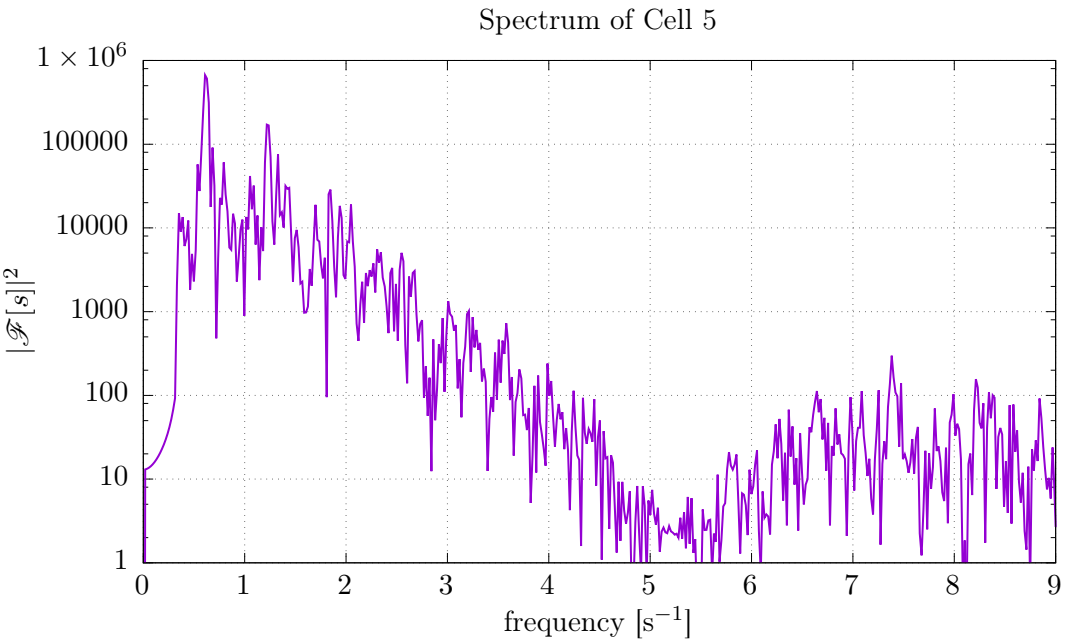

Figure A.13.: Frequency spectrum of the svd filtered signal of cell 5, generated with the reference frame approach.

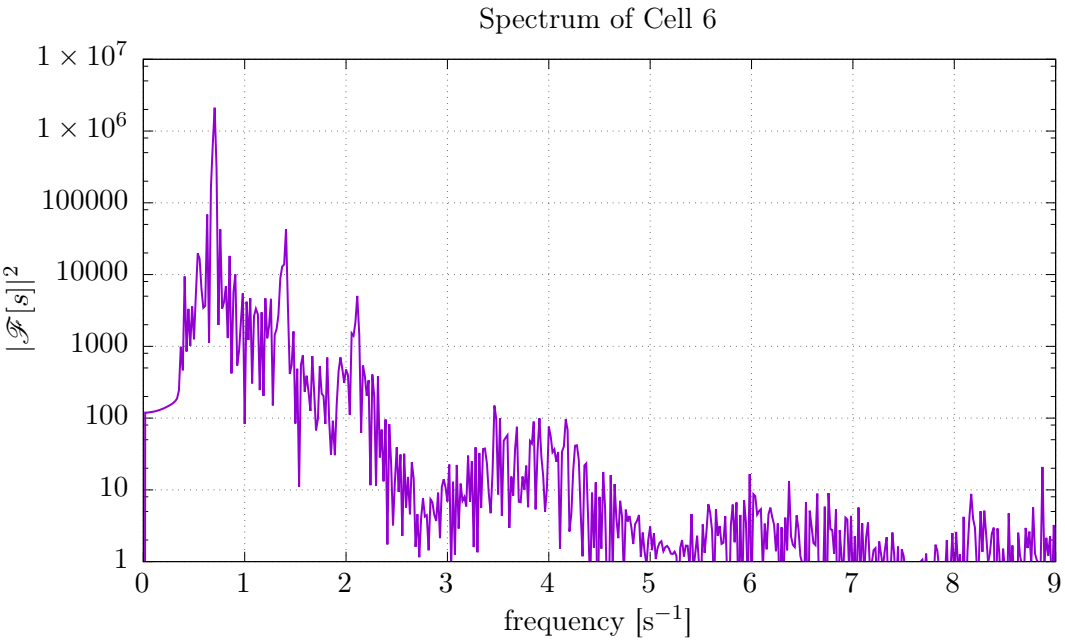

Figure A.14.: Frequency spectrum of the svd filtered signal of cell 6, generated with the reference frame approach.

A.5. Frequency map of the in-phase synchronisation states

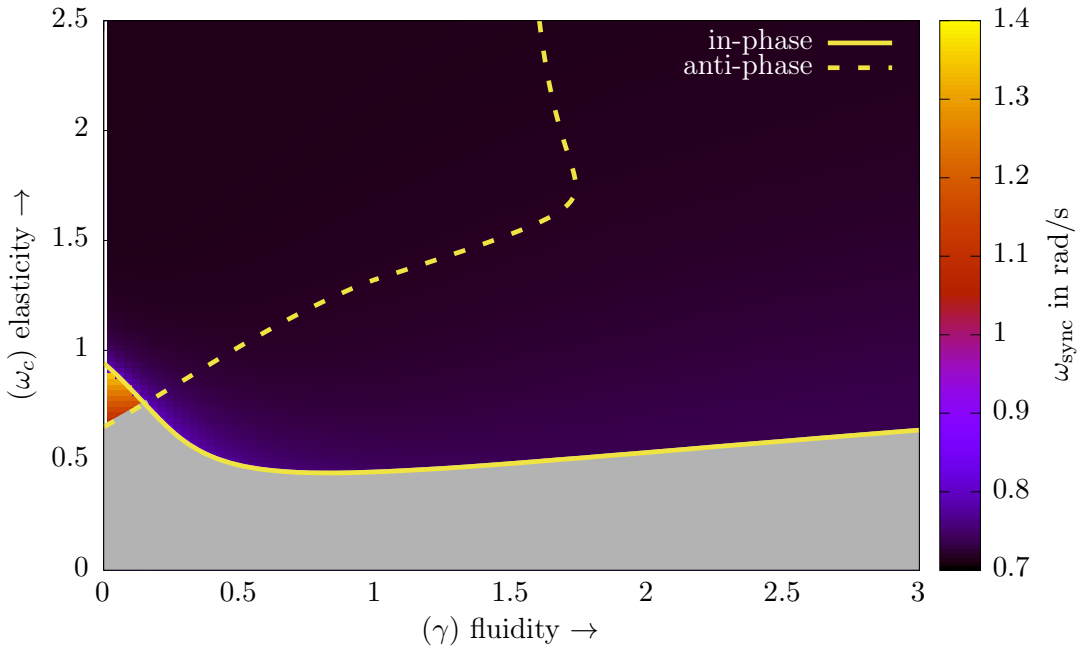

Figure A.15.: Map in parameter space showing the colour coded frequency of the in-phase synchronisation state in dependence of the elastic ω_c and viscous γ coupling parameter. Above the bifurcation curves (yellow lines), the corresponding synchronisation state exists (see Figure 5.9). In case of two coexisting synchronisation states, the initial conditions determine which state is reached. Here, initial condition favouring the in-phase state are chosen. In the absence of synchronisation (below both yellow lines), no meaningful frequency can be determined. See the other frequency maps in Figure 5.11 for comparison.

A.6. Oscillation form of in- and anti-phase state

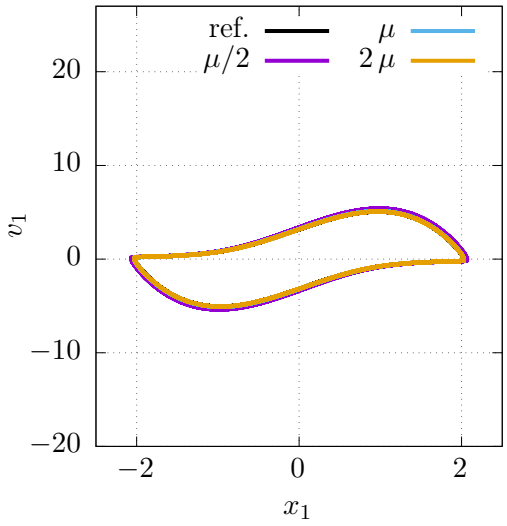

(a) In-phase orbits vs. the reference orbit.

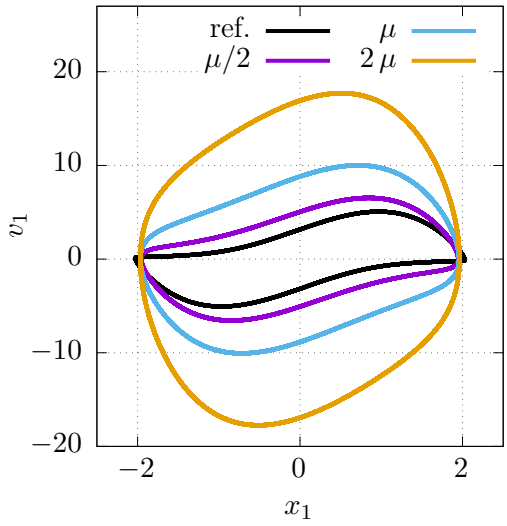

(b) Anti-phase orbits vs. the reference orbit.

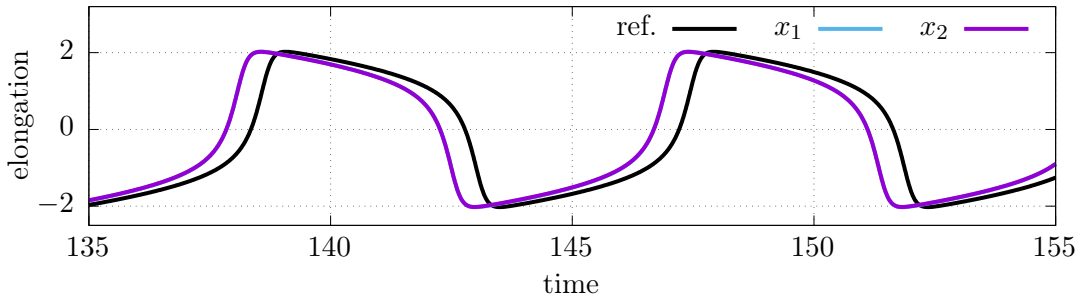

(c) In-phase synchronised oscillations with $\omega_c = 2\,\mu$ vs. the reference oscillation. Due to the strong elastic coupling, the elongation of the coupled oscillators x_1 and x_2 do not significantly differ from each other.

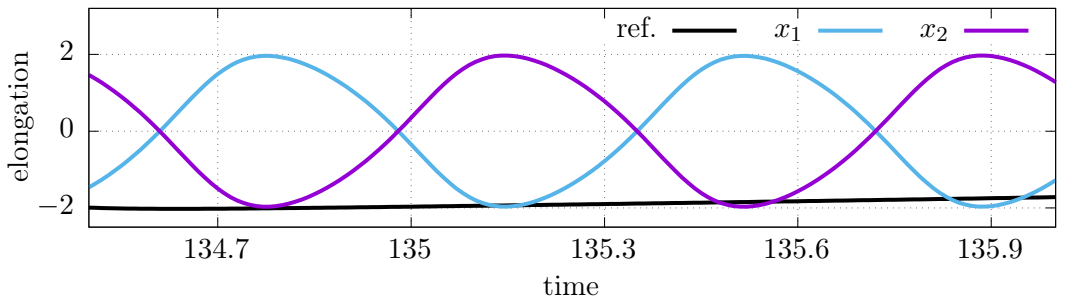

(d) Anti-phase synchronised oscillations with $\omega_c = 2\,\mu$ vs. the reference oscillation.

Figure A.16.: Comparison of the orbit and oscillation form of the in- and anti-phase synchronisation states with the oscillation of an single oscillator ($\omega = 1$, $\mu = 3$) denoted by *ref.* In case of the orbit comparison, different values for the elastic coupling parameter are chosen: $\omega_c \in \{\mu/2, \mu, 2\,\mu\}$. Note that although the in-phase state is very similar to the reference oscillator for every chosen elastic coupling strength, the anti-phase state differs a lot with respect to both, oscillation form and frequency.

A.7. Lissajous figures from raw experimental data

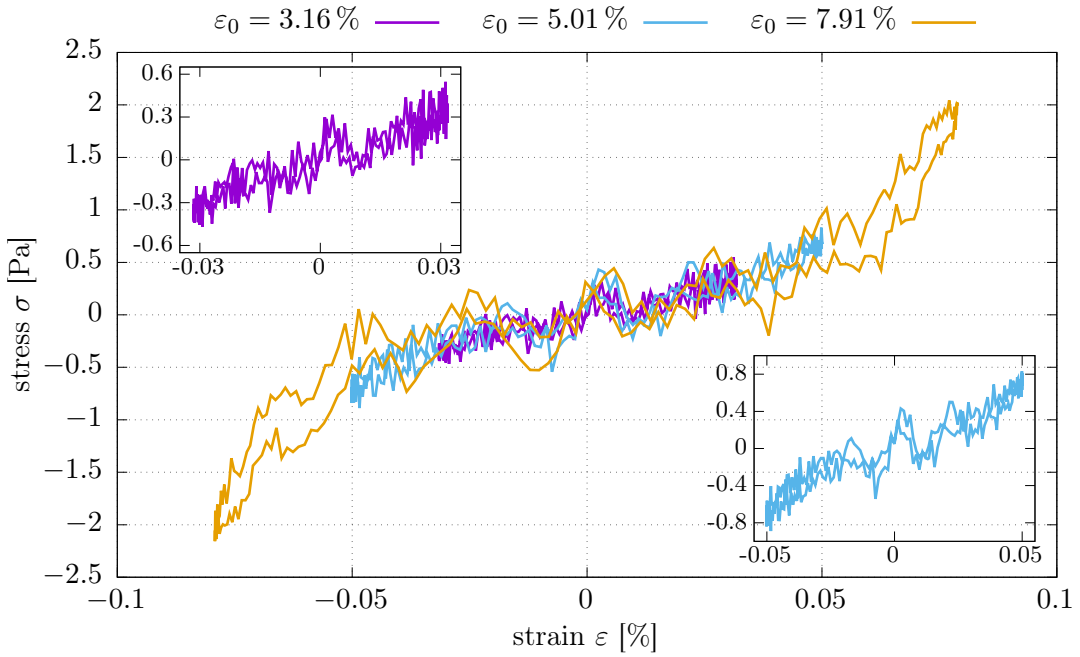

Figure A.17.: Lissajous figures at different maximum strains ε_0 showing a linear stress response at lower maximum strain $\varepsilon_0 = 3.16\,\%$ and strain stiffening at higher maximum strain $\varepsilon_0 = 7.91\,\%$. Lissajous figures based on Fourier fits are shown in Figure 4.4. The shear frequency is $f = 1\,\mathrm{Hz}$.

B. Additional Calculations

B.1. Equivalence of Relaxance and Retardance

To show that the relaxance $Q(t)$ and the retardance $U(t)$ can be inferred from each other Eq. (2.7) shall be reconsidered. This equation states that their convolution is identical to the Dirac-delta-function.

$$\int_0^\infty Q(t-u)\,U(u)\,\mathrm{d}u = Q(t) * U(t) = \delta(t) \tag{B.1}$$

Since convolutions in the time domain are mere multiplications in Laplace[1] space

$$\mathscr{L}[f(t) * g(t)](s) = \bar{f}(s) \cdot \bar{g}(s), \tag{B.2}$$

Laplace transforming[2] equation Eq. (B.1) yields an algebraic equation, which can be solved for $\bar{Q}(s)$ or $\bar{U}(s)$.

$$\bar{Q}(s) \cdot \bar{U}(s) = 1 \tag{B.3a}$$

$$\Leftrightarrow \bar{Q}(s) = \frac{1}{\bar{U}(s)} \tag{B.3b}$$

$$\Leftrightarrow \bar{U}(s) = \frac{1}{\bar{Q}(s)} \tag{B.3c}$$

Transforming Eq. (B.3b) and Eq. (B.3c) back into the time domain yields the relaxance and the retardance respectively.

$$Q(t) = \mathscr{L}^{-1}\left[\frac{1}{\bar{U}(s)}\right](t) \tag{B.4a}$$

$$U(t) = \mathscr{L}^{-1}\left[\frac{1}{\bar{Q}(s)}\right](t) \tag{B.4b}$$

Note that the inverse Laplace transform is defined as an integral over a contour enclosing the poles of the transformed function.

$$\mathscr{L}^{-1}\left[\bar{f}(s)\right](t) = f(t) = \frac{1}{2\,\pi\,i}\oint \bar{f}(s)\exp(s\,t)\,\mathrm{d}s \tag{B.5}$$

Thus Eq. (B.4a) and Eq. (B.4b) are well defined even if $\bar{U}(s)$ and $\bar{Q}(s)$ feature complex roots.

[1] The Laplace transform is defined as: $\mathscr{L}[f(t)](s) = \bar{f}(s) = \int_0^\infty f(t)\exp(-s\,t)\,\mathrm{d}t$ with $s \in \mathbb{C}$.

[2] The Laplace transform is chosen over the Fourier transform since $Q(t)$ and $U(t)$ are only defined for positive time.

B.2. Solving Eq. (5.4c) with Green's function approach

Solving Eq. (5.4c) with Green's function approach. Consider the following linear and ordinary differential equation (ode) with time dependent inhomogeneity $\phi(t)$:

$$L \circ f(t) = \phi(t). \tag{B.6}$$

Here L denotes the linear differential operator acting on the sought function $f(t)$. $\phi(t)$ can be understood as the response of the differential operator L to the input function $f(t)$. A Green's function $G(t)$ is defined as the function which leads to a single impulse response, denoted by the delta distribution $\delta(t)$.

$$L \circ G(t) = \delta(t) \tag{B.7}$$

For obtaining a fundamental solution $\tilde{f}(t)$ of the inhomogeneous ode system Eq. (B.6), Eq. (B.7) can be applied in the following way:

$$L \circ \tilde{f}(t) = \phi(t) = \delta(t) * \phi(t) = [L \circ G(t)] * \phi(t) = L \circ [G(t) * \phi(t)] \tag{B.8a}$$

$$\Rightarrow \tilde{f}(t) = G(t) * \phi(t). \tag{B.8b}$$

Here $*$ is the convolution operator. The general solution $f(t)$ of Eq. (B.6) is given by the sum of the general solution $f_h(t)$ of the homogeneous system (Eq. (B.6) with $\phi(t) \equiv 0$) and one fundamental solution $\tilde{f}(t)$ of the inhomogeneous system.

$$f(t) = f_h(t) + \tilde{f}(t) \tag{B.9}$$

The advantage of the Green's function approach is that the Green's function can be found by applying the Fourier transform[3] to Eq. (B.7).

$$\mathscr{F}[L \circ G(t)] = \hat{L}\,\hat{G}(\omega) = \mathscr{F}[\delta(t)] = 1 \tag{B.10a}$$

$$\Rightarrow G(t) = \mathscr{F}^{-1}\left[\hat{L}^{-1}\right] \tag{B.10b}$$

To summarize, a linear and ordinary differential equation with time dependent inhomogeneity can be solved by applied Green's function approach in the following way.

1. Find the general solution $f_h(t)$ of the homogeneous ode system $L \circ f(t) = 0$.
2. Find the Green's function $G(t)$ of the differential operator L with Eq. (B.10).
3. Calculate the fundamental solution $\tilde{f}(t)$ of the inhomogeneous ode system with Eq. (B.8b).
4. Generate the general solution of the inhomogeneous ode system with Eq. (B.9).

[3] The following convention is used: $\mathscr{F}[f(t)] = \int_{-\infty}^{\infty} f(t)\,\mathrm{e}^{i\,\omega\,t}\,\mathrm{d}t$ and $\mathscr{F}^{-1}[\hat{f}(\omega)] = \frac{1}{2\,\pi}\int_{-\infty}^{\infty} \hat{f}(\omega)\,\mathrm{e}^{i\,\omega\,t}\,\mathrm{d}\omega$.

This procedure shall now be applied to Eq. (5.4c). The differential equation to be solved is given by:

$$\dot{d} = \gamma\,(\Delta x - d) \quad \Leftrightarrow \quad \left[\frac{\mathrm{d}}{\mathrm{d}t} + \gamma\right] \circ d(t) = \gamma\,\Delta x(t) \tag{B.11}$$

The linear differential operator is given by $L = \left[\frac{\mathrm{d}}{\mathrm{d}t} + \gamma\right]$ and the time dependent inhomogeneity is given by $\phi(t) = \gamma\,\Delta x(t)$. The general solution $d_h(t)$ of the homogeneous system is known.

$$\frac{\mathrm{d}d}{\mathrm{d}t} = -\gamma\,d \quad \Rightarrow \quad d_h(t) = d_0\,\mathrm{e}^{-\gamma\,t} \tag{B.12}$$

Here $d(t=0) = d_0$ is the initial condition which decays to zero over a time scale given by γ^{-1}. The Green's function of the differential operator under study can be found in the following way:

$$\mathscr{F}\left[\left[\frac{\mathrm{d}}{\mathrm{d}t} + \gamma\right] \circ G(t)\right] = (i\omega + \gamma)\,\hat{G}(\omega) = 1 \tag{B.13a}$$

$$\Rightarrow G(t) = \mathscr{F}^{-1}\left[\frac{1}{i\omega + \gamma}\right] = \frac{1}{2\,\pi}\int_{-\infty}^{\infty} \frac{\mathrm{e}^{i\,\omega\,t}}{i\omega + \gamma}\,\mathrm{d}\omega. \tag{B.13b}$$

To calculate the Green's function, the integral given by Eq. (B.13b) has to be solved. This is done by splitting up the exponential function into sine and cosine, by multiplying the integrand with the complex conjugated of $i\omega + \gamma$, and by splitting up the integral into its real an imaginary components.

$$G(t) = \frac{1}{2\,\pi}\int_{-\infty}^{\infty} \frac{[\cos(\omega\,t) + i\,\sin(\omega\,t)]\,[\gamma - i\,\omega]}{\gamma^2 + \omega^2}\,\mathrm{d}\omega \tag{B.14a}$$

$$\mathrm{Re}\{G(t)\} = \frac{\gamma}{2\,\pi}\int_{-\infty}^{\infty} \overbrace{\frac{\cos(\omega\,t)}{\gamma^2 + \omega^2}}^{\text{symmetric}}\,\mathrm{d}\omega + \frac{1}{2\,\pi}\int_{-\infty}^{\infty} \overbrace{\frac{\omega\,\sin(\omega\,t)}{\gamma^2 + \omega^2}}^{\text{symmetric}}\,\mathrm{d}\omega \tag{B.14b}$$

$$\mathrm{Im}\{G(t)\} = \frac{\gamma}{2\,\pi}\int_{-\infty}^{\infty} \overbrace{\frac{\sin(\omega\,t)}{\gamma^2 + \omega^2}}^{\text{antisymmetric}}\,\mathrm{d}\omega - \frac{1}{2\,\pi}\int_{-\infty}^{\infty} \overbrace{\frac{\omega\,\cos(\omega\,t)}{\gamma^2 + \omega^2}}^{\text{antisymmetric}}\,\mathrm{d}\omega \tag{B.14c}$$

The imaginary part of $G(t)$ vanishes since it comprises only integrals with asymmetric integrands. The real part of $G(t)$ comprises integrals which can be rewritten and found in literature[4].

$$G(t) = \mathrm{Re}\{G(t)\} = \frac{1}{\pi}\int_{0}^{\infty} \frac{\gamma\,\cos(\omega\,t)}{\gamma^2 + \omega^2} + \frac{\omega\,\sin(\omega\,t)}{\gamma^2 + \omega^2}\,\mathrm{d}\omega = \mathrm{e}^{-|\gamma\,t|} \tag{B.15a}$$

$$\Rightarrow G(t) = \mathrm{e}^{-\gamma\,t} \quad \text{with} \quad \gamma, t \geq 0 \tag{B.15b}$$

With the calculated Green's function, a fundamental solution $\tilde{d}(t)$ of the inhomogeneous system Eq. (B.11) can be constructed.

$$\tilde{d}(t) = \gamma\,\Delta x(t) * G(t) = \gamma\int_{0}^{t} \mathrm{e}^{-\gamma\,(t-\tau)}\,\Delta x(\tau)\,\mathrm{d}\tau \quad \text{with} \quad \Delta x(t) \equiv 0 \text{ for } t < 0 \tag{B.16}$$

[4] Bronstein [79] page 1083.

Combining the general solution Eq. (B.12) of the homogeneous system and the fundamental solution Eq. (B.16) of the inhomogeneous system yields the general solution of the inhomogeneous system Eq. (B.11).

$$d(t) = d_h(t) + \tilde{d}(t) = d_h(t) = d_0 \, \mathrm{e}^{-\gamma \, t} + \gamma \int_0^t \mathrm{e}^{-\gamma \, (t-\tau)} \, \Delta x(\tau) \, \mathrm{d}\tau \tag{B.17}$$

This solution is discussed in the following of Eq. (5.12).

Bibliography

[1] K. Golenhofen. *Physiologie heute*. München, Germany: Urban & Fischer, 2000. 576 pp.

[2] D. M. Bers. "Cardiac excitation-contraction coupling". *Nature* 415.6868 (2002), 198–205.

[3] D. M. Bers. "Calcium Cycling and Signaling in Cardiac Myocytes". *Annual Review of Physiology*. Vol. 70. Palo Alto: Annual Reviews, 2008, 23–49.

[4] S. Viatchenko-Karpinski et al. "Intracellular Ca2+ oscillations drive spontaneous contractions in cardiomyocytes during early development". *Proceedings of the National Academy of Sciences of the United States of America* 96.14 (1999), 8259–8264.

[5] J. Satin et al. "Mechanism of spontaneous excitability in human embryonic stem cell derived cardiomyocytes". *Journal of Physiology-London* 559.2 (2004), 479–496.

[6] P. Sasse et al. "Intracellular Ca2+ oscillations, a potential pacemaking mechanism in early embryonic heart cells". *Journal of General Physiology* 130.2 (2007), 133–144.

[7] J. Domke et al. "Mapping the mechanical pulse of single cardiomyocytes with the atomic force microscope". *European Biophysics Journal with Biophysics Letters* 28.3 (1999), 179–186.

[8] J. F. S. Cogollo et al. "A new integrated system combining atomic force microscopy and micro-electrode array for measuring the mechanical properties of living cardiac myocytes". *Biomedical Microdevices* 13.4 (2011), 613–621.

[9] J. Liu et al. "Atomic Force Mechanobiology of Pluripotent Stem Cell-Derived Cardiomyocytes". *PLoS ONE* 7.5 (2012), e37559.

[10] W.-T. Chang et al. "Characterization of the Mechanodynamic Response of Cardiomyocytes with Atomic Force Microscopy". *Analytical Chemistry* 85.3 (2013), 1395–1400.

[11] T. Eschenhagen et al. "Three-dimensional reconstitution of embryonic cardiomyocytes in a collagen matrix: a new heart muscle model system". *Faseb Journal* 11.8 (1997), 683–694.

[12] M. Tiburcy et al. "Defined Engineered Human Myocardium With Advanced Maturation for Applications in Heart Failure Modeling and Repair". *Circulation* 135.19 (2017), 1832–1847.

[13] I. Nitsan et al. "Mechanical communication in cardiac cell synchronized beating". *Nature Physics* 12.5 (2016), 472–477.

[14] A. Harris, D. Stopak, and P. Wild. "Fibroblast Traction as a Mechanism for Collagen Morphogenesis". *Nature* 290.5803 (1981), 249–251.

[15] V. H. Barocas and R. T. Tranquillo. "An anisotropic biphasic theory of tissue-equivalent mechanics: The interplay among cell traction, fibrillar network deformation, fibril alignment, and cell contact guidance". *Journal of Biomechanical Engineering-Transactions of the Asme* 119.2 (1997), 137–145.

[16] K. D. Costa, E. J. Lee, and J. W. Holmes. "Creating alignment and anisotropy in engineered heart tissue: Role of boundary conditions in a model three-dimensional culture system". *Tissue Engineering* 9.4 (2003), 567–577.

[17] N. W. Tschoegl. *The Phenomenological Theory of Linear Viscoelastic Behavior*. Berlin, Heidelberg: Springer Berlin Heidelberg, 1989. 769 pp.

[18] D. M. Knapp et al. "Rheology of reconstituted type I collagen gel in confined compression". *Journal of Rheology* 41.5 (1997), 971–993.

[19] V. K. Lai et al. "Microstructural and mechanical differences between digested collagen-fibrin co-gels and pure collagen and fibrin gels". *Acta Biomaterialia* 8.11 (2012), 4031–4042.

[20] H. Li and Y. Zhang. "Modeling of the viscoelastic behavior of collagen gel from dynamic oscillatory shear measurements". *Biorheology* 51.6 (2014), 369–380.

[21] A. Moon and R. Tranquillo. "Fibroblast-Populated Collagen Microsphere Assay of Cell Traction Force .1. Continuum Model". *Aiche Journal* 39.1 (1993), 163–177.

[22] V. Barocas, A. Moon, and R. Tranquillo. "The Fibroblast-Populated Collagen Microsphere Assay of Cell Traction Force .2. Measurement of the Cell Traction Parameter". *Journal of Biomechanical Engineering-Transactions of the Asme* 117.2 (1995), 161–170.

[23] V. K. Lai et al. "A Multiscale Approach to Modeling the Passive Mechanical Contribution of Cells in Tissues". *Journal of Biomechanical Engineering-Transactions of the Asme* 135.7 (2013), 071007.

[24] R. H. Ewoldt, A. E. Hosoi, and G. H. McKinley. "New measures for characterizing nonlinear viscoelasticity in large amplitude oscillatory shear". *Journal of Rheology* 52.6 (2008), 1427–1458.

[25] S. W. Katicha and G. W. Flintsch. "Fractional viscoelastic models: master curve construction, interconversion, and numerical approximation". *Rheologica Acta* 51.8 (2012), 675–689.

[26] A. Jaishankar and G. H. McKinley. "Power-law rheology in the bulk and at the interface: quasi-properties and fractional constitutive equations". *Proceedings of the Royal Society a-Mathematical Physical and Engineering Sciences* 469.2149 (2013), 20120284.

[27] M. B. Cannell et al. "Control of Sarcoplasmic Reticulum Ca2+ Release by Stochastic RyR Gating within a 3D Model of the Cardiac Dyad and Importance of Induction Decay for CICR Termination". *Biophysical Journal* 104.10 (2013), 2149–2159.

[28] M. M. Maleckar et al. "Studying dyadic structure–function relationships: a review of current modeling approaches and new insights into Ca2+ (mis) handling". *Clinical Medicine Insights-Cardiology* 11 (2017).

[29] R. R. Aliev and A. V. Panfilov. "A simple two-variable model of cardiac excitation". *Chaos Solitons & Fractals* 7.3 (1996), 293–301.

[30] L. D. Weise and A. V. Panfilov. "Emergence of Spiral Wave Activity in a Mechanically Heterogeneous Reaction-Diffusion-Mechanics System". *Physical Review Letters* 108.22 (2012), 228104.

[31] Y. Yamauchi, A. Harada, and K. Kawahara. "Changes in the fluctuation of interbeat intervals in spontaneously beating cultured cardiac myocytes: experimental and modeling studies". *Biological Cybernetics* 86.2 (2002), 147–154.

[32] O. Cohen and S. A. Safran. "Elastic interactions synchronize beating in cardiomyocytes". *Soft Matter* 12.28 (2016), 6088–6095.

[33] L. M. Pecora and T. L. Carroll. "Master stability functions for synchronized coupled systems". *Physical Review Letters* 80.10 (1998), 2109–2112.

[34] S. H. Strogatz. "From Kuramoto to Crawford: exploring the onset of synchronization in populations of coupled oscillators". *Physica D* 143.1 (2000), 1–20.

[35] S. Astakhov et al. "The role of asymmetrical and repulsive coupling in the dynamics of two coupled van der Pol oscillators". *Chaos: An Interdisciplinary Journal of Nonlinear Science* 26.2 (2016), 023102.

[36] T. Bountis. "From mechanical to biological oscillator networks: The role of long range interactions". *European Physical Journal-Special Topics* 225.6 (2016), 1017–1035.

[37] Y. N. Kyrychko, K. B. Blyuss, and E. Schoell. "Amplitude and phase dynamics in oscillators with distributed-delay coupling". *Philosophical Transactions of the Royal Society a-Mathematical Physical and Engineering Sciences* 371.1999 (2013), 20120466.

[38] Y. N. Kyrychko, K. B. Blyuss, and E. Schoell. "Synchronization of networks of oscillators with distributed delay coupling". *Chaos* 24.4 (2014), 043117.

[39] D. M. Abrams and S. H. Strogatz. "Chimera states for coupled oscillators". *Physical review letters* 93.17 (2004), 174102.

[40] T. Banerjee. "Chimera death induced by the mean-field diffusive coupling". *arXiv:1409.7895 [nlin]* (2014). arXiv: 1409.7895.

[41] K. M. Stiefel and G. B. Ermentrout. "Neurons as oscillators". *Journal of Neurophysiology* 116.6 (2016), 2950–2960.

[42] J. Pena-Ramirez, R. H. Fey, and H. Nijmeijer. "IN-PHASE AND ANTI-PHASE SYNCHRONIZATION OF OSCILLATORS WITH HUYGENS' COUPLING". *CYBERNETICS AND PHYSICS* 1 (2012), 58–66.

[43] J. Pena Ramirez et al. "The sympathy of two pendulum clocks: beyond Huygens' observations". *Scientific Reports* 6 (2016).

[44] A. R. Bausch, W. Moller, and E. Sackmann. "Measurement of local viscoelasticity and forces in living cells by magnetic tweezers". *Biophysical Journal* 76.1 (1999), 573–579.

[45] J. Argyris, G. Faust, and M. Haase. *Die Erforschung des Chaos*. Wiesbaden: Vieweg+Teubner Verlag, 1994.

[46] U. Parlitz. "Estimating Lyapunov Exponents from Time Series". C. Skokos, G. A. Gottwald, and J. Laskar. *Chaos Detection and Predictability*. Vol. 915. Lecture Notes in Physics. Berlin: Springer-Verlag Berlin, 2016, 1–34.

[47] Wikimedia Commons. *File:Bifurcation DiagramB.png - Wikimedia Commons*. 2016. URL: `https://commons.wikimedia.org/wiki/File:Bifurcation_DiagramB.png` (visited on 07/11/2017).

[48] A. Pikovsky, M. Rosenblum, and J. Kurths. *Synchronization: a universal concept in nonlinear sciences*. Cambridge Nonlinear Science 12. New York: Cambridge University Press, 2003.

[49] G. Beeler and H. Reuter. "Relation Between Membrane Potential, Membrane Currents and Activation of Contraction in Ventricular Myocardial Fibres". *Journal of Physiology-London* 207.1 (1970), 211–229.

[50] *Device-Independent Bitmaps (Windows)*. URL: `https://msdn.microsoft.com/en-us/library/windows/desktop/dd183562(v=vs.85).aspx#` (visited on 04/20/2017).

[51] *AVI RIFF File Reference (Windows)*. URL: `https://msdn.microsoft.com/en-us/library/windows/desktop/dd318189(v=vs.85).aspx` (visited on 04/20/2017).

[52] Aldus Developers Desk. *TIFF Revision 6.0*. 1986.

[53] *FFmpeg - A complete, cross-platform solution to record, convert and stream audio and video*. FFmpeg. URL: `https://www.ffmpeg.org/` (visited on 05/08/2017).

[54] J. Schindelin et al. "Fiji: an open-source platform for biological-image analysis". *Nature Methods* 9.7 (2012), 676–682.

[55] J. Schindelin et al. "The ImageJ ecosystem: An open platform for biomedical image analysis". *Molecular Reproduction and Development* 82.7 (2015), 518–529.

[56] C. Xu and J. L. Prince. *Active Contours, Deformable Models, and Gradient Vector Flow*. Active Contours, Deformable Models, and Gradient Vector Flow. URL: `http://www.iacl.ece.jhu.edu/static/gvf/` (visited on 05/29/2017).

[57] C. Xu and J. L. Prince. "Gradient vector flow: A new external force for snakes". *1997 Ieee Computer Society Conference on Computer Vision and Pattern Recognition, Proceedings*. Los Alamitos: I E E E, Computer Soc Press, 1997, 66–71.

[58] T. Kaneko, F. Nomura, and K. Yasuda. "On-chip constructive cell-Network study (I): Contribution of cardiac fibroblasts to cardiomyocyte beating synchronization and community effect". *Journal of Nanobiotechnology* 9.1 (2011), 21.

[59] A. P. G. Castro et al. "Combined numerical and experimental biomechanical characterization of soft collagen hydrogel substrate". *Journal of Materials Science-Materials in Medicine* 27.4 (2016), 79.

[60] S. Stein, S. Luther, and U. Parlitz. "Impact of viscoelastic coupling on the synchronization of symmetric and asymmetric self-sustained oscillators". *New Journal of Physics* 19.6 (2017), 063040.

[61] P. C. Matthews, R. E. Mirollo, and S. H. Strogatz. "Dynamics of a large system of coupled nonlinear oscillators". *Physica D: Nonlinear Phenomena* 52.2 (1991), 293–331.

[62] P. Ashwin, J. Buescu, and I. Stewart. "Bubbling of Attractors and Synchronization of Chaotic Oscillators". *Physics Letters A* 193.2 (1994), 126–139.

[63] F. M. Atay. "Distributed delays facilitate amplitude death of coupled oscillators". *Physical Review Letters* 91.9 (2003), 094101.

[64] J. Teramae and D. Tanaka. "Robustness of the noise-induced phase synchronization in a general class of limit cycle oscillators". *Physical Review Letters* 93.20 (2004), 204103.

[65] V. V. Klinshov and V. I. Nekorkin. "Synchronization of delay-coupled oscillator networks". *Physics-Uspekhi* 56.12 (2013), 1217–1229.

[66] D. Dudkowski et al. "Hidden attractors in dynamical systems". *Physics Reports-Review Section of Physics Letters* 637 (2016), 1–50.

[67] H. Nakao. "Phase reduction approach to synchronisation of nonlinear oscillators". *Contemporary Physics* 57.2 (2016), 188–214.

[68] J. A. Acebron et al. "The Kuramoto model: A simple paradigm for synchronization phenomena". *Reviews of Modern Physics* 77.1 (2005), 137–185.

[69] Y. N. Kyrychko, K. B. Blyuss, and E. Schoell. "Amplitude death in systems of coupled oscillators with distributed-delay coupling". *European Physical Journal B* 84.2 (2011), 307–315.

[70] C. Wille, J. Lehnert, and E. Schoell. "Synchronization-desynchronization transitions in complex networks: An interplay of distributed time delay and inhibitory nodes". *Physical Review E* 90.3 (2014), 032908.

[71] R. Dilao. "Antiphase and in-phase synchronization of nonlinear oscillators: The Huygens's clocks system". *Chaos: An Interdisciplinary Journal of Nonlinear Science* 19.2 (2009), 023118.

[72] V. Gattulli, F. Potenza, and M. Lepidi. "Damping performance of two simple oscillators coupled by a visco-elastic connection". *Journal of Sound and Vibration* 332.26 (2013), 6934–6948.

[73] B. van der Pol. "On "relaxation oscillations."". *Philosophical Magazine* 2.11 (1926), 978–992.

[74] J. C. Maxwell. "On the Dynamical Theory of Gases". *Philosophical Transactions of the Royal Society of London* 157 (1867), 49–88.

[75] M. Tsatsos. "Theoretical and Numerical study of the Van der Pol equation". *Doctoral desertation, Aristotle University of Thessaloniki* (2006).

[76] *AUTO - SOFTWARE FOR CONTINUATION AND BIFURCATION PROBLEMS IN ORDINARY DIFFERENTIAL EQUATIONS*. URL: `http://indy.cs.concordia.ca/auto/` (visited on 04/20/2016).

[77] E. J. Doedel and B. E. Oldeman. *AUTO-07P : CONTINUATION AND BIFURCATION SOFTWARE FOR ORDINARY DIFFERENTIAL EQUATIONS*. 2012.

[78] T. S. Girton, V. H. Barocas, and R. T. Tranquillo. "Confined compression of a tissue-equivalent: Collagen fibril and cell alignment in response to anisotropic strain". *Journal of Biomechanical Engineering-Transactions of the Asme* 124.5 (2002), 568–575.

[79] I. N. Bronstein et al. *Taschenbuch der Mathematik*. Frankfurt am Main: Harri Deutsch GmbH, 2008. 1221 pp.

List of Figures

2.1. Excitation contraction coupling. 6
2.2. Engineered heart muscle. 8
2.3. Object deformed by an external stress. 9
2.4. Hookean spring and Newtonian dashpot. 10
2.5. Maxwell fluid and Kelvin-Voigt material. 10
2.6. Complex moduli of Maxwell fluid and Kelvin-Voigt material. 12
2.7. Phase space portrait of the Van der Pol oscillator. 16
2.8. Phase volume and Lyapunov exponents. 19
2.9. Phase space portrait of a saddle-node bifurcation. 21
2.10. Bifurcation diagram of a saddle-node bifurcation. 22
2.11. Bifurcation of the Rössler system 23
2.12. Dynamics of a self-sustained oscillator. 27
2.13. Neutral stability of the phase. 29
2.14. Synchronisation of two oscillators. 31

3.1. Snapshots of example cell videos. 34
3.2. Components found in the cell videos. 35
3.3. Preprocessing of cell videos. 36
3.4. Signal of the mean intensity approach. 37
3.5. Reference frame approach. 38
3.6. Signal of the reference image approach. 39
3.7. Active contour approach. 41
3.8. Signal of the active contour approach. 43
3.9. Outlier filter. 45
3.10. Band pass filter. 47
3.11. Svd filter. 48
3.12. Fourier series filter. 50
3.13. Signal of cell 1. 52
3.14. Beating signal of cell 1 with extrema. 54
3.15. Spectrum of cell 1. 55
3.16. Orbits representing cellular beating. 56

4.1. Rheometer sketch. 60
4.2. Complex modulus of the collagen gel over time. 61
4.3. LAOS – stress response. 63
4.4. LAOS – Lissajous figures. 64
4.5. Sketch of the Maxwell fluid. 66

4.6. Fit of the Maxwell fluid to LAOS-data. 67
4.7. Temporal evolution of the Maxwell fluid parameters. 68

5.1. Dynamics of the Van der Pol oscillator. 71
5.2. Dynamics of the modified van der Pol oscillator. 73
5.3. Asymmetric Van der Pol oscillator vs. cardiomyocyte beating. 74
5.4. Sketch of coupled oscillators. 76
5.5. Pendulum and cardiomyocyte picture. 77
5.6. Comparison of in- and anti-phase synchronisation states. 81
5.7. Frequency ration between in- and anti-phase synchronisation states. . 82
5.8. Bifurcation diagram of in-phase state. 84
5.9. Viscoelastic phase diagram. 85
5.10. Viscoelastic phase diagram - cardiomyocyte picture. 86
5.11. Frequency map of the in- and anti-phase states. 88
5.12. Line scan of the frequency map. 89
5.13. Bifurcation diagram featuring the asymmetry parameter c. 91
5.14. Chaos in the asymmetric system. 92
5.15. Oscillations of new in-phase state. 93
5.16. Lyapunov exponent map of the asymmetric Van der Pol oscillator. . . 93
5.17. Bifurcation diagram of Duffing oscillator. 95
5.18. Lyapunov exponent map of the Duffing oscillator. 96

A.1. The six cells. 103
A.2. Comparison of a good and a poor cel signal. 104
A.3. Beating signal of cell 1. 105
A.4. Beating signal of cell 2. 105
A.5. Beating signal of cell 3. 106
A.6. Beating signal of cell 4. 106
A.7. Beating signal of cell 5. 107
A.8. Beating signal of cell 6. 107
A.9. Spectrum of cell 1. 108
A.10. Spectrum of cell 2. 108
A.11. Spectrum of cell 3. 109
A.12. Spectrum of cell 4. 109
A.13. Spectrum of cell 5. 110
A.14. Spectrum of cell 6. 110
A.15. Frequency map of the in-phase synchronisation states - colour scale. . 111
A.16. Oscillation form of in- and anti-phase state. 112
A.17. LAOS – Lissajous figures raw data. 113

Acknowledgements

At his point, I like to thank several people and organisations who supported me during my studies and who made this thesis possible.

First, I like to thank Prof. Stefan Luther who not only gave me the opportunity to do my masters degree in his group, the *Biomedical Physics Group at the Max Planck Institute for Dynamics and Self-Organization, Göttingen*, but to pursue my PhD-studies there as well.

During that time, I received founding from the German Research Foundation (DFG) (Collaborative Research Center SFB 937 Project A18) and I appreciate this support. Because of the SFB 937, I had the opportunity to collaborate with several colleagues from the *Institute of Pharmacology and Toxicology, University Medical Center Göttingen* and from the *Third Institute of Physics - Biophysics, Georg-August-University Göttingen*. In this context, I foremost worked together with Susanne Schlick, who supported my theoretical and numerical work with experimental video data from premature cardiomyocytes, and Florian Rehfeldt, who provided the instruments and supervised the rheological experiments I conducted together with Susanne Schlick and Florian Spreckelsen, respectively. I am very happy that I could rely on their support.

Furthermore, I would like to thank Prof. Reiner Kree, whom I know since my very first physics lecture: Physik I in the winter semester 2008. He supervised my bachelor thesis at the *Institut of Theoretische Physics, Georg-August-University Göttingen* and his contributions in my annual thesis committee meetings have always been helpful.

All the people which accompanied me as colleagues in the *Biomedical Physics Group* deserve many thanks as well. Jan Christoph did a great job while supervising me while I worked on my master thesis. Daniel Hornung and Sebastian Berg helped me with all kinds of technical problems. I really enjoined the scientific and non-scientific discussions and free time activities with Florian Spreckelsen, Svetlana Husser (my in-group-SFB-937 collaborators), Edda Boccia, Henrik tom Wörden, Jan Schumann-Bischoff, Johannes Schröder-Schetelig (who were my office mates for several years), and of course Alexander Schlemmer (who accompanied me even across offices). With Alex, I discussed statistics, math, physics, science, programming languages, bureaucracy, psychology, philosophy, rhetoric, video games and other many things; he introduced me to the bliss of Arch Linux; together, we wagged our torches and pitchforks when office space was rare; and although we never had the opportunity to bend a "banana state" under our will, we confronted the elder gods several times in grave danger. Thank you very much, Alex. Thank you all very much and although I could only name a few of you, my thanks belongs to every group member. I did not only achieve my PhD degree during the past years, I made friends.

In the second half of my first semester at the Georg-August-University Göttingen, I met Simon Christoph Stein and we discovered that our grandfathers were brothers. He introduced me to a nice group of students, among them Simon Sebastian Schütz. Christoph, Simon and I share not only our names but five to nine years of physics studies. Together we solved exercise sheets, passed exams, earned our degrees and spent our free time together. Especially during the first three semesters, which were difficult times for me, I could always rely on them to have my back. I am not sure if I would have had the opportunity to write these lines if I had not met them. Thank you very much.

There is another fellow student and friend of mine who accompanies me now for several years and needs to be mentioned: Jan Thiart. Christoph, Jan and I sped uncountable hours together. But first and foremost we beat several video games, had many movie nights and explored with passion the ever changing culinary scene in Göttingen. Whenever the mana seems to be drained from the world or whenever a man in a bear costume hits a woman, I will think about you. I cannot imagine how the past decade would have been without you three. So thank you very much.

So far, I mentioned only those people who I met and who joined me during my time at the university. But there are of course others who supported me "behind the scenes".

Whenever I needed a break from Göttingen, I was able to visit my close childhood friends: Timo Liebig whom I know since my very first year as a pupil, Gerrit Schnaase who taught me about life itself ever since I met him, and Michael Wiegelmann who always offers me a bed and a roof whenever I visit my old home town. There are myriads of anecdotes to tell and I know that there are myriads of anecdotes to come. But at this point my gratefulness for knowing them cumulates in a simple *thank you very much*.

Another person who deserves many thanks is my dear *favourite* aunt Renate Lemmermyer. She supported me without any question throughout my entire life and in every dark or bright circumstances. Together with her husband Walter Lemmermeyer she provides a second home for me, which I never want to miss.

A special thanks goes to my grandpa Wilhelm Wendel, my grandma Olga Wendel, and my parents, Hartmut Stein and Sabine Stein, who supported me as long as they could. I literally would not writing these lines if they had not been there. Before I went to school, Wilhelm had already taught me simple maths like addition and multiplication and together, they provided the environment for a very happy and fruitful childhood.

Furthermore, I would like to thank my beautiful and intelligent girlfriend Carmina Warth who supported me with the most delicious food and a lot of patience during the final writing-my-thesis-down episode, when I locked myself away from the world.

At the beginning of this chapter, I said that I like to thank those people who made this thesis possible. Although I mentioned many of them, there are two who very directly influenced me as a physicist. This is the last, but the very opposite of least part of the acknowledgement chapter and I would like to start it with a quote.

"A teacher affects eternity: he can never tell where his influence stops."
— Henry Brooks Adams

In this context, I like to thank my direct supervisor, my *Doktorvater*, Prof. Ulrich Parlitz. I learned a lot from him. He taught me about physics, he thought me to be a scientist, and he taught me about the little details of wise communication. Whenever I had the need to speak to him about the large or little problems which occur in the life of a student, he always was only one office, one call, or one e-mail away and without delay, he always spent his time to help me. With patience, commitment, and guidance he created the fruitful environment which a student needs to develop. Even beside his roll as a supervisor, it was always pleasant to have the person, Ulrich Parltz, with his positive attitude around and I very enjoyed to be his student. I know that all this is by far not a matter of course and I am very grateful for that. Thank you very much, Ulrich. It turned out to be like you always said: *"Alles wird gut."*.

The second person I would like to thank in this context is my very first physics teacher Bernd Rauschenbach to whom this thesis is dedicated. Although I have not had contact to him for many years now, I recall him as a friendly and knowledgeable person, with a sound sense of humour, who enjoyed being a teacher and who earned the respect of his pupils by always being fair. He taught me for several years, wether it was physics or maths, and after some time, he addressed me with the nickname *Basti Fantasti*. I especially remember one class in which we studied hydraulic pressure. I was finished with writing down from the blackboard and I told my table neighbour Timo that now that I have everything in my notebook, it needs to go into my head. I started to make a sketch of the equations we just learned, when I noticed Mr. Rauschenbach standing behind me. He smiled at me and went along. With his attitude and his commitment he was the one who planted the seed which should become my delight in becoming and being a physicist. Until today, he is one of my favourite teachers and physics is still my favourite subject. Thank you very much, Mr. Rauschenbach.

With this, I want to close and conclusively thank all my *"teachers"*, wether they had taught me in school, at the university or about the subjects of life outside those halls and wether I have named them here or not. I cannot tell where their influence will stop, but so far, it led to this thesis and a doctoral degree in physics. Thank you very much!

Curriculum Vitae

Sebastian Stein

Data of birth: 15.11.1988
Place of birth: Bad Arolsen
Nationality: German

Academical Background

04.2014 - 09.2017	**Doctor Rerum Naturalium** in Physics Thesis: *Synchronisation Behaviour of Viscoelastically Coupled Self-Sustained Oscillators as Models for Premature Cardiomyocytes* Georg-August-Universität Göttingen, MPI for Dynamics Self-Organisation, Göttingen
10.2011 - 10.2013	**Master of Science** in Physics Thesis: *Three Dimensional Electromechanical Computer Model of the Heart Based on a Discrete Particle Simulation* Georg-August-Universität Göttingen, MPI for Dynamics and Self-Organisation, Göttingen
10.2008 - 07.2011	**Bachelor of Science** in Physics Thesis: *Stability of smooth surfaces under ion bombardment: Non-local effects and the influence of surface barriers* Georg-August-Universität Göttingen
2005 - 2008	**Abitur** Berufliches Gymnasium, Korbach

Publications

2017	**Sebastian Stein**, Stefan Luther, and Ulrich Parlitz. Impact of viscoelastic coupling on the synchronization of symmetric and asymmetric self-sustained oscillators. *New Journal of Physics*, 19(6):063040, 2017. doi: 10.1088/1367-2630/aa6d4a.

Conference Contributions

Posters

2015	XXXV Dynamics Days, Exeter, UK (*poster award*)
2015	SFB 937 Autumn School, Hohegeis, GER
2016	International Symposium (SFB 755, SFB 803, SFB 937), Grimma, GER

Talks

2015	SFB 937 Autumn School, Hohegeis, GER
2016	International Symposium (SFB 755, SFB 803, SFB 937), Grimma, GER
2016	Perspectives in Nonlinear Dynamics (PNLD), Berlin, GER
2016	SFB 937 Summer School, Heiligenstadt, GER
2017	DPG-Frühjahrstagung, Dresden, GER